M. Smoluchowski Institute of Physics
Jagiellonian University

EFFECTS OF QUANTUM CHROMODYNAMICS IN THE HIGH ENERGY LIMIT IN PARTICLE COLLISIONS

Sebastian Sapeta

Thesis presented for the degree of Doctor of Philosophy
written under the supervision of
dr hab. Krzysztof Golec-Biernat

Kraków
2008

Contents

Preface

Quantum Chromodynamics (QCD) is the most successful fundamental theory of strong interactions. Since the time of its beginnings, over three decades ago, it has been extensively developed and tested in numerous experiments. Nevertheless, at the present state of the art, the theory is far from being completely solved or even fully explored. On the contrary, there are many effects predicted by QCD which still lack firm experimental evidence. Similarly, numerous experimental facts, sometimes very basic, wait for comprehensive theoretical description.

The deep inelastic electron–proton scattering (DIS) is one of the most important QCD processes. The standard theoretical approach to DIS is based on the collinear factorization between the long and short distance parts of the theory. The latter can be described within perturbative approach since the hard scale is provided by the high virtuality of the photon γ^* and, as a result, the strong coupling α_s is small. However, α_s is always accompanied by the large logarithm of virtuality so that $\alpha_s \ln Q^2 \sim 1$. Therefore, the key element of the proper description of DIS in this approach is the necessity to resum an infinite class of terms of the type $(\alpha_s \ln Q^2)^n$.

In the high energy limit, in which the center-of-mass energy of the $\gamma^* p$ system $W^2 \gg Q^2$, the above description of DIS becomes questionable. This limit corresponds to small values of the Bjorken variable $x \simeq Q^2/W^2$ and now the large logarithms $\ln(1/x)$ should be taken into account leading to the infinite resummation of terms $(\alpha_s \ln(1/x))^n$. This is referred to as the $k_\perp$ factorization or the high energy factorization approach. In the limit of small x, the proton appears as a dense system of soft gluons. The strong rise of the gluon number with decreasing x was one of the most important findings of HERA experiments. In contrast to the regime of DIS in which Q^2 is the only large scale, here, the interactions between gluons can give sizable effect. In particular, the growth of gluon density is expected to slow down due to the recombination processes, which are non-negligible in a dense system. This goes under the name of gluon saturation and is necessary to ensure unitarity of the $\gamma^* p$ cross section. The first part of this Thesis is devoted to the issue of proton structure in the transition region between the "dilute" and "saturated" regime.

The state of the saturated QCD matter is described by theory of the color glass condensate (CGC). This state can be created in DIS at low x or in the high energy collisions of heavy nuclei. In the latter case, the CGC phase turns after the collision into the new state of matter called the quark gluon plasma (QGP). The experimental data from the gold–gold collisions suggests that the latter state has been attained at RHIC. The evidence is provided *e.g.* by the observed suppression of leading particles.

The properties of QGP can be studied by analyzing modifications of jets created in the collisions of heavy ions. The attenuation of yields of high momenta particles measured at RHIC supports this idea. The theoretical framework used to describe jets is similar to that developed for the case of DIS. In particular, one also performs the infinite resummation of terms containing large logarithms generated by soft and collinear gluons. However, the satisfactory theoretical description of the interactions of jets with the dense QCD matter is still not available. Instead, one uses realistic models of jet modifications. This allows to study the properties of QGP and on the other hand, confronted with the data, may guide the theoretical investigations. The study of jets modified by the dense medium is the subject of the second part of this Thesis.

The outline of the dissertation is the following.

Chapter 1 serves as an introduction in which we review basic facts concerning QCD and establish notation. There, we present the standard approach to DIS in the framework of the collinear factorization and introduce the concept of parton distribution function. We also discuss the linear evolution equation, called DGLAP equation.

In Chapter 2, we focus on the DIS in the limit of low x (or equivalently high energy of the $\gamma^* p$ collision). We discuss the framework of $k_\perp$ factorization and the BFKL evolution equation, which allows to calculate the unintegrated gluon distributions in the regime of dilute system. There, we also establish the relation between the collinear and $k_\perp$ factorization. Finally, in Chapter 2, we point out the deficiencies of the BFKL equation in the regime of dense gluonic systems and the necessity to account for the saturation effects in this limit.

In Chapter 3, we present the study of the heavy flavor production in deep inelastic scattering in the framework of a saturation model based on QCD. The model was proposed by Golec-Biernat and Wüsthoff and further improved by Bartels, Golec-Biernat and Kowalski. We demonstrate that this model is not only able to precisely fit the HERA data but also to correctly predict the charm and beauty quark contributions to the proton structure function as well as some other quantities.

In Chapter 4, we introduce the basic QCD equation, which captures the essential features of saturation, namely the BK equation. We show that solutions of this equation are in qualitative agreement with the assumptions of the saturation model from Chapter 3. We also describe a specific method of analyzing the BK equation proposed by Munier and Peschanski, called the traveling waves approach. This method allows to obtain solutions of the BK equation in the limit of asymptotically small x.

In Chapter 5, we study, in the framework of the traveling waves approach, the asymptotic solutions of the most developed form of the BK equation, namely with the running coupling and the NLL BFKL kernel. We obtain solutions for the scattering amplitude as well the saturation scale. We also explore the possibility of adopting our asymptotic result to the phenomenological energies.

In Chapter 6, we discuss the essential facts concerning jets and their characteristics. We introduce the notion of the fragmentation function, which is an object complementary to the parton distribution function used in the description of DIS. There, we also discuss the the perturbative equation for fragmentation functions called MLLA as well as its solutions.

In Chapter 7, a new approach to access the properties of medium created in heavy ion collisions at the LHC is proposed, namely by studying change of the hadronic composition of jets. As a theoretical framework, we use the formalism from Chapter 6 supplemented by the radiative energy loss model of Borghini and Wiedemann. We analyze the impact of the modification of parton shower caused by the medium on the abundances of pions, kaons and protons. We provide predictions for the hadronic spectra and ratios which can be tested as soon as the data from the ALICE experiment is available.

The summary of the Thesis is given in Chapter 8, which is followed by three appendices.

The original work, presented in this Thesis, is based on the following publications

- **"Heavy flavour production in DGLAP improved saturation model"**
  K. J. Golec-Biernat and S. Sapeta, Phys. Rev. D **74**, 054032 (2006)

- **"QCD traveling waves beyond leading logarithms"**
  R. B. Peschanski and S. Sapeta, Phys. Rev. D **74**, 114021 (2006)

- **"Jet hadrochemistry as a characteristic of jet quenching"**
  S. Sapeta and U. A. Wiedemann, arXiv:0707.3494 [hep-ph], CERN-PH-TH-2007-111 (2007)
  to be published in Eur. Phys. J. C

Chapter 1

Introduction

1.1 QCD essentials

Quantum Chromodynamics (QCD) [1–4] is a non-Abelian local gauge theory describing the strong interactions of quarks and gluons. The Lagrangian of QCD is required to be invariant under the transformations from the SU(3) group. The postulate of the SU(3) color symmetry stems from the fact that only color singlet states are observed in experiment. Indeed in nature we have mesons ($q\bar{q}$) and baryons (qqq) rather than free quarks. Consequently, all the properties of the particles that we measure in experiment are color-independent.

The SU(3) group is a Lie group specified by eight generators T^a, which form the Lie algebra [1]

$$[T^a, T^b] = if^{abc}T^c, \tag{1.1}$$

where f^{abc} are called the structure constants of the group and $a, b, c = 1, \ldots, 8$. Two representations (R) of the SU(3) group are of particular importance. The first is the *fundamental representation* ($R \equiv F$). The generators in this representations are the 3×3 matrices $T^a_{mn}(F) = \frac{1}{2}\lambda^a_{mn}$, where $m, n = 1, 2, 3$ and λ^a are the Gell-Mann matrices. The quark is a three-dimensional vector in the color space, with colors being red, green, blue. The elements of the SU(3) group in the fundamental representation act on a quark state and change its color. The second important representation is the *adjoint representation* ($R \equiv A$). Here, the generators have the form of the 8×8 matrices given by $T^a_{bc}(A) = -if^{abc}$. This matrices act in the eight-dimensional space of gluon states. For any representation R one can construct an object $\sum_a T^a_{ik}(R)T^a_{kj}(R) = C_R\delta_{ij}$ called the quadratic Casimir invariant. The value of the constant C_R in the fundamental representation is given by $C_F = (N_c^2 - 1)/(2N_c)$ whereas in the adjoint representation by $C_A = N_c$, where N_c is the number of colors. Therefore, for the case of SU(3) we have $C_F = \frac{4}{3}$ and $C_A = 3$.

The QCD Lagrangian density reads [1]

$$\mathcal{L} = -\frac{1}{4}\mathrm{Tr}\left[F_{\mu\nu}\,F^{\mu\nu}\right] + \sum_f \bar{q}^f_m \left(i\not{D} - m_f\right)_{mn} q^f_n + \mathcal{L}_{\text{gauge-fixing}} + \mathcal{L}_{\text{ghost}}, \tag{1.2}$$

with $F_{\mu\nu} = F^a_{\mu\nu}\,T^a$ where

$$F^a_{\mu\nu} = \left[\partial_\mu A^a_\nu - \partial_\nu A^a_\mu - g\,f^{abc}A^b_\mu A^c_\nu\right]. \tag{1.3}$$

The quark field with flavor f and mass m_f is denoted by q^f whereas the gluons fields by A_μ, where μ, ν are the Lorentz indices. The sum in Eq. (1.2) runs over the number of active flavors n_f. We have also introduced the notation $\not{D} \equiv \gamma^\mu D_\mu$, where γ^μ are the Dirac matrices satisfying $\{\gamma^\mu, \gamma^\nu\} = 2g^{\mu\nu}$,

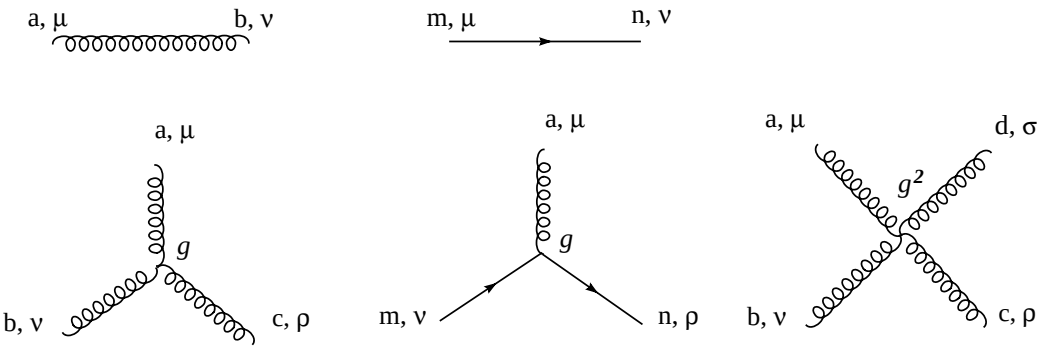

Figure 1.1: Feynman graphs for QCD in the ghost-less gauge. The solid lines represent quarks whereas the curly lines correspond to gluons.

with the metric $g^{\mu\nu} = \mathrm{diag}(1, -1, -1, -1)$. By D_μ we denote the covariant derivative, which depends on the fields A^a_μ and is defined as

$$D_\mu[A] = \partial_\mu + i\, g\, A^a_\mu\, T^a. \tag{1.4}$$

The strength of the interaction is specified by g, which is called the *coupling constant*. Hereafter, we will use also the quantities

$$\alpha_s = \frac{g^2}{4\pi} \quad \text{or} \quad \bar{\alpha}_s = \frac{N_c}{\pi}\alpha_s. \tag{1.5}$$

The first two terms in the Lagrangian (1.2) describe the quark fields q^f_n, the gluon fields A^a_μ and their interactions. This part of the Lagrangian is by construction invariant with respect to the SU(3) group transformation [3]

$$q'(x) = U(x)\, q(x), \quad F'_{\mu\nu}(x) = U(x) F_{\mu\nu}(x)\, U^{-1}(x), \tag{1.6}$$

$$[D_\mu[A]\, q(x)]' \equiv D_\mu[A']\, q'(x) = U(x) D_\mu[A]\, q(x), \tag{1.7}$$

where $U(x) = \exp\left(\theta^a(x)\, T^a\right)$ is in the fundamental representation. The invariance of the Lagrangian density (1.2) with respect to the gauge transformations (1.6) and (1.7) means that there is an infinite number of configurations of fields $A_\mu(x)$ which are physically equivalent. These equivalent fields are related to each other by the gauge transformation.

The quantization of the gauge fields is possible only if some specific gauge is chosen and fixed. This is necessary to avoid double counting, *i.e.* considering the physically indistinguishable configurations. Such a quantization with constraint, by the method of Lagrange multipliers, gives rise to the third term in Eq. (1.2). In addition, in the case of the non-Abelian theory such as QCD, for some gauges, one is forced to introduce extra fields into the formalism, the so called *ghosts*, which are described by the last term in Eq. (1.2).

In particle physics we are interested in calculating quantities such as decay widths or cross sections for scatterings. They all depend on the squared amplitudes for the transition between some incoming and outgoing states. In the region of small coupling one can expand the amplitude in powers of g and calculate terms order by order. This theoretical framework is called *perturbative QCD* (pQCD). The natural language of the perturbative theory are Feynman graphs representing propagation of quarks and gluons as well as their interactions. For the sake of example, we depict in Fig. 1.1 the propagators of the gluon and the quark as well as the quark-gluon, three-gluon and four-gluon vertices. The appearance of the three-gluon vertex is a nontrivial property of QCD since it means that the self-gluon interaction

is present already at the lowest order $\mathcal{O}(g)$. The three-gluon vertex arises from the third, non-Abelian term in the field strength tensor (1.3). The Feynman graphs together with additional set of rules allow to write the expression for amplitude in an efficient an unique way. One should, however, keep in mind that the Feynman rules may differ significantly in different gauges. This proves to be very useful since it allows to choose the most suitable gauge for each problem.

In the regime of large coupling other techniques must be used such as *e.g.* lattice QCD. In this approach the theory is formulated in the Euclidean space, which is in turn discretized into the four-dimensional lattice with spacing a. Local gauge invariance is preserved. The action obtained by this procedure is used to calculate the expectation values of various operator associated, for instance, with hadronic masses or $q\bar{q}$ potential. The lattice spacing a must be much smaller than the size of the studied object, *e.g.* the hadron radius. In the following, we will refer to all the effects which cannot be studied in the perturbative theory as the *non-perturbative effects*.

We see that the value of the coupling is of crucial importance from the point of view of applicability of the perturbative QCD techniques. But so far g is a constant so how one can speak about various limits of QCD? It turns out that when one tries to calculate amplitudes at higher orders one encounters the expressions containing momentum integrals which are divergent as momentum goes to infinity (UV divergences). The integrals can be formally calculated, *e.g.* by introducing a cut-off parameter μ. Such procedure is called *regularization* and exists in many various versions. The expressions which are obtained have the terms which are finite and the terms which are infinite after removing the cut-off. The reason why the divergent terms appear is that the coupling g from the Lagrangian (1.2), which we call "bare" coupling, is not a correct expansion parameter and has to be redefined. The bare coupling absorbs the divergent terms and gives finite, experimentally measured quantity which we call "physical coupling". This procedure is called *renormalization*. Similar procedure has to be also applied to the bare mass an the bare fields from (1.2). Subsequently, the Lagrangian density (1.2) can be rewritten in terms of physical (*i.e.* renormalized) quantities $\Phi_{\text{ren}}(\mu)$, $m_{\text{ren}}(\mu)$ and $g_{\text{ren}}(\mu)$. This new Lagrangian naturally splits into two parts. The first part has the form which is identical to (1.2) but with the physical quantities instead of bare. The second part consists of the so called counterterms which are formally divergent. These divergences cancel however the divergences from the "bare-like" part so the perturbation theory based on the renormalized Lagrangian gives finite results. The problem is, however, not fully solved since we have an arbitrary parameter μ in the Lagrangian. Moreover, the Lagrangian depends on the details of the regularization procedure. Such a situation is in principle allowed provided that we require that all observables are independent of the choice μ. This requirements leads to the *renormalization group equations*. One of them determines the evolution of the coupling

$$\mu^2 \frac{\partial \alpha_s}{\partial \mu^2} = \beta(\alpha_s). \tag{1.8}$$

The function $\beta(\alpha_s)$ introduced above has a perturbative expansion. For the case of perturbative QCD ($\alpha_s \ll 1$) this function is negative, $\beta(\alpha_s) < 0$, which means that the coupling decreases with increasing μ^2. This is a fundamental property of the theory, called *asymptotic freedom*, since due to the smallness of the coupling at high energies quarks behave effectively as free particles. In contrast, in Quantum Electrodynamics (QED) $\beta(\alpha_{\text{em}}) > 0$ and the coupling grows with the scale. At the lowest order $\beta(\alpha_s) = -b\alpha_s^2$ where $b = (11C_A - 2n_f)/(12\pi)$ and the Eq. (1.8) can be solved analytically giving

$$\alpha_s(\mu^2) = \frac{1}{b \ln\left(\frac{\mu^2}{\Lambda^2}\right)}. \tag{1.9}$$

The constant Λ is a fundamental parameter of QCD. This is, by definition, the scale at which the coupling calculated perturbatively diverges. Λ can be determined from experiment. Its value depends, however, on the precise definition (which involves *e.g.* the number of flavors and renormalization scheme) and varies between 100 MeV and 300 MeV.

Besides the asymptotic freedom, the second important feature of QCD is *confinement*. This is a non-perturbative phenomenon and has to do with the fact that free quarks or gluons are not observed in experiment. Instead, only the color singlet states of the SU(3) group are registered. Indeed, lattice studies show that the potential between the pair of quarks is linear in energy. Thus, it would require infinite amount of energy to separate the two color charges.

1.2 Space-like branching and deep inelastic scattering (DIS)

We begin our discussion of the high energy limit of QCD from one of the most important processes which has served as a testing ground for the theory right from its origin. Let us consider the scattering of a charged lepton with four-momentum k off a hadron with four-momentum p with the outgoing particles being the electron with momentum k' and anything else. Such a process is called *deep inelastic scattering* (DIS). The lepton and the hadron interact via exchange of a virtual photon [1] like depicted in Fig. 1.2. The emitted photon carries four-momentum q equal to the change of the electron

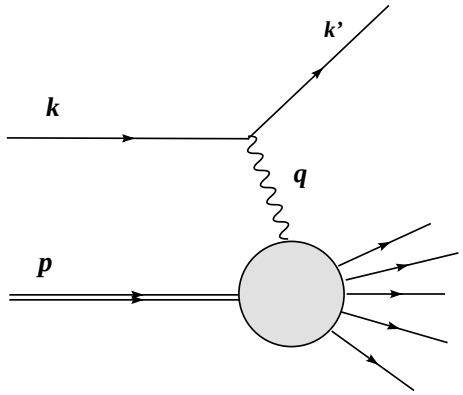

Figure 1.2: Kinematics of deep inelastic lepton-hadron scattering.

momentum $q = k' - k$. One usually defines in this context the following set of invariants [3]

$$\begin{aligned} Q^2 &= -q^2, \\ x &= \frac{Q^2}{2p \cdot q}, \\ \nu &= p \cdot q, \\ y &= \frac{\nu}{k \cdot p}, \end{aligned} \tag{1.10}$$

where $-Q^2$ is the virtuality of the exchanged photon whereas x, known as the Bjorken variable, measures the inelasticity of the process, with $x = 1$ corresponding to the elastic scattering. Finally, y is interpreted in the hadron rest frame as the electron energy transferred to the hadron normalized to the energy of the incoming electron. It is useful to introduce the notation for the center-of-mass energy in the $\gamma^* p$ system, which can be expressed by Q^2 and x

$$W^2 \equiv (p+q)^2 = Q^2 \left(\frac{1}{x} - 1 \right). \tag{1.11}$$

[1] Strictly speaking, also the Z^0 boson exchange can take place. Here we restrict ourselves to the situations with the interaction via virtual photon.

The cross for the DIS process can be factored into a leptonic and a hadronic piece [3, 5]

$$\frac{d\sigma}{dxdQ^2} = \frac{2\pi\alpha_{\text{em}}^2}{x^2 s^2 Q^2} L^{\mu\nu} W_{\mu\nu}, \tag{1.12}$$

where α_{em} is the electromagnetic coupling. The leptonic part can be completely determined from QED, and assuming that only photon is exchanged, we obtain

$$L^{\mu\nu} = 2\left(k^\mu k'^\nu + k^\nu k'^\mu - g^{\mu\nu}\, k\cdot k'\right). \tag{1.13}$$

The hadronic tensor describes the interaction of the virtual photon with a complex target and only general expression for $W_{\mu\nu}$ can be written [3]

$$W_{\mu\nu} = \frac{1}{4\pi}\sum_n \langle p|J_\nu(0)|n\rangle\langle n|J_\mu(0)|p\rangle\,(2\pi)^4\delta^4(q+p-p_n), \tag{1.14}$$

where J_μ is the electromagnetic current and the sum runs over the complete set of final states. Using the conservation of J_μ and the parity conservation one may derive the most general form of the hadronic tensor

$$W^{\mu\nu} = \left(g^{\mu\nu} - \frac{q^\mu q^\nu}{q^2}\right) F_1(x,Q^2) + \left(p^\mu + \frac{1}{2x}q^\mu\right)\left(p^\nu + \frac{1}{2x}q^\nu\right)\frac{1}{\nu}F_2(x,Q^2), \tag{1.15}$$

which leads to the following expression for the DIS cross section

$$\frac{d^2\sigma}{dxdQ} = \frac{4\pi\alpha_{\text{em}}^2}{Q^4}\left\{\left[1+(1-y)^2\right]F_1(x,Q^2) + \frac{1-y}{x}\left[F_2(x,Q^2) - 2xF_1(x,Q^2)\right]\right\}. \tag{1.16}$$

In the above, we have introduced two *structure functions*, F_1 and F_2, which contain the information about the hadron probed by the virtual photon. This functions cannot be calculated within pQCD for the case of the proton which, due to its small mass, is a non-perturbative object.

Alternatively, one can introduce the functions F_T and F_L which are related to the $\gamma^* p$ cross section with the transversely and longitudinally polarized photon, respectively

$$F_T \equiv \frac{Q^2}{4\pi^2\alpha_{\text{em}}}\sigma_T = 2xF_1, \tag{1.17}$$

$$F_L \equiv \frac{Q^2}{4\pi^2\alpha_{\text{em}}}\sigma_L = F_2 - 2xF_1, \tag{1.18}$$

and we also have

$$F_2 = F_T + F_L. \tag{1.19}$$

The expansion (1.16) is general and can be used with any model of the hadron structure. For instance, one may assume that the hadron consists of elementary objects with spin $\frac{1}{2}$, called *partons*, and that the virtual photon interacts with the hadron by interacting electromagnetically with individual partons. This *naive parton model* was proposed before the advent of QCD. Its main prediction was the so called *Bjorken scaling*, observed at that time in the DIS data from SLAC, which means that in the limit $Q^2 \to \infty$ and fixed x the structure function $F_2(Q^2, x) \to F_2(x)$. Moreover, the longitudinal structure function vanishes and we obtain the Callan-Gross relation $F_2(x) = 2xF_1(x)$, or equivalently $F_L(x) = 0$. The x-Bjorken in the naive parton model is equal to the fraction of the proton momentum carried by the struck parton.

From the QCD viewpoint, the partons introduced in the above model should be identified with quarks. However, Quantum Chromodynamics supplements the above picture by introducing gluons.

This leads to the logarithmic violation of the Bjorken scaling, as well as to the nonzero value of F_L. We see already at this stage that the longitudinal structure function probes directly the gluonic content of a hadron. As mentioned above, the structure functions of proton cannot be calculated within the perturbation theory. Nevertheless, what can be determined is how these functions change with Q^2. Before we derive the evolution equations for F_2 let us try to identify which classes of Feynman diagrams give the leading contributions.

1.3 Leading logarithmic approximation (LLA)

Let us consider the situation in which instead of a hadron we have a massless quark as the target. In this case the tensor $W_{\mu\nu}$ may be calculated perturbatively. It is related to the imaginary part of the forward elastic scattering amplitude $T_{\mu\nu}$ by the optical theorem

$$W_{\mu\nu} = \frac{1}{2\pi}\mathrm{Im}\, T_{\mu\nu}. \tag{1.20}$$

Thus, instead of summing over all possible final states it suffices to consider the elastic γ^*–parton scattering. Then, the *parton* structure functions, which we denote as $\hat{F}_i$, can be extracted from $W_{\mu\nu}$ using Eq. (1.15).

Sudakov variables

It proves to be useful to represent all parton four-momenta k in the following form, known as the Sudakov decomposition

$$k_\mu = \alpha\, q'_\mu + \beta\, p'_\mu + k_{\perp\mu}, \tag{1.21}$$

$$k^2 = \alpha\,\beta s - k^2_{\perp\mu}, \tag{1.22}$$

where $s \equiv 2\,p'\cdot q'$ and the vectors q' and p' lie on the light cone whereas $k_\perp$ is perpendicular to both of them

$$q'^2 = p'^2 = 0, \tag{1.23}$$

$$q'^\mu k_{\perp\mu} = p'^\mu k_{\perp\mu} = 0. \tag{1.24}$$

For the case of $\gamma^* p$ (γ^*-parton) scattering we obtain (keeping the notation from the previous section)

$$q_\mu = q'_\mu - x p'_\mu, \qquad\qquad p_\mu = p'_\mu + \frac{m_p^2}{s} q'_\mu \approx p'_\mu, \tag{1.25}$$

where typically the target mass $m_p^2 \ll Q^2$ and $s \approx 2\,p\cdot q$.

1.3.1 Born level

The lowest order (Born level) diagram is shown in Fig. 1.3a. With aid of Eq. (1.20) we obtain $W_{\mu\nu} \sim e_q^2\delta((p+q)^2)$, with e_q denoting the quark electric charge. This, in turn, leads to

$$\hat{F}_2(x) = e_q^2\delta(1-x). \tag{1.26}$$

Hence, in this case $\hat{F}_2$ depends only on x, so we obtain the result compatible with the Bjorken scaling (this time for quark). The delta function means that at the lowest order only the elastic photon-quark collision can occur. This way we have rediscovered the naive parton model for the case of the $\gamma^* q$ scattering.

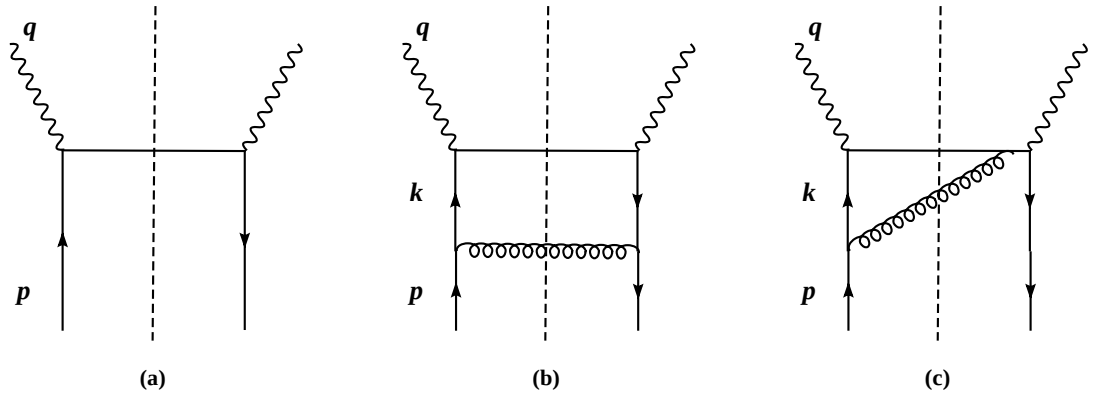

Figure 1.3: Deep inelastic scattering off quark: (a) lowest order (Born level), (b) one gluon emission - ladder diagram (c) one gluon emission - interference diagram.

1.3.2 One and multi-gluon emission

Let us now allow for one gluon being emitted from the quark line. In such a case we encounter two classes of diagrams: the ladder diagram of Fig. 1.3b and the interference diagrams like the one depicted in Fig. 1.3c.

Since this time we work in the framework of QCD, the choice of gauge for the gluon field becomes an issue. It turns out that the most physically transparent picture appears when one adopts the *light-cone gauge* defined as [6]

$$A^a_\mu q'^\mu = 0, \tag{1.27}$$

with q' being the light-like vector defined in Eqs. (1.21), (1.23) and (1.24). This choice of gauge ensures that gluons have only two physical (*i.e.* transverse) polarizations. More importantly, in the light-cone gauge (1.27) the contribution of the ladder diagram of Fig. 1.3b to the hadronic tensor can be schematically written as

$$W_{\mu\nu} \sim \frac{\alpha_s}{2\pi} \int^{Q^2} \frac{d|k^2_\perp|}{|k^2_\perp|}, \tag{1.28}$$

whereas the interference diagram depicted in Fig. 1.3c gives

$$W_{\mu\nu} \sim \frac{\alpha_s}{2\pi} \int^{Q^2} \frac{d|k^2_\perp|}{|k^2_\perp|} |k_\perp|. \tag{1.29}$$

Hence, due to the logarithmic divergence in transverse momentum (or virtuality) the ladder diagram gives the dominant contribution to the tensor $W_{\mu\nu}$ in the case of γ^*–quark scattering. This is known as the *collinear enhancement*. The suppression of the interference diagram with respect to the ladder diagram results from the absence of the second gluon propagator.

The above result can be generalized to the case with n emitted gluons. The dominant contribution comes from the diagram shown in Fig. 1.4a in which each gluon emission provides a singular integral. The corresponding contribution to $W_{\mu\nu}$ reads

$$W_{\mu\nu} \sim \left(\frac{\alpha_s}{2\pi}\right)^n \int_{m^2}^{Q^2} \frac{d|k^2_{\perp n}|}{|k^2_{\perp n}|} \int_{m^2}^{|k^2_{\perp n}|} \frac{d|k^2_{\perp n-1}|}{|k^2_{\perp n-1}|} \cdots \int_{m^2}^{|k^2_{\perp 2}|} \frac{d|k^2_{\perp 1}|}{|k^2_{\perp 1}|} = \frac{1}{n!} \left(\frac{\alpha_s}{2\pi} \ln \frac{Q^2}{m^2}\right)^n, \tag{1.30}$$

where we have introduced an arbitrary small cut-off m^2 on the transverse momentum to regularize the logarithmic divergence. This divergence appears since we consider here the theory with massless quarks.

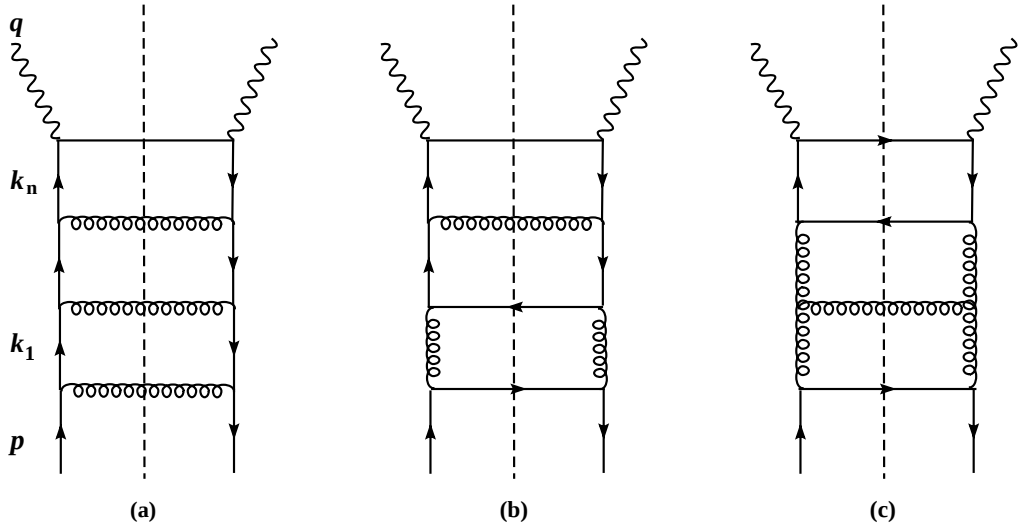

Figure 1.4: Multi-cell ladder diagrams for γ^*–quark deep inelastic scattering.

Formula (1.30) reveals the fundamental idea behind the LLA approach. For the processes in which the hard scale $Q^2 \gg m^2$ is involved, despite the smallness of the coupling, we have $\alpha_s \ln Q^2/m^2 \sim 1$ due to the large collinear logarithms. This, in turn, implies that in order to obtain the full LLA result one has to sum an infinite number of the ladder diagrams. Moreover, the collinear divergent integrals are accompanied by the infrared divergent integrals such that for the diagram of Fig. 1.4a we have [4]

$$W_{\mu\nu} \sim \frac{1}{n!}\left(\frac{\alpha_s}{2\pi}\ln\frac{Q^2}{m^2}\right)^n \times \int_0^1 \frac{d\beta_n}{\beta_n}\,\delta\left(1-\frac{x}{\beta_n}\right)\int_{\beta_n}^1 \frac{d\beta_{n-1}}{\beta_{n-1}}\cdots\int_{\beta_2}^1 \frac{d\beta_1}{\beta_1}\hat{P}_{qq}\left(\frac{\beta_n}{\beta_{n-1}}\right)\hat{P}_{qq}\left(\frac{\beta_{n-1}}{\beta_{n-2}}\right)\cdots\hat{P}_{qq}\left(\frac{\beta_1}{1}\right), \tag{1.31}$$

where β_n is the Sudakov variable (for quark) defined in Eq (1.21) and

$$\hat{P}_{qq}(z) = C_F\,\frac{1+z^2}{1-z} \tag{1.32}$$

is the *unregularized splitting function*. $\hat{P}_{qq}(z)$ corresponds to the process in which the quark changes its momentum from k to zk via gluon emission. Hence, we see that the dominant contribution to the hadronic tensor comes from the ladder diagrams with strongly ordered transverse momenta

$$m^2 \ll |k^2_{\perp\,1}| \ll |k^2_{\perp\,2}| \cdots \ll |k^2_{\perp\,n}| \ll Q^2. \tag{1.33}$$

The longitudinal momentum fractions decrease when one moves along the ladder from the quark to the photon

$$1 \geq \beta_1 \geq \beta_2 \cdots \geq \beta_n \geq x. \tag{1.34}$$

The energy divergence which appears in Eq (1.32) vanishes if one adds the contributions coming from self-energy (virtual) corrections to the ladder diagrams as well as the corrections to the photon vertex. This leads to the *regularized splitting functions*. In general, they have a perturbative expansion

$$P_{qq}(z,\alpha_s) = P^{(0)}_{qq}(z) + \frac{\alpha_s}{2\pi}\,P^{(1)}_{qq}(z) + \ldots. \tag{1.35}$$

To obtain the complete picture of the deep inelastic γ^*–quark scattering at the leading order, one should also include other types of ladder diagrams like those shown in Figs. 1.4b and 1.4c. They contain the remaining possible emissions with respect to $q \to qg$ described by $P_{qq}(z)$. These are: $q \to gq$ with the corresponding splitting function denoted as $P_{gq}(z)$, $g \to qq$ with $P_{qg}(z)$ and finally $g \to gg$ associated with $P_{gg}(z)$. The full set of the regularized, leading order (LO) splitting functions reads [7]

$$P_{qq}^{(0)}(x) = C_F \left[\frac{1+x^2}{(1-x)_+} + \frac{3}{2}\delta(1-x) \right], \tag{1.36}$$

$$P_{qg}^{(0)}(x) = T_R \left[x^2 + (1-x)^2 \right], \quad T_R = \frac{1}{2}, \tag{1.37}$$

$$P_{gq}^{(0)}(x) = C_F \left[\frac{1+(1-x)^2}{x} \right], \tag{1.38}$$

$$P_{gg}^{(0)}(x) = 2C_A \left[\frac{x}{(1-x)_+} + \frac{1-x}{x} + x(1-x) \right] + \delta(1-x)\frac{11C_A - 4n_f T_R}{6}, \tag{1.39}$$

where we have introduced the *plus distribution* defined by the integral with a smooth function $f(x)$ as

$$\int_0^1 dx \, \frac{f(x)}{(1-x)_+} \equiv \int_0^1 dx \, \frac{f(x) - f(1)}{1-x}. \tag{1.40}$$

The DIS splitting functions have been so far calculated also at the next-to-leading (NLO) [8,9] and the next-to-next-to leading order (NNLO) [10, 11].

The leading order *unregularized* splitting functions $\hat{P}_{ik}^{(0)}(x)$ (*i.e.* the functions from Eqs. (1.36)-(1.39) without the plus prescription and the terms proportional to $\delta(1-x)$) have the interpretation of the probabilities of splitting of the parton k into the parton i with the momentum fraction x and the parton j with momentum fraction $1-x$. Therefore, these functions are positive definite for $0 < x < 1$.

Finally, we can write the expression for the quark structure function at LLA

$$\hat{F}_2(x, Q^2, m^2) = e_q^2 \, x \left[\delta(1-x) + \sum_n \frac{1}{n!} \left(\frac{\alpha_s}{2\pi} \ln \frac{Q^2}{m^2} \right)^n \mathcal{P}_n(x) \right], \tag{1.41}$$

where by $\mathcal{P}_n(x)$ we denoted the multiple integral like the one from the second line of Eq. (1.31) but summed over all possible combinations of the regularized splitting functions.

1.4 Collinear factorization

The quark structure function $\hat{F}_2$ calculated within LLA exhibits collinear (or mass) divergences which have been temporarily regularized in Eq. (1.41) by introducing the cut-off m^2. The appearance of the collinear divergences can be understood by noticing that the limit $k_\perp \to 0$ corresponds to the soft part of the strong interaction for which the perturbation theory approach breaks down. Below certain momentum scale one cannot speak about quarks and gluons any longer. Quarks and gluons are not, however, directly observed in experiment. Instead, they constitute hadrons. The distributions of partons inside hadrons (hereafter *parton distribution functions* or *pdf*s), denoted by $q(x, Q^2)$ and $g(x, Q^2)$ for quark and gluons respectively, are not calculable in pQCD since they contain input from non-perturbative regime of the theory. Nevertheless, the hadron structure function can be written as the convolution of the quark and the gluon structure functions, $\hat{F}_2^q$ and $\hat{F}_2^g$, at some scale $\mu_F^2 \gg \Lambda^2$ with $q(x, \mu_F^2)$ and $g(x, \mu_F^2)$ distributions which absorb the collinear divergences

$$F_2^{\text{hadron}}(x, Q^2) = x \int_x^1 \frac{dz}{z} \left\{ \sum_{q,\bar{q}} q(z, \mu_F^2) \hat{F}_2^q(\frac{x}{z}, Q^2, \mu_F^2) + g(z, \mu_F^2) \hat{F}_2^g(\frac{x}{z}, Q^2, \mu_F^2) \right\}, \tag{1.42}$$

where the sum runs over all flavors of quarks and anti-quarks. The above formula is a non-trivial property of QCD which comes under the name of the *collinear factorization theorem*. It has been proved to all orders in α_s [12].

Collinear factorization deals with the logarithmic singularities. There are, however, also regular terms in $\hat{F}^q$ and $\hat{F}^g$ which are to a certain degree arbitrary. For instance, some of them may be absorbed into the quark or gluon distribution, which alone are not observables. This defines the *factorization scheme*. In particular, in the *DIS factorization scheme* all gluon contribution is absorbed into the quark distribution and the structure function acquires especially simple form

$$F_2^{\text{hadron}}(x,Q^2) = x\sum_{q,\bar{q}} e_q^2 q(x,Q^2). \tag{1.43}$$

What makes the concept of parton distribution functions the most attractive is the fact that once they are determined for a given hadron from one process, they can be used in any other process. This means that parton distribution functions have the property of being universal.

1.5 DGLAP evolution equation

The result (1.42) has to be independent of the value μ_F^2 since the factorization scale can be chosen arbitrary provided that it stays in the perturbative regime. This leads to the condition that the derivative of the right hand side of Eq. (1.42) with respect to μ_F^2 must be identically zero. Hence, we obtain the evolution equations for the quark and the gluon density [7, 13–15]

$$\mu^2\frac{\partial}{\partial\mu^2}\begin{pmatrix} q(x,\mu^2) \\ g(x,\mu^2)\end{pmatrix} = \frac{\alpha_s(\mu^2)}{2\pi}\int_x^1\frac{dz}{z}\begin{pmatrix} P_{qq}(\frac{x}{z},\alpha_s(\mu^2)) & 2n_f P_{qg}(\frac{x}{z},\alpha_s(\mu^2)) \\ P_{gq}(\frac{x}{z},\alpha_s(\mu^2)) & P_{gg}(\frac{x}{z},\alpha_s(\mu^2))\end{pmatrix}\begin{pmatrix} q(z,\mu^2) \\ g(z,\mu^2)\end{pmatrix}, \tag{1.44}$$

where by $q(x,\mu^2)$ we mean the sum of quarks and anti-quarks of all flavors, *i.e.* the so called *singlet distribution*. The above equation is known as the Dokshitzer-Gribov-Lipatov-Altarelli-Parisi (DGLAP) equation [7, 13–15] and is an analogue of the renormalization group equation for evolution of the running coupling $\alpha_s(\mu^2)$. Similarly to the renormalization group equation it allows to calculate the change of the function with scale but the absolute value at a given scale cannot be determined without specifying an initial condition which is not provided by the theory itself.

1.5.1 Determination of parton distribution functions from DIS data

As pointed out at the end of Section 1.4, determination of pdfs is of great practical relevance. Therefore, huge effort is being constantly made by many groups, which provide various sets of pdfs, to refine their results. Among the recent ones, MRST2006 [16] and CTEQ6.5 [17] sets of pdfs are the most common. The strategy usually adopted is the following. One parametrizes the quark and gluon distribution functions at some reference scale Q_0^2 in a rather general form, for instance $\sum_i A_i x^{\alpha_i}\sum_k B_k(1-x)^{\beta_k}$ in the case of MRST. The parameters are determined from the global fit to the experimental data, with the DIS data being the most important input. The values of pdfs at scales different than Q_0^2 are calculated by solving numerically the DGLAP equations (1.44). This is done currently up to the next-to-next-to leading order. Typically, Λ is left as a free parameter so this is also a method to pin down the value of this fundamental parameter of QCD.

1.5.2 Solution for gluon density at low x

The leading order DGLAP equation can be solved analytically with help of the Mellin transform. In this Thesis we are interested in the high energy limit of QCD, which for the case of DIS means that

W^2 is large. This, in turn, via the relation (1.11), corresponds to low values of x. It turns out that for such a case quarks may be neglected in the first approximation and we obtain from Eq. (1.44) the diagonal equation for the gluon density

$$\mu^2 \frac{\partial g(x,\mu^2)}{\partial \mu^2} = \frac{\alpha_s(\mu^2)}{2\pi} \int_x^1 \frac{dz}{z} P_{gg}^{(0)}(z) g\Big(\frac{x}{z}, \mu^2\Big). \tag{1.45}$$

This equation can be written in a more compact form after introducing the variable t, which absorbs the one-loop running coupling (1.9)

$$t = \frac{1}{2\pi b} \ln \frac{\ln(\mu^2/\Lambda^2)}{\ln(Q_0^2/\Lambda^2)}, \tag{1.46}$$

where Q_0^2 is the starting scale of the evolution at which the initial condition must be specified. The DGLAP equation becomes

$$\frac{\partial x g(x,t)}{\partial t} = \int_x^1 dz P_{gg}^{(0)}(z) \, \frac{x}{z} g\Big(\frac{x}{z}, t\Big). \tag{1.47}$$

Taking the Mellin transform, defined and discussed in Appendix A, leads to

$$\frac{\partial \tilde{g}_n(t)}{\partial t} = \tilde{\gamma}_n^{(0)} \, \tilde{g}_n(t), \tag{1.48}$$

where the quantity $\tilde{\gamma}_n^{(0)}$, defined as the logarithmic derivative of the Mellin moment of the gluon distribution $\tilde{g}_n(t)$, is called the *anomalous dimension* and for the case of Eq. (1.47) it coincides with the Mellin transform of the splitting function

$$\tilde{\gamma}_n^{(0)} = \int_0^1 dz \, z P_{gg}^{(0)}(z) z^{n-1}. \tag{1.49}$$

Due to properties of the Mellin transform (see Appendix A) the DGLAP equation (1.47) becomes an algebraic equation (1.48), which can be instantly solved. After applying the inverse Mellin transform we arrive at

$$x g(x,t) = \int_{\mathcal{C}} \frac{dn}{2\pi} \, \tilde{g}_n(0) \, \exp\Big(n \ln(1/x) + \tilde{\gamma}_n^{(0)} t\Big), \tag{1.50}$$

where $\tilde{g}_n(0)$ is the Mellin moment of the initial condition and the integration contour, $\mathcal{C}$, runs parallel to the imaginary axis to the right of all singularities of the integrand. In the double logarithmic limit (DLLA), $Q^2 \to \infty$ and $x \to 0$, the above integral can be calculated by the saddle point method and we obtain [18]

$$g(x,Q^2) \sim \frac{1}{x} \exp \sqrt{\frac{4N_c}{\pi b} \frac{\ln Q^2/\Lambda^2}{\ln Q_0^2/\Lambda^2} \ln \frac{1}{x}}. \tag{1.51}$$

Hence, indeed we see that the gluon density is enhanced in the region of small x growing faster than any power of $\ln(1/x)$.

Chapter 2

Deep inelastic scattering at low x

The LLA description of the DIS processes is supposed to be valid when the photon virtuality Q^2 is much grater than any other scale. In such case terms of the type $\alpha_s \ln Q^2 \sim 1$ give the dominant contribution to the cross section. However, in the region of small x, which in the case of DIS, through the relation (1.11) is equivalent to the limit of large $W^2 \simeq Q^2/x$, the energy logarithms start to be important. The LLA formalism contains only those energy logarithms which are accompanied by the collinear logs. Hence, for the case of small x it DIS should, in principle, work correctly in the double logarithmic limit. As we see in Fig. 2.1, the kinematic region of HERA is not of DLLA type since when we decrease x we reduce at the same time Q^2 instead of increasing it. In this case the single energy logarithms should give the most important contribution. Consequently, one would expect that in order to properly describe DIS at low x a scheme in which the single logarithmic terms of the type $\alpha_s \ln W^2$ are resummed should be designed. Such a resummation, which in addition keeps exact transverse momentum dependence, has been accomplished by Balitsky, Fadin, Kuraev and Lipatov [19–22]. It results in the evolution equation in energy. At the leading order, the resummed terms are of the type

$$\left(\bar{\alpha}_s \ln \frac{W^2}{W_0^2}\right)^n, \tag{2.1}$$

with $\bar{\alpha}_s$ defined in Eq. (1.5), and W_0^2 being a constant introduced for dimensional reasons. At the next-to-leading order, corrections suppressed by one power of the coupling are added

$$\bar{\alpha}_s \left(\bar{\alpha}_s \ln \frac{W^2}{W_0^2}\right)^n. \tag{2.2}$$

In Section 2.1 we discuss various facts concerning the BFKL equation at the leading and higher orders. We introduce the framework of the $k_\perp$ factorization in which the BFKL description of the high energy collision is formed. The relation between the $k_\perp$ factorization and the collinear factorization is established in Section 2.2. The BFKL equation is supposed to be valid only in the limit of the dilute system of gluons. The possible approaches to handle the dense gluonic system are discussed in Section 2.3.

2.1 $k_\perp$ factorization and BFKL evolution equation

The amplitude for elastic $\gamma^* p$ scattering in the limit of large W^2 (or equivalently small x) can be represented diagrammatically as in Fig. 2.2a, where $t \approx -\mathbf{q}^2$ is the square of the total momentum transfer which is, in turn, dominated by its transverse component $\mathbf{q}$. The inclusive DIS cross section is

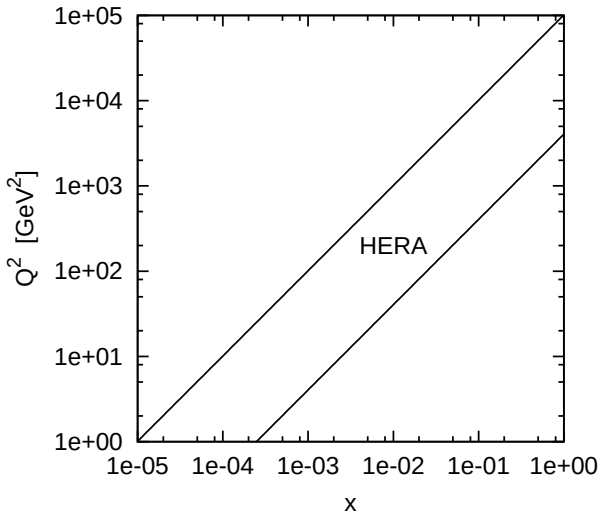

Figure 2.1: HERA kinematic plane.

obtained via the optical theorem as a cut of this diagram [23]

$$\sigma_{T,L}(W^2) = \frac{\mathcal{G}}{(2\pi)^4}\int \frac{d^2\mathbf{k}_1}{\mathbf{k}_1^2}\frac{d^2\mathbf{k}_2}{\mathbf{k}_2^2}\Phi_{T,L}(\mathbf{k}_1,\mathbf{q})\Phi_p(\mathbf{k}_2,\mathbf{q})\mathcal{F}(W^2,\mathbf{k}_1,\mathbf{k}_2,\mathbf{q})\Big|_{\mathbf{q}=0}, \tag{2.3}$$

where $\mathbf{k}_\mathrm{i}$ and $\mathbf{q}$ are the transverse momenta and $\Phi_{T,L}(\mathbf{k}_1,\mathbf{q})$ and $\Phi_p(\mathbf{k}_2,\mathbf{q})$ are the so called photon and proton *impact factors*. The above equation is known as the $k_\perp$ *factorization formula*. The constant $\mathcal{G}$ is a color factor which depends on the process.

The central blob in Fig. 2.2a corresponds to the function $\mathcal{F}(W^2,\mathbf{k}_1,\mathbf{k}_2,\mathbf{q})$ and represents the object exchanged between γ^* and the proton, which is called the *hard Pomeron*. It is by definition a color singlet state and, in the BFKL description of high energy collisions, it has the form of a gluon ladder as depicted in Fig. 2.2b for the forward case, $\mathbf{q}=0$. The BFKL equation is an equation for $\mathcal{F}(W^2,\mathbf{k}_1,\mathbf{k}_2,\mathbf{q})$. At the leading order and in the forward case it has the form [23]

$$\omega\tilde{\mathcal{F}}(\omega,\mathbf{k}_1,\mathbf{k}_2,0) = \delta^2(\mathbf{k}_1-\mathbf{k}_2) + \mathcal{K}_0 \bullet \tilde{\mathcal{F}}(\omega,\mathbf{k}_1,\mathbf{k}_2,0), \tag{2.4}$$

where the kernel $\mathcal{K}_0$ is the integral operator defined as

$$\mathcal{K}_0 \bullet \tilde{\mathcal{F}}(\omega,\mathbf{k}_1,\mathbf{k}_2,0) = \frac{\bar{\alpha}_s}{\pi}\int \frac{d^2\mathbf{k}'}{(\mathbf{k}_1-\mathbf{k}')^2}\left[\tilde{\mathcal{F}}(\omega,\mathbf{k}',\mathbf{k}_2,0) - \frac{\mathbf{k}_1^2}{\mathbf{k}'^2+(\mathbf{k}_1-\mathbf{k}')^2}\tilde{\mathcal{F}}(\omega,\mathbf{k}_1,\mathbf{k}_2,0)\right], \tag{2.5}$$

and $\tilde{\mathcal{F}}(\omega,\mathbf{k}_1,\mathbf{k}_2,0)$ is the Mellin transform of $\mathcal{F}(W^2,\mathbf{k}_1,\mathbf{k}_2,0)$. The first term on the right hand side of Eq. (2.5) corresponds to the emission of the real gluon with transverse momentum $\mathbf{k}'$ whereas the second describes the virtual contribution.

The leading order BFKL equation (2.4) was derived in the *multi-Regge kinematics*

$$\alpha_i \gg \alpha_{i+1}, \qquad\qquad |l_{\perp\, i}| \simeq |l_{\perp\, i+1}| \sim \sqrt{s_0}, \tag{2.6}$$

where we exploited the Sudakov decomposition (1.21) for the momenta of the horizontal gluons from Fig. 2.2b, $l_i = \alpha_i p' + \beta_i q' + l_{\perp\, i}$. The constant $\sqrt{s_0} \ll W$, which cannot be determined at the leading order, is of the magnitude of a typical transverse momentum. It is not difficult to check, using Eqs. (1.21) and (1.22), that the strong ordering in α_i leads to oriented in the opposite direction ordering

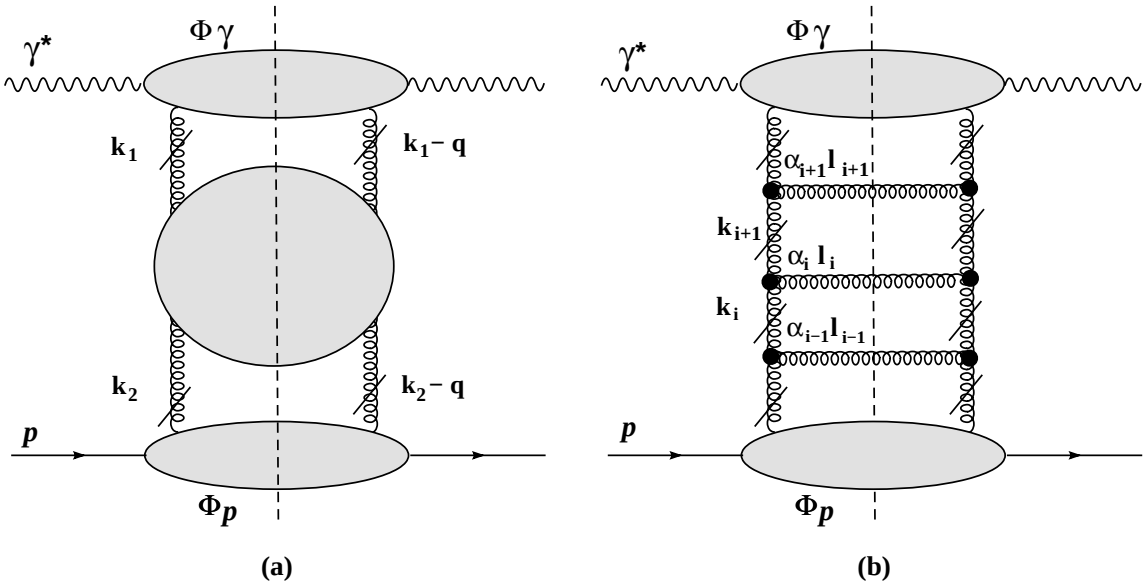

Figure 2.2: Deep inelastic scattering in the high energy limit: (a) structure of $\gamma^* p$ amplitude (b) exchange of the BFKL Pomeron.

in β_i. Finally, when the light-like vectors p' and q' are chosen to be parallel to the z axis in the $\gamma^* p$ collinear frame, we obtain $y_i - y_{i+1} \simeq \ln \alpha_i/\alpha_{i+1}$, where

$$y_i = \frac{1}{2} \ln \frac{E_i + l_{z,i}}{E_i - l_{z,i}} \tag{2.7}$$

is the physical rapidity. Hence, the first condition from Eq. (2.6) is equivalent to the strong ordering in rapidity

$$y_i \gg y_{i+1}. \tag{2.8}$$

In contrast to the DGLAP equation, here the transverse momenta are not order. They are instead integrated over the whole phase space. It is worth to mention that there is no collinear divergence in the BFKL equation (2.4) since the expression in the square brackets in Eq. (2.5) compensates the logarithmic divergence of the integral as $\mathbf{k}' \to \mathbf{k}_1$.

The vertical gluons are *reggeized*. This means that the standard gluon propagator (in the Feynman gauge) $D_{\mu\nu}(k_i^2) = -ig_{\mu\nu}/k_i^2$ is replaced by

$$D_{\mu\nu}(k_i^2) = -i \frac{g_{\mu\nu}}{k_i^2} \left(\frac{s_{ij}}{s_0} \right)^{\omega(k_i^2)}, \tag{2.9}$$

where $s_{ij} = (l_i + l_{i+1})^2$ and $\alpha_G(k_i^2) = 1 + \omega(k_i^2)$ is the Regge trajectory of the gluon. Gluon reggeization arises as a property of the color octet exchange channel. In Figs. 2.2a and 2.2b reggeization is represented by the dashes on gluon lines.

Another important element introduced in the BFKL equation is the *effective vertex* denoted as $\Gamma^{\sigma_i}_{\mu_i \nu_{i+1}}(k_i, k_{i+1})$ and indicated in Fig. 2.2b by the dark blobs. It is obtained by adding a horizontal gluon with momentum $(k_i - k_{i+1})^{\mu_i}$ to all gluon lines.

The photon impact factor, which appears in the formula (2.3), can be calculated perturbatively. The two graphs which contribute at the leading order are shown in Fig. 2.3. The corresponding expressions

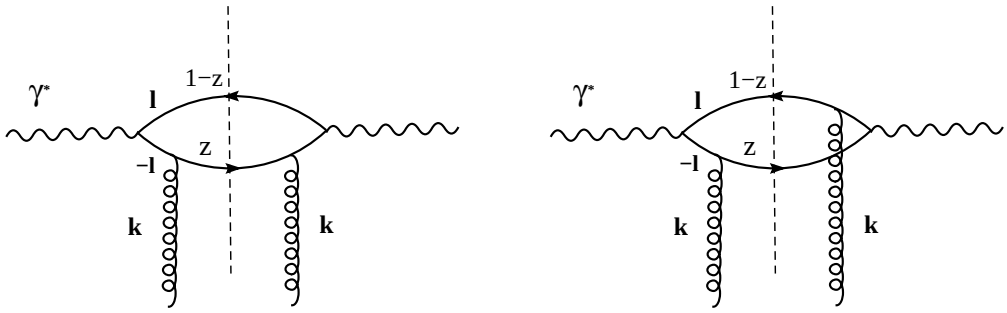

Figure 2.3: The photon impact factors at leading order.

for the transversely and longitudinally polarized photons in the forward case are [5, 23]

$$\Phi_T(\mathbf{k},0) = 4\alpha_{\rm em}\alpha_s \sum_f e_f^2 \int_0^1 dz \int d^2\mathbf{l} \times \left\{ [z^2+(1-z)^2] \left\{ \frac{\mathbf{l}}{D(\mathbf{l})} - \frac{\mathbf{l}+\mathbf{k}}{D(\mathbf{l}+\mathbf{k})} \right\}^2 + m_f^2 \left\{ \frac{1}{D(\mathbf{l})} - \frac{1}{D(\mathbf{l}+\mathbf{k})} \right\}^2 \right\}, \tag{2.10}$$

$$\Phi_L(\mathbf{k},0) = 16\alpha_{\rm em}\alpha_s Q^2 \sum_f e_f^2 \int_0^1 dz \int d^2\mathbf{l}\, z^2(1-z)^2 \left\{ \frac{1}{D(\mathbf{l})} - \frac{1}{D(\mathbf{l}+\mathbf{k})} \right\}^2, \tag{2.11}$$

where $\pm\mathbf{l}$ are the two-dimensional transverse momentum vectors of the quarks in the dipole as depicted in Fig. 2.3 and we also introduced the following notation

$$D(\mathbf{l}) = \mathbf{l}^2 + \bar{Q}^2, \tag{2.12}$$

$$\bar{Q}^2 = z(1-z)Q^2 + m_f^2. \tag{2.13}$$

The sum in Eqs. (2.10) and (2.11) runs over the flavors, f, of the $q\bar{q}$ pair with m_f being the quark (anti-quark) mass.

The proton impact factor has the non-perturbative nature. It proves to be convenient to combine it with the function $\mathcal{F}(x,\mathbf{k}_1,\mathbf{k}_2,0)$ into one object called the *unintegrated gluon distribution*

$$f(x,\mathbf{k}) = \frac{1}{(2\pi)^3} \int \frac{d\mathbf{k}_2}{\mathbf{k}_2^2} \Phi_p(\mathbf{k}_2,0)\mathbf{k}^2 \mathcal{F}(x,\mathbf{k},\mathbf{k}_2,0), \tag{2.14}$$

where, to simplify the notation, we did not write the explicit dependence on the momentum transfer $\mathbf{q}$ in f. In fact, for the purpose of the further discussion it is sufficient to restrict ourselves to the forward case, $\mathbf{q}=0$. This is because in the remaining part of this chapter as well as in Chapters 3–5 we are interested in calculating fully inclusive quantities, which can be obtained from the forward scattering amplitude via the optical theorem (1.20).

The BFKL equation for the Mellin moments of the unintegrated gluon distribution, assuming the spherical symmetry of $\tilde{f}(\omega,\mathbf{k})$ and denoting $k^2 \equiv \mathbf{k}^2$, has the form

$$\omega\tilde{f}(\omega,k^2) = \tilde{f}^0(k^2) + \bar{\alpha}_s k^2 \int_0^\infty \frac{dk'^2}{k'^2} \left\{ \frac{\tilde{f}(\omega,k'^2)-\tilde{f}(\omega,k^2)}{|k'^2-k^2|} + \frac{\tilde{f}(\omega,k^2)}{\sqrt{4k'^4+k^4}} \right\}, \tag{2.15}$$

where the first term corresponds to the case in which only two gluons (*i.e.* the ladder without rungs) are exchanged. The $k_\perp$ factorization formula is now given by

$$\sigma_{T,L}(x,Q^2) = \frac{\mathcal{G}}{2\pi} \int \frac{dk^2}{k^4} \Phi_{T,L}(Q^2,k) f(x,k^2), \tag{2.16}$$

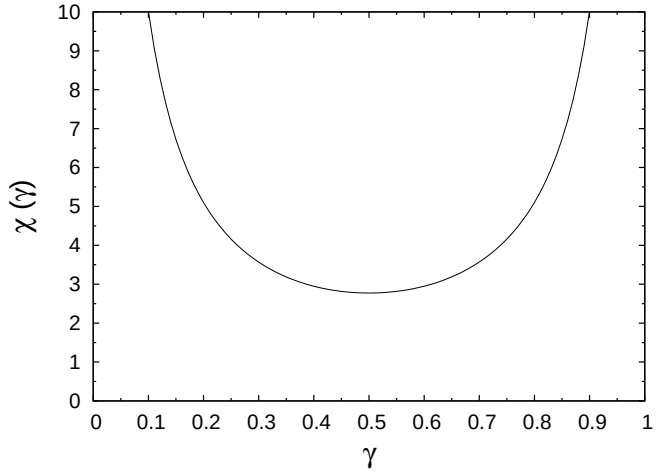

Figure 2.4: Lipatov kernel at leading order.

where the constant for the case of DIS we have $\mathcal{G} = \frac{1}{2}$. Performing the Mellin transform with respect to k^2 leads to the following form of the BFKL equation

$$\omega \hat{f}(\omega, \gamma) = \hat{f}^0(\gamma) + \bar{\alpha}_s \chi(\gamma) \hat{f}(\omega, \gamma), \tag{2.17}$$

with $\chi(\gamma)$ being the Lipatov kernel, shown in Fig. 2.4 and given by

$$\chi(\gamma) = 2\psi(1) - \psi(\gamma) - \psi(1-\gamma), \tag{2.18}$$

where ψ is the digamma function (logarithmic derivative of the Γ function)

$$\psi(\gamma) = \frac{d}{d\gamma} \ln \Gamma(\gamma), \qquad \psi(1) = -\gamma_E, \tag{2.19}$$

and $\gamma_E \approx 0.577$ denotes the Euler constant. It is easy to check that applying the inverse double Mellin transform to Eq. (2.17) results in yet another form of the BFKL equation for the unintegrated gluon distribution

$$\frac{\partial}{\partial \ln(1/x)} f(x, k^2) = \bar{\alpha}_s \, \chi \left(\frac{\partial}{\partial \ln(k^2/k_0^2)} \right) \, f(x, k^2), \tag{2.20}$$

where k_0^2 is an arbitrary constants which only adjust the dimension. The above form of the BFKL equation will turn out to be particularly suitable for our further discussion.

2.1.1 Solution of the leading order BFKL equation in the forward case

The full solution of Eq. (2.4) is given by

$$\tilde{\mathcal{F}}(\omega, \mathbf{k}_1, \mathbf{k}_2, 0) = \sum_{n=0}^{\infty} \int_{-\infty}^{\infty} d\nu \left(\frac{k_1^2}{k_2^2} \right)^{i\nu} \frac{e^{in(\theta_1 - \theta_2)}}{2\pi^2 k_1 k_2} \frac{1}{\omega - \bar{\alpha}_s \chi_n(\nu)}, \tag{2.21}$$

with the transverse vectors represented in the radial coordinates: $\mathbf{k}_1 = (k_1, \theta_1)$ and $\mathbf{k}_2 = (k_1, \theta_2)$. We have introduced also the function

$$\chi_n(\nu) = 2\psi(1) - \psi\left(\frac{n+1}{2} + i\nu \right) - \psi\left(\frac{n+1}{2} - i\nu \right). \tag{2.22}$$

The leading behavior of the result (2.21) at large W^2 corresponds to the large real part in the ω plane. The function $\chi_n(\nu)$ decreases with increasing n so the leading contribution comes from $\chi_0(\nu)$. Moreover, $\chi_0(\nu)$ decreases with increasing ν thus we can expand it and keep only the first two terms

$$\chi_0(\nu) = 4\ln 2 - 14\zeta(3)\nu^2 + \dots, \tag{2.23}$$

where ζ denotes the Riemann zeta function. Hence, the approximated solution becomes

$$\tilde{\mathcal{F}}(\omega, \mathbf{k}_1, \mathbf{k}_2, 0) \approx \frac{1}{\pi k_1 k_2} \int_{-\infty}^{\infty} \frac{d\nu}{2\pi} \left(\frac{k_1^2}{k_2^2}\right)^{i\nu} \frac{1}{\omega - \omega_0 + a^2\nu^2}, \tag{2.24}$$

where we have defined $\omega_0 = 4\bar{\alpha}_s \ln 2$ and $a^2 = 14\bar{\alpha}_s\zeta(3)$. The integrand in Eq. (2.24) has a cut from $-\infty$ to ω_0. After performing the contour integration and applying the inverse Mellin transform we obtain

$$\mathcal{F}(W^2, \mathbf{k}_1, \mathbf{k}_2, 0) \approx \frac{1}{\sqrt{k_1^2 k_2^2}} \left(\frac{W^2}{W_0^2}\right)^{\omega_0} \frac{1}{\sqrt{\pi \ln(W^2/W_0^2)}} \frac{1}{2\pi a} \exp\left(-\frac{\ln^2(k_1^2/k_2^2)}{4a^2 \ln(W^2/W_0^2)}\right). \tag{2.25}$$

The above result exhibits the Regge type of the energy dependence, namely, the leading behavior is power-like $(W^2)^{\omega_0}$. Taking, for instance, the phenomenologically motivated value of the coupling $\bar{\alpha}_s = 0.2$ results in

$$\sigma_{T,L} \sim \mathcal{F} \sim (W^2)^{0.5} \sim x^{-0.5}. \tag{2.26}$$

This corresponds to the intercept $\alpha_{I\!P} = 1 + \omega_0$ greater than one and that is why the exchanged gluon ladder is referred to as the *hard Pomeron*.

The leading order result (2.25) has a number of drawbacks which make it rather academic. Apart from the fixed coupling $\bar{\alpha}_s$ and arbitrary parameter W_0^2 the value $\omega_0 \approx 0.5$ is too large to correctly describe the low x growth of the structure function F_2 measured at HERA. Moreover, the function (2.25) satisfies the diffusion equation, *i.e.* with increasing W^2 the relevant range of transverse momenta broadens as $\sqrt{\ln W^2}$. Thus, it may happen that it enters the non-perturbative, infrared domain. The problem of diffusion is the more severe the larger the difference in $k_\perp$ between the colliding objects. Hence, the collision of two highly virtual photons with $Q_1^2 \sim Q_2^2$ is better suited for studying the BFKL evolution than the DIS scattering where the virtual photon and the proton have significantly different virtualities. All this gives a strong motivation to go the the next-to-leading order.

2.1.2 BFKL kernel at next-to-leading order

As mentioned at the beginning of this chapter, at the next-to-leading order terms with large single logarithms accompanied by en extra power of coupling are added. This amounts to the following change of the Mellin transform of the BFKL characteristic function

$$\chi_{\text{NLL}}(\gamma) = \chi_0(\gamma) + \bar{\alpha}_s \chi_1(\gamma), \tag{2.27}$$

where $\chi_0(\gamma)$ is the leading order result (2.18) and $\chi_1(\gamma)$ the contribution coming from the summation of subleading logarithms of the type (2.2). In principle, the series (2.27) can be extended to any higher order. In practice, however, already the calculation of $\chi_1(\gamma)$ took almost a decade which gives an idea about the complexity of the problem. Nevertheless, it turns out that the structure of the collinear and anti-collinear limit of the kernel (corresponding to $\gamma \to 0$ and $\gamma \to 1$, respectively) can be guessed by imposing on the result the requirement of consistency with the renormalization group.

In order to understand the structure of the higher order corrections, let us consider scattering of two objects with virtualities $-k_1^2$ and $-k_2^2$, were $k_1^2, k_2^2 > 0$. The collinear limit corresponds to the DIS process in which the absolute value of the photon virtuality is much larger than that of the target,

$k_1^2 \gg k_2^2$. The anti-collinear limit matches the symmetric situation, $k_2^2 \gg k_1^2$. Below, following [24], we shall sketch the derivation of these terms of $\chi_1(\gamma)$, which are relevant in the collinear and anti-collinear limit.

First, we notice that using the property of the digamma function, $\psi(\gamma) = -1/\gamma + \psi(1+\gamma)$, and keeping in $\chi_0(\gamma)$ only the terms important at the collinear and anti-collinear limit gives

$$\chi_0^{\text{coll}}(\gamma) = \frac{1}{\gamma} + \frac{1}{1-\gamma}. \tag{2.28}$$

The corresponding result in the momentum space after multiplying by $\bar{\alpha}_s$ has the form

$$K_0^{\text{coll}}(k_1^2, k_2^2) = \bar{\alpha}_s \frac{\Theta\left(k_1^2 - k_2^2\right)}{k_1^2} + \bar{\alpha}_s \frac{\Theta\left(k_2^2 - k_1^2\right)}{k_2^2}. \tag{2.29}$$

The question we want to address in what follows is: which additional contributions to the terms from Eq. (2.28) or equivalently (2.29) can we expect at the next-to-leading order? It turns out that they can come from three sources: the running of the coupling, the non-singular terms in the splitting functions and the choice of the energy scale.

Running coupling effects

The coupling in QCD runs with the energy scale. From the DGLAP evolution we known that the highest scale is usually the proper argument of the coupling. Hence, on the right hand side of Eq. (2.29) the fixed coupling should be replaced by $\bar{\alpha}_s(k_1^2)$ in the first term and by $\bar{\alpha}_s(k_2^2)$ in the second term. The relation between the two has the form

$$\bar{\alpha}_s(k_2^2) = \frac{\bar{\alpha}_s(k_1^2)}{1 + b\,\bar{\alpha}_s(k_1^2) \ln \frac{k_2^2}{k_1^2}}, \tag{2.30}$$

and for large k_1^2 this can be approximated as $\bar{\alpha}_s(k_2^2) \simeq \bar{\alpha}_s(k_1^2) - b\,\bar{\alpha}_s^2(k_1^2) \ln\left(k_2^2/k_1^2\right)$. After applying the Mellin transform to Eq. (2.29) with running couplings, we obtain an extra term with respect to Eq. (2.28) which is a next-to-leading order contribution

$$\chi_1^{\text{coll},\alpha_s}(\gamma) = -\frac{b}{(1-\gamma)^2}. \tag{2.31}$$

Regular terms of splitting function

Taking into account the non-singular terms of the splitting function physically means considering the ladder in which one of the splittings does not satisfy strong ordering in energy (rapidity), that is one large energy logarithm is lost. In the collinear limit of the high energy scattering this implies that the DLLA terms $(\bar{\alpha}_s \ln k^2 \ln(1/x))^n$ are replaced by $\bar{\alpha}_s \ln k^2 (\bar{\alpha}_s \ln k^2 \ln(1/x))^{n-1}$. Resummation of this class of terms will give the contribution suppressed by $\bar{\alpha}_s$ and therefore belonging to $\chi_1(\gamma)$. The additional large collinear logarithm, not accompanied by the large logarithm of energy, after the Mellin transform will convert into the $1/\gamma$ term. Symmetric situation takes place in the anti-collinear limit and altogether we obtain

$$\chi_1^{\text{coll, split}}(\gamma) = \frac{A_1}{\gamma^2} + \frac{A_1}{(1-\gamma)^2}, \tag{2.32}$$

where $A_1 = -11/12$ is the leading (in ω which is the Mellin conjugate of x) term from the gluon splitting function, P_{gg}. In the above, the number of quark flavors, n_f, was set to zero for simplicity.

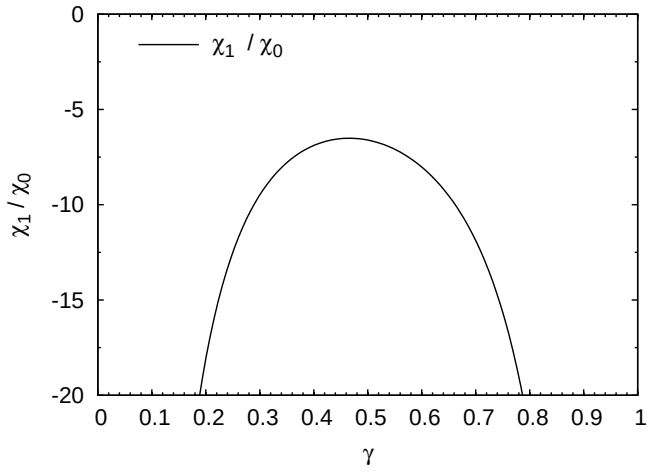

Figure 2.5: Next-to-leading order correction to the BFKL kernel

Energy scale choice

This source of the higher order corrections is more intricate. Let us recall that at the leading order we resume terms of the type $\left(\bar{\alpha}_s \ln\left(W^2/W_0^2\right)\right)^n$, where W^2 is the center of mass energy. So far we did not discuss the constant W_0^2 simply because its choice does not affect the leading order result (the corrections contribute to higher orders). However, since this time we are interested in the next-to-leading order contributions we have to address the issue of W_0^2 more carefully. In the symmetric case, $k_1^2 \approx k_2^2$, the choice $W_0^2 = k_1 k_2$ seems to be the most natural and, at the leading order, one resumes the following terms

$$\left(\bar{\alpha}_s \ln\frac{W^2}{k_1 k_2} \ln\frac{k_1^2}{k_2^2}\right)^n. \tag{2.33}$$

However, if we want to study the collinear (DIS) limit $k_1^2 \gg k_2^2$ we are rather interested in terms $\left(\bar{\alpha}_s \ln(1/x) \ln(k_1^2/k_2^2)\right)^n$, with $x = k_1^2/W^2$, thus the choice $W_0^2 = k_1^2$ is preferred. If use the leading order result resummed with the symmetric scale and scrutinize it in the collinear limit we discover that some additional terms arise, namely

$$\left(\bar{\alpha}_s \ln\frac{W^2}{k_1 k_2} \ln\frac{k_1^2}{k_2^2}\right)^n = \left(\bar{\alpha}_s \ln\frac{1}{x} \ln\frac{k_1^2}{k_2^2}\right)^n + \frac{n}{2}\left(\bar{\alpha}_s \ln\frac{1}{x} \ln\frac{k_1^2}{k_2^2}\right)^{n-1}\left(\bar{\alpha}_s \ln^2\frac{k_1^2}{k_2^2}\right) + \dots. \tag{2.34}$$

The first piece is just the leading order contribution for the asymmetric scale choice. However, the second part, which is formally next-to-leading, contains an additional *double collinear logarithm* accompanied by single coupling. The renormalization group does not allow for existence of such terms so they must be canceled at the next-to-leading order. Therefore, we expect the following contribution to $\chi_1(\gamma)$

$$\chi_1^{\text{coll, scale}}(\gamma) = -\frac{1}{2\gamma^3} - \frac{1}{2(1-\gamma)^3}, \tag{2.35}$$

where $1/\gamma^3$ results from the Mellin transform of the double collinear logarithm and the second term, proportional to $1/(1-\gamma)^3$, arises from considering the anti-collinear limit.

Full solution

The complete next-to-leading order correction to the BFKL kernel in the Mellin space was calculated by Fadin and Lipatov [25] and independently by Ciafaloni and Camici [26]. It has the form

$$\begin{aligned}\chi_1(\gamma) &= -\frac{\pi^2\cos(\pi\gamma)}{4\sin^2(\pi\gamma)(1-2\gamma)}\left(3+\frac{2+3\,\gamma\,(1-\gamma)}{(3-2\,\gamma)(1+2\,\gamma)}\right)\\ &\quad -\frac{b}{2}\left(\chi_0^2(\gamma)-\psi'(\gamma)+\psi'(1-\gamma)\right)+\frac{\psi''(\gamma)}{4}+\frac{\psi''(1-\gamma)}{4}\\ &\quad +\left(\frac{67}{36}-\frac{\pi^2}{12}\right)\chi_0(\gamma)+\frac{3}{2}\zeta(3)+\frac{\pi^3}{4\sin(\pi\gamma)}-\phi(\gamma),\end{aligned} \tag{2.36}$$

where

$$\phi(\gamma)=\sum_{n=0}^{\infty}(-1)^n\left[\frac{\psi(n+1+\gamma)-\psi(1)}{(n+\gamma)^2}+\frac{\psi(n+2-\gamma)-\psi(1)}{(n+1-\gamma)^2}\right]. \tag{2.37}$$

The first line in (2.36) comes from the non-singular term of the splitting function. The first term proportional to b in the second line is a contribution of the running coupling and the rest of this line should be identified with the double collinear logarithmic terms of Eq. (2.35). The last line of (2.36) does not have a clear interpretation and it is free of double or triple poles in γ.

The full NLL contribution, $\chi_1(\gamma)$, is shown in Fig. 2.5. The correction turns out to be huge and produces numerous pathologies. In particular, the Pomeron intercept becomes negative very quickly. For instance, taking $\bar{\alpha}_s = 0.2$ we obtain at the LL saddle point $\gamma = \frac{1}{2}$

$$\omega_{\rm NLL} = \bar{\alpha}_s\chi_0(1/2)(1-6.46) \simeq -0.16, \tag{2.38}$$

the value which has nothing to do with the energy growth seen in the DIS or $\gamma^*\gamma^*$ scattering data. In addition, $\chi_{\rm NLL}(\gamma)$ has now two complex saddle points which replace the value of the $\chi_0(\gamma)$ kernel, that is $\gamma = \frac{1}{2}$. This has a dramatic effect on the cross section, which acquires oscillatory behavior as a function of the transverse momentum already for $\bar{\alpha}_s \simeq 0.05$.

2.1.3 Resummation of terms beyond next-to-leading order

Due to its serious pathologies, the next-to-leading order BFKL kernel is of little practical use. The large corrections brought by $\chi_1(\gamma)$ indicate rather bad convergence of the series. Hence, to obtain a stable result one would probably need to include several higher order terms of the expansion. The corrections beyond NLL are, however, unknown and one should not expect them to be calculated soon. What can be done instead is to try to estimate the leading contributions to each higher order term, N^{n}LL, and resume them.

One of the possible methods to guess these leading contributions is by studying the collinear limit of the BFKL kernel [24, 27–29]. In fact, this approach proves to be very efficient, as we have seen in the preceding section, where in order to guess the NLL corrections the method was applied to the LL kernel. The double logarithmic terms, $1/\gamma^3$, encountered in the NLL kernel written for the scale $W_0^2 = k_1k_2$, are necessary to cancel the corresponding terms produced by the LL kernel when the scale is changed to $W_0^2 = k_1^2$. Such a change from the symmetric to the asymmetric scale is equivalent to the shift of the argument of the kernel, $\gamma \to \gamma - \omega/2$. The requirement of vanishing of the double collinear logarithms in the DGLAP limit, $W_0^2 = k_1^2$, follows from renormalization group and, since it must be satisfied at all orders, one could use the method from Section 2.1.2 to determine terms N^{n}LL in the collinear limit for arbitrary n. However, it is essential to understand that the pathologies similar to those found for the NLL kernel will persist even if we go to a very large but finite N^{n}LL order. This

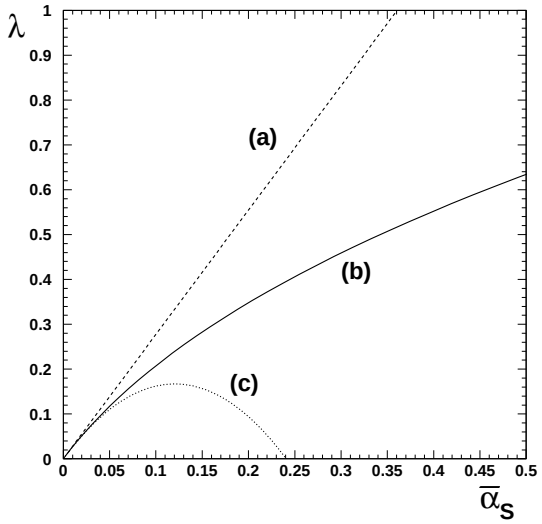

Figure 2.6: The exponent λ from the cross section parametrization $\sigma^{\gamma^* p} \sim x^{-\lambda}$. The dashed curve (a) corresponds to the LL result (2.26). The solid curve (b) results from using the improved LL BFKL kernel (2.39) proposed in [30, 31]. The dotted curve (c) is obtained if only the terms up to the order $\mathcal{O}(\bar{\alpha}_s)$ are kept in the kernel (2.39). The large and negative corrections observed in this case correspond to the pathologies of the NLL BFKL kernel (2.36). Figure from [31].

is because every higher order contribution cancels the double logarithms of the preceding order but brings its own instead. Thus, it is necessary to perform the resummation for all n from 0 to ∞.

Hence, our goal is to modify the BFKL kernel known exactly, for the scale $W_0^2 = k_1 k_2$, at order n in such a way that it is free of double collinear logarithms after changing the scale to $W_0^2 = k_1 k_2$ or, equivalently, after applying the shift of $\gamma \to \gamma + \omega/2$. Moreover, the modified kernel truncated at the order α_s^n has to reproduce the exact N^{n}LL result.

We start from the following modification of the asymmetric kernel, proposed in [30, 31]

$$\chi_0^a(\gamma, \omega) = 2\psi(1) - \psi(\gamma) - \psi(1 - \gamma + \omega). \tag{2.39}$$

In the collinear limit, this kernel behaves as $1/\gamma$, hence it is free of spurious double collinear logarithms. Similarly in the anti-collinear limit. At the symmetric scale the above kernel takes the form

$$\chi_0^s(\gamma, \omega) = 2\psi(1) - \psi\left(\gamma + \frac{\omega}{2}\right) - \psi\left(1 - \gamma + \frac{\omega}{2}\right). \tag{2.40}$$

This result expanded and truncated at $\bar{\alpha}_s$ correctly recovers the singular structure of the exact NLL kernel taken in the collinear limit. In particular, the double logarithmic term $1/\gamma^3$ with the right coefficient is *predicted*. The physical motivation beyond the modification (2.39) is clear and well-founded. It follows form imposing on the leading order BFKL equation (2.15) the kinematic constraint on the transverse momentum of the horizontal gluons from the ladder of Fig. 2.2b, $l_{i\perp}^2 < (\alpha_i/\alpha_{i+1}) k_{i+1\perp}^2$. The improvement obtained by exploiting this condition is truly remarkable, as shown in Fig. 2.6. Yet, we can still obtain a better result.

Suppose that we know the BFKL equation not only at the leading logarithmic accuracy but beyond, up to the order N^{m}LL. The construction of the proper symmetric kernel should proceed as follows. We start from the requirement that at the scale $W_0^2 = k_1^2$ our kernel must be free of double logarithms which means that it has to have the form

$$\chi^{\text{asym}}(\gamma) = \sum_{n=0}^{N} \sum_{k=1}^{n+1} \bar{\alpha}_s^n d_{n,k} D_k(\gamma), \tag{2.41}$$

where the functions $D_k(\gamma)$ have only the divergence $1/\gamma^k$. If we known this kernel up to order m then by the shift we obtain the symmetric kernel. If we now modify our N^{m}LL kernel in analogy with Eq. (2.40) we will unambiguously reproduce all the regular terms $\mathcal{O}(\bar{\alpha}_s^n)$ for $n \leq m$ and the double logarithmic terms $\mathcal{O}(\bar{\alpha}_s^n/\gamma^k)$ for $2n+1-m \leq k \leq 2n+1$ and $n > m$. The subleading double logarithmic terms and regular terms for $n > m$ will depend on the specific choice of the function $D_k(\gamma)$. This ambiguity is reflected in the existence of a number of resummation schemes. The differences between results obtained from various schemes quantifies the uncertainty of the regular parts of $D_k(\gamma)$.

In our study presented in Chapter 5 we will use the NLL BFKL kernels improved by the collinear resummation. The discussion of three specific schemes is given in Section 5.1.

2.2 Relation between collinear and $k_\perp$ factorization

The $k_\perp$ factorization formula for the DIS cross section, given in Eq. (2.16), is valid at low x and at any perturbative value of Q^2. Therefore, in the limit $Q^2 \to \infty$ it should give the result compatible with the DLLA limit of the cross section (or the structure function) obtained in the framework of the collinear factorization.

The photon impact factors given in Eqs. (2.10) and (2.11) can be integrated over $\mathbf{l}$ by introducing the Feynman parameter τ to deal with the products in the denominators

$$\frac{1}{AB} = \int_0^1 d\tau \frac{1}{\left[A + \tau(B-A)\right]^2}\,. \tag{2.42}$$

This leads to [23]

$$\begin{aligned}
\Phi_T(\mathbf{k}) &= 4\pi\alpha_{\rm em}\alpha_s \sum_{q=1}^{n_f} e_q^2 \int_0^1 dz \int_0^1 d\tau \frac{\mathbf{k}^2}{z(1-z)Q^2 + \tau(1-\tau)\mathbf{k}^2} \\
&\qquad \times \left[\tau^2 + (1-\tau)^2\right]\left[z^2 + (1-z)^2\right], \qquad (2.43) \\
\Phi_L(\mathbf{k}) &= 32\pi\alpha_{\rm em}\alpha_s \sum_{q=1}^{n_f} e_q^2 \int_0^1 dz \int_0^1 d\tau \frac{\mathbf{k}^2}{z(1-z)Q^2 + \tau(1-\tau)\mathbf{k}^2} \\
&\qquad \times \left[z(1-z)\tau(1-\tau)\right], \qquad (2.44)
\end{aligned}$$

where, as before, $-Q^2$ is the photon virtuality and $\mathbf{k}$ the transverse momentum of the exchanged gluon, as shown in Fig. 2.3. For simplicity, we assume that quarks are massless. Let us substitute the above expressions into the $k_\perp$ factorization formula (2.16) and differentiate with respect to $\ln Q^2$. In the double logarithmic limit, which corresponds to $Q^2 \to \infty$, the major part of the integration over $k^2 \equiv |\mathbf{k}|^2$ comes from the region $k^2 \ll Q^2$. Hence, after performing the integral over z we may neglect terms suppressed by k^2/Q^2. It turns out that in this limit only the transverse photons contribute. We obtain

$$\frac{\partial F_2(x,Q^2)}{\partial \ln Q^2} = 2\sum_{q=1}^{n_f} e_q^2 \frac{\bar{\alpha}_s}{6} \int_0^1 d\tau \left[\frac{1}{2}\left(\tau^2 + (1-\tau)^2\right)\right] \int^{Q^2} \frac{dk^2}{k^2} f(x,k^2). \tag{2.45}$$

The expression in the square brackets is just the splitting function $P_{qg}^{(0)}(\tau)$ defined in Eq. (1.37). The integration over τ is trivial and it results in the factor $\frac{2}{3}$. Hence, we can write

$$\frac{\partial F_2(x,Q^2)}{\partial \ln Q^2} = \sum_{q=1}^{n_f} e_q^2 \frac{\bar{\alpha}_s}{9} \int^{Q^2} \frac{dk^2}{k^2} f(x,k^2). \tag{2.46}$$

Similar logarithmic derivative of the structure function F_2 can be obtained in the DLLA limit in the framework of the collinear factorization. Differentiating Eq. (1.43) and substituting $\partial q/\partial \ln Q^2$ by the corresponding DGLAP equation with neglected quarks on the right hand side gives

$$\frac{\partial F_2(x,Q^2)}{\partial \ln Q^2} = \sum_{q=1}^{n_f} e_q^2 \frac{\bar{\alpha}_s}{N_c} \int_x^1 dz P_{qg}(z) \frac{x}{z} g\left(\frac{x}{z}, Q^2\right). \tag{2.47}$$

Since at high Q^2 the function $\frac{x}{z}g(\frac{x}{z},Q^2)$ strongly decreases with the increasing $\frac{x}{z}$, the largest contribution comes from the region $z \approx 1$ and we are allowed to neglect the z dependence of the gluon density. This gives the integral of $P_{qg}(z)$ identical as in Eq. (2.45). Finally we obtain

$$\frac{\partial F_2(x,Q^2)}{\partial \ln Q^2} = \sum_{q=1}^{n_f} e_q^2 \frac{\bar{\alpha}_s}{9} x g\left(x, Q^2\right). \tag{2.48}$$

The comparison of Eqs. (2.46) and (2.48) allows us to establish the relation between the integrated and the unintegrated gluon distributions valid in the DLLA limit, namely

$$x g(x,Q^2) = \int^{Q^2} \frac{dk^2}{k^2} f(x,k^2). \tag{2.49}$$

The lower limit of integration over k^2 in the above equation lies, in general, in the non-perturbative domain. Therefore, in principle, one should also possess a meaningful description of $f(x,k^2)$ in this region in order to correctly use the relation (2.49).

2.3 Unitarity and saturation

In the preceding sections we have discussed two complementary approaches to the description of the QCD dynamics. On one hand this is the DGLAP equation, which governs the evolution of parton densities with the hard transverse scale Q^2. In the DLLA limit, $Q^2 \to \infty$ and $x \to 0$, the integrated gluon density resulting from this approach behaves as

$$x g(x,Q^2) = \exp\left\{2\sqrt{\bar{\alpha}_s \ln(Q^2/Q_0^2)\ln(1/x)}\right\}. \tag{2.50}$$

On the other hand the solution of the lading order BFKL equation gives the unintegrated gluon density of the form

$$f(x,k^2) \sim (k^2)^{1/2} x^{-\lambda} \exp\left\{-A\frac{\ln^2(k^2/k_0^2)}{\ln(1/x)}\right\}, \tag{2.51}$$

where A is a positive constant. What the two above results have in common is that the growth of the gluon density with energy is never slowed down. This statement remains valid also at higher orders. However, when the gluon density becomes very high one expects the gluon merging processes to become important. The untamed growth of parton density is an unwanted feature also because it leads to the cross sections which, at large center-of-mass energy s behave like s^λ, and hence grow faster than allowed by the Froissart-Martin bound [32, 33]

$$\sigma_{\text{tot}}(s) \leq \text{ const} \cdot \ln^2 s, \tag{2.52}$$

which means that unitarity is violated. An equation which takes into account *gluon saturation* at high densities was first derived in the DLLA limit by Gribov, Levin and Ryskin (GLR equation) [34, 35]

$$\frac{\partial^2 x g(x,Q^2)}{\partial \ln(1/x) \partial \ln(Q^2/\Lambda^2)} = \bar{\alpha}_s x g(x,Q^2) - \frac{4\alpha_s^2 N_c}{3 C_F R^2} \frac{1}{Q^2} [x g(x,Q^2)]^2, \tag{2.53}$$

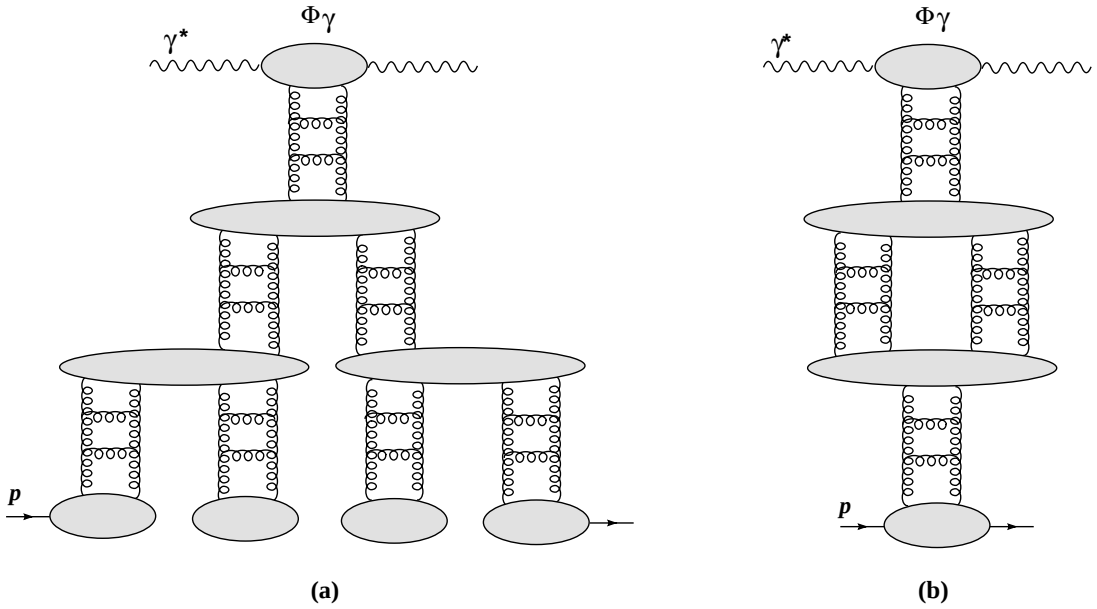

Figure 2.7: Multiple Pomeron exchange diagrams: (a) fan diagram (b) Pomeron loop diagram.

where R is the proton radius. The factor ahead the quadratic term was calculated by Mueller and Qiu [36]. The effect of slowing down the growth of the gluon density, or equivalently unitarizing the cross section is obtained by resummation of the diagrams with multiple Pomeron exchanges. As argued in [34, 35], for the case of DLLA it is sufficient to include only a subclass of all graphs, the so called *fan diagrams*, which are depicted in Fig. 2.7a whereas other types, in particular diagrams with Pomeron loops shown in Fig. 2.7b, may be neglected. The cigar shape blobs in Fig. 2.7 denote the triple Pomeron vertices.

The original idea of Gribov, Levin and Ryskin triggered an enormous activity both on the theory and phenomenology side. On one hand it resulted in a number of equations which unitarize the BFKL growth and incorporate parton saturation. In particular, Balitsky obtained in [37] an infinite hierarchy of coupled equations for n-point Wilson line operators, valid at low x. An equation identical in the large N_c limit to the first equation of the Balitsky hierarchy was independently derived by Kovchegov [38]. Thus, it is usually referred to as the Balitsky-Kovchegov (BK) equation. We will discuss its properties in detail in the Chapter 4. The BK equation is a mean field approximation of the QCD evolution. In contrast, the Balitsky hierarchy describes also fluctuations of the color field. Later on, the equation equivalent the Balitsky hierarchy, known as the JIMWLK equation was derived [39–44]. It can be used to calculate the scattering amplitudes in the framework of the color glass condensate [45, 46].

On the other hand various phenomenological models were formulated which managed to account for a wide range of the DIS data. Among them, the color dipole model of Golec-Biernat and Wüsthoff (GBW) [47, 48] and its further improvement by Bartels, Golec-Biernat and Kowalski (BGK model) [49] turned out to be particularly successful. The study performed in the framework of these two models is the subject of the next chapter.

Chapter 3

Heavy flavor production in DIS in the saturation model

As shown in the original papers of Golec-Biernat and Wüsthoff [47,48], the GBW saturation model [47] was not only able to describe both the low x structure function F_2 and the diffractive structure function F_2^D measured at HERA, but also it incorporated all the essential elements of saturation in a relatively simple way. With the advent of the more precise data [50–52] this model needed, however, an improvement in order to provide better description of F_2 at large values of the photon virtuality ($Q^2 \gtrsim 20\ \mathrm{GeV}^2$). This was attained by Bartels, Golec-Biernat and Kowalski (BGK model) [49] by incorporating into the saturation model [47] a proper gluon density evolving according to the DGLAP equation.

Since the time of the first successful attempt of Golec-Biernat and Wüsthoff other descriptions of DIS, based on the saturation physics, have appeared. These include the Regge-like model of Forshaw and Shaw [53–55] the model of Iancu, Itakura and Munier [56] which tries to reconcile the BFKL description with the theory of the color glass condensate as well as the model of McDermott, Frankfurt, Guzey and Strikman [57]. Also the BGK model extended by incorporating the impact parameter dependence has been analyzed by Kowalski, Motyka and Watt [58]. For more details on these models see *e.g.* the review given in [59].

Nevertheless, an important element was missing in the analyzes based on the BGK model as well as most of other approaches (except [58]), namely, the heavy quark contribution to the structure function F_2. The recent data from HERA [60–62] shows that this contribution cannot be neglected by any means since it reaches up to 30%.

The main goal of the study presented in this chapter is to take into account heavy quark production in the DGLAP improved saturation model and confront it with the recent data. This analysis does not introduce new parameters to those already present. Once the parameters of the dipole cross section are determined from a fit to the total structure function F_2, they can be used to *predict* the charm and beauty contributions $F_2^{c\bar{c}}$ and $F_2^{b\bar{b}}$. In addition, the longitudinal structure function F_L and the diffractive structure function F_2^D can also be predicted.

We start from introducing the color dipole formalism in Section 3.1. Subsequently, we explain the main features and recall the known results concerning the GBW and BGK models, respectively, in Sections 3.2 and 3.3. In Sections 3.4 and 3.5 we describe the fits of the GBW and BGK models with heavy quarks. The issues of critical line and geometric scaling are discussed in Section 3.6. Predictions for the charm and beauty as well as the longitudinal structure function are presented in Section 3.7. Finally the conclusions are given in Section 3.8.

The results presented in Sections 3.4-3.7 are based on the original publication [63].

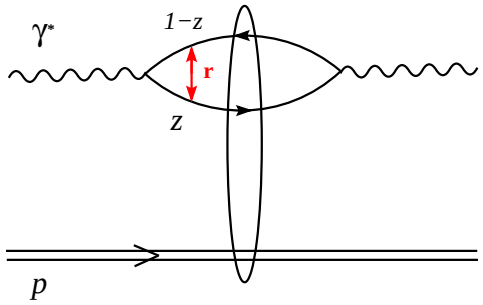

Figure 3.1: The $\gamma^* p$ interaction in the dipole formalism at small x.

3.1 Color dipole formalism

The $k_\perp$ factorization formula (2.16) may be rewritten in various ways. The form which is particularly suitable for discussion of saturation phenomena is the so called *dipole representation* in which the $\gamma^* p$ cross section is given by

$$\sigma_{T,L}(x,Q^2) = \int d^{\,2}\mathbf{r} \int_0^1 dz \sum_f |\Psi^f_{T,L}\,(\mathbf{r},z,Q^2)|^2\,\hat{\sigma}\,(x,\mathbf{r}), \tag{3.1}$$

The above formula can be obtained directly from Eq. (2.16) and the impact factors (2.10) and (2.11) after using the following relations

$$\int d^2\mathbf{l}\left\{\frac{\mathbf{l}}{D(\mathbf{l})} - \frac{\mathbf{l}+\mathbf{k}}{D(\mathbf{l}+\mathbf{k})}\right\}^2 = \bar{Q}^2 \int d^2\mathbf{r}\, K_1^2(\bar{Q}r)\left(1-e^{-i\,\mathbf{r}\cdot\mathbf{k}}\right)\left(1-e^{i\,\mathbf{r}\cdot\mathbf{k}}\right), \tag{3.2}$$

$$\int d^2\mathbf{l}\left\{\frac{1}{D(\mathbf{l})} - \frac{1}{D(\mathbf{l}+\mathbf{k})}\right\}^2 = \int d^2\mathbf{r}\, K_0^2(\bar{Q}r)\left(1-e^{-i\,\mathbf{r}\cdot\mathbf{k}}\right)\left(1-e^{i\,\mathbf{r}\cdot\mathbf{k}}\right), \tag{3.3}$$

where the notational shorthands from Eqs. (2.12) and (2.13) were used. The physical interpretation of Eq. (3.1) is the most transparent in the *proton rest frame*, where the process may be diagrammatically represented as in Fig. 3.1. The quantity $\Psi^f_{T,L}$, called the *photon wave function*, describes the splitting of the photon with the virtuality $-Q^2$ into the *color dipole*, that is a $q\bar{q}$ pair separated by $\mathbf{r}$ in the transverse plane. Quark and anti-quark carry the fraction z or $1-z$ of the light cone momentum of γ^*, respectively. For the case of the transversely and longitudinally polarized photon $|\Psi^f_{T,L}|^2$ takes the form

$$|\Psi^f_T\,(\mathbf{r},z,Q^2)|^2 \;=\; \frac{3\,\alpha_{\rm em}}{2\,\pi^2}\,e_f^2\left\{\,[\,z^2+(1-z)^2\,]\,\bar{Q}^2\,K_1^2\,(\bar{Q}\,r)\;+\;m_f^2\,K_0^2\,(\bar{Q}\,r)\,\right\}, \tag{3.4}$$

$$|\Psi^f_L\,(\mathbf{r},z,Q^2)|^2 \;=\; \frac{3\,\alpha_{\rm em}}{2\,\pi^2}\,e_f^2\left\{\,4\,Q^2\,z^2\,(1-z)^2\,K_0^2\,(\bar{Q}\,r)\,\right\}, \tag{3.5}$$

where we denoted $r \equiv |\mathbf{r}|$. Since the formation time of the $q\bar{q}$ pair is inversely proportional to x in the small x limit, it is much larger than the interaction time. Consequently, the values of $\mathbf{r}$ and z which characterize the color dipole may be regarded as being frozen during the interaction. Therefore, one can view the $\gamma^* p$ interaction at small x as a two-stages process where after the splitting of virtual photon the $q\bar{q}$ pair scatters on the proton with the *dipole cross section* $\hat{\sigma}(x,\mathbf{r})$, which has the following relation to the unintegrated gluon distribution

$$\hat{\sigma}(x,\mathbf{r}) = \frac{2\pi}{3}\int \frac{d^2\mathbf{k}}{k^4}\alpha_s f(x,k^2)\left(1-e^{-i\mathbf{k}\mathbf{r}}\right)\left(1-e^{i\mathbf{k}\mathbf{r}}\right). \tag{3.6}$$

From Eq. (3.6) one sees that in the limit $r \to 0$ the dipole cross section vanishes. This feature, called the *color transparency*, is in accord with our expectations that in perturbative QCD, due to gauge invariance, the interaction should die out as the object becomes colorless.

It is clear from Eq. (3.6) that the dipole cross section contains information about the gluonic content of the proton. The dipole-proton interaction may involve single ladder exchange and, in such case, would correspond to the BFKL result for the unintegrated gluon distribution. However, since the integration in (3.1) includes also large distances r, the dipole cross section should be valid as well in this, non-perturbative region. Therefore, some modeling for the interactions of the large dipoles is needed.

3.2 Golec-Biernat and Wüsthoff saturation model

In the GBW model the dipole cross section is given by [47]

$$\hat{\sigma}(x,r) = \sigma_0 \left\{ 1 - \exp\left(-\frac{r^2}{4R_0^2(x)} \right) \right\}, \tag{3.7}$$

where $R_0(x)$, called the *saturation radius*, was proposed in the following form

$$R_0(x) = \frac{1}{Q_0} \left(\frac{x}{x_0} \right)^{\lambda/2}. \tag{3.8}$$

One defines also the *saturation scale* as the inverse of the saturation radius

$$Q_s(x) = \frac{1}{R_0(x)} = Q_0 \left(\frac{x}{x_0} \right)^{-\lambda/2}. \tag{3.9}$$

The above choice of the form of $\hat{\sigma}(x,r)$ and $R_0(x)$ was motivated by the following arguments

- for small values of r the dipole cross section behaves like $\hat{\sigma} \sim r^2$, hence it admits the color transparency in accordance with the perturbative QCD predictions,
- for large values of r the dipole cross section saturates reaching σ_0 and that, in turn, results in $\sigma^{\gamma^* p} \sim \ln(1/x)$ which is consistent with the Froissart-Martin unitarity bound (2.52),
- for large Q^2 and small x the leading behavior of the proton structure function is $F_2 \sim x^{-\lambda}$, with λ to be fitted, which on one hand agrees with what is observed in the DIS data and on the other hand reproduces the BFKL result.

Hence, in the GBW model the BFKL-like one ladder exchanges dominate for small dipoles, $r < R_0$, whereas for $r > R_0$ the multiple Pomeron interactions and non-perturbative effects become important. This is in qualitative agreement with the GLR result mentioned in Section 2.3 and also, as we will seen in the next chapter, with the BK equation.

In the original analysis [47] the Q_0 parameter was taken as $Q_0 = 1$ GeV. The remaining parameters, σ_0, λ and x_0, were fitted to the low x DIS data from H1 and ZEUS collaborations. The values from [47] are given in the first row of Table 3.1. In this fit only three light quarks were considered with a common mass $m_q = 140$ MeV, which was adopted in order to allow for the calculation of the photoproduction cross section in the limit $Q^2 \to 0$. By "ndf" we denote the number of experimental points used in the fit. Also, the fit with the charm quark, $m_c = 1.5$ MeV, was discussed in [47]. We quote the original values of the parameters for this case in the second row of Table 3.1.

The dipole cross section from the light quark fit is shown in Fig. 3.2 as a function of the dipole size for the values of x changing from 10^{-2} down to 10^{-6}. We see that there are two possibilities

	σ_0 [mb]	λ	x_0	χ^2/ndf
light	23.03	0.288	$3.04{\cdot}10^{-4}$	1.18
light + c	29.12	0.277	$0.41{\cdot}10^{-4}$	1.50

Table 3.1: Parameters from the original fit of Golec-Biernat and Wüsthoff [47].

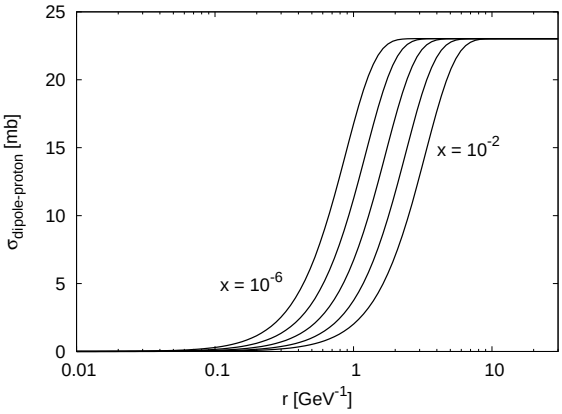

Figure 3.2: Dipole cross section in the GBW model with parameters from the first row of Table 3.1.

to saturate the cross section: either by increasing the dipole size or by decreasing x. By going with $x \to 0$ we increase the range of the dipole sizes for which the saturation behavior is important in the $\gamma^* p$ cross section (3.1). The scaling property of the dipole cross section, with the variable $r^2 Q_s(x)$, is also reflected in Fig.3.2.

3.2.1 Critical line

The saturation radius R_0 has an interpretation of the mean transverse distance between partons in the proton. On the other hand the photon with virtuality Q^2 can only resolve those objects whose transverse size is greater than $1/Q$, which is a typical dipole size. When $R_0(x) \gg 1/Q$ proton appears to the color dipole as a dilute system of partons. In contrast if $R_0(x) \ll 1/Q$ the proton seen by the $q\bar{q}$ pair becomes dense. The form of the dipole cross section (3.7) suggests the definition of the critical line that separates these two regions of the (x, Q^2) space. In the GBW model this line is specified by the condition that the argument of the exponent in $\hat{\sigma}(x, \bar{r})$ equals 1, where $\bar{r} = 2/Q$ was adopted as the magnitude of the characteristic dipole size. Hence, we obtain

$$Q^2 \, R_0^2(x) = 1. \tag{3.10}$$

This definition is not unique but it gives a meaningful estimate of the transition zone and is useful to make comparisons between various models.

(3.11)

3.2.2 Geometric scaling

In the GBW model the dipole cross section depends only on the ratio $r/R_0(x)$. If we neglect quark masses and change the variable $r \to r' = r/R_0(x)$ in Eq. (3.1), we notice that the $\gamma^* p$ cross section becomes a function of a single, dimensionless variable $\tau = Q^2 R_0^2(x)$

$$\sigma^{\gamma^* p}(x, Q^2) = \sigma^{\gamma^* p}(\tau). \tag{3.12}$$

This feature known as the *geometric scaling* is a very powerful prediction of the model since it suggests existence of a fundamental, intrinsic scale related to the phenomenon of saturation. Staństo, Golec-Biernat and Kwieciński have shown in [64] that the low x DIS data supports the prediction (3.12) of the GBW model. As we see in Fig. 3.3, this regularity holds at low x for a wide range of Q^2. As also reflected in Fig. 3.3, the geometric scaling is to some extent violated. One of the contributions to the violation of scaling comes from finiteness of the quark masses. The original idea of [64] has been recently checked against the new F_2 data and extended to the diffractive processes where the geometric scaling is also observed [65].

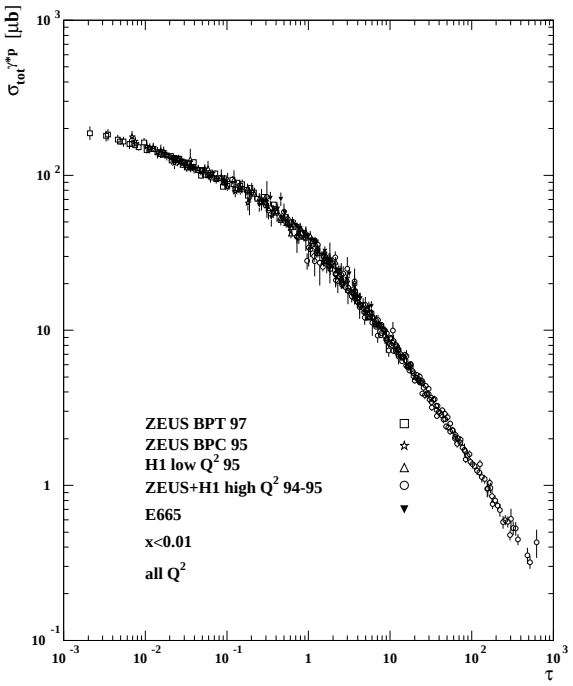

Figure 3.3: Geometric scaling of low x DIS data as a function of $\tau = Q^2 R_0^2(x)$ (reproduced from [64]).

3.2.3 Integrated gluon distribution

We conclude the discussion of the saturation model by presenting the integrated gluon distribution. One can show that taking the dipole cross section (3.7) and keeping only the leading term in Q^2 gives

$$\frac{\partial F_2(x,Q^2)}{\partial \ln Q^2} \simeq \frac{1}{4\pi^3} \sum_f e_f^2 \frac{\sigma_0}{R_0^2(x)}. \tag{3.13}$$

Comparing this result with Eq. (2.48) allows to determine the gluon distribution

$$xg(x,Q^2) = \frac{3}{4\pi^2 \alpha_s(Q^2)} \frac{\sigma_0}{R_0^2(x)}, \tag{3.14}$$

which is valid in the DLLA limit. Although the Q^2 dependence appears in Eq. (3.14) through the coupling constant it is rather far from the prediction of the DGLAP equation given in (1.51). This element turns out to be important when one tries to fit the model to the more recent data set than the one used in the original Golec-Biernat and Wüsthoff analysis [47].

3.3 DGLAP improved saturation model

To account for the proper behavior of the gluon density as a function of Q^2, the refined dipole cross section was proposed by Bartels, Golec-Biernat and Kowalski in [49] (BGK model or DGLAP improved saturation model)

$$\hat{\sigma}(x,r) \,=\, \sigma_0 \left\{1 \,-\, \exp\left(-\frac{\pi^2\, r^2\, \alpha_s(\mu^2)\, xg(x,\mu^2)}{3\,\sigma_0}\right)\right\}\,, \tag{3.15}$$

where $xg(x,\mu^2)$ is the integrated gluon density calculated at the scale

$$\mu^2 = \frac{C}{r^2} + \mu_0^2. \tag{3.16}$$

It is evolved with the leading order DGLAP equation with running coupling simplified by neglecting quarks since the model is designed for the low x region. The starting distribution at $Q_0^2 = 1$ GeV^2 was taken, similarly to the MRST analysis [66], in the form

$$xg(x,Q_0^2) \,=\, A_g\, x^{\lambda_g}\, (1-x)^{5.6}\,. \tag{3.17}$$

We observe that

- for small values of r the cross section reduces to

$$\hat{\sigma}(x,r) \,\simeq\, \frac{\pi^2}{3}\, r^2\, \alpha_s(\mu^2)\, xg(x,\mu^2), \tag{3.18}$$

  which is the known perturbative QCD result [67] admitting the color transparency property,

- for large values of r the gluon density and the coupling become frozen at the scale μ_0^2 and the dipole cross section saturates at σ_0 recovering the behavior of the GBW model.

On the whole, the BGK model has five parameters to be fitted: the dipole cross section bound σ_0 and the four parameters of the gluon distribution: A_g, λ_g, C and μ_0^2.

Introducing the realistic gluon distribution in place of (3.14) has a sizable effect on F_2, especially in the region of large Q^2. This is because when Q^2 is large the typical dipole size $\sim 1/Q$ becomes small and consequently the scale $\mu^2 \approx Q^2$ is big hence the gluon density grows. In contrast, for low Q^2 the large dipoles dominate and the scale of the gluon is close to μ_0^2. In addition, since the gluon density is now r-dependent the power governing the low x rise of the structure function becomes a function of Q^2 so that we have $F_2 \sim x^{-\lambda(Q^2)}$.

In the original paper [49] the two fits to the data H1 [50] and ZEUS [51, 52] data with $x < 0.01$ were performed. Both of them take into account only three light quarks. We recall the results of [49] in Table 3.2 below.

		σ_0 [mb]	A_g	λ_g	C	μ_0^2	χ^2/ndf
Fit 1	($m_q = 140$ MeV)	23.0	1.20	-0.28	0.26	0.52	1.17
Fit 2	($m_q = 0$ MeV)	23.8	13.71	0.41	11.10	1.00	0.97

Table 3.2: Parameters from the light quark fits of the BGK model. Notice the different sign convention of λ_g used in Eq. (3.17) and the original analysis [49].

In the first fit (Fit 1) the light quark mass was taken at the value known from the GBW model, $m_q = 140$ MeV, while in the second (Fit 2) m_q was set to zero. In addition, the parameter σ_0 was not

fitted in the first case but fixed at the value 23.0 mb. In the second case so was done with μ_0^2 which was set to 1.0.

As we see from the values of χ^2/ndf given in the last column of Table 3.2, the DGLAP improved saturation model (BGK model) successfully describes the data. There is, however, one element missing in the analysis [49], namely the heavy quarks: charm and beauty. The study which we are going to described in the remaining part of this chapter was meant to fill up this deficiency.

3.4 GBW model fitted to the new HERA data

Before studying the improved version of the saturation model (BGK model) it is interesting to check how the original model of Golec-Biernat and Wüsthoff fits the new data from HERA [50–52]. We start from considering the data points with $x \leq 0.01$ and $Q^2 \geq 0.04\,\mathrm{GeV}^2$. The number of experimental points in such a case equals 288. We added in quadrature the statistical and systematic errors in calculating χ^2. Moreover, the H1 data were multiplied by the factor 1.05 to account for slightly different normalization of the H1 and ZEUS data sets. The results of the fits with and without heavy quarks are presented in Table 3.3. The obtained values of χ^2/ndf indicate that description of the new

	σ_0 [mb]	λ	x_0	χ^2/ndf
light	16.82	0.315	$1.27{\cdot}10^{-3}$	1.96
light + c + b	18.81	0.320	$2.91{\cdot}10^{-4}$	2.24

Table 3.3: The parameters of the GBW model fitted to the new data set from HERA for all Q^2.

HERA data by the GBW model is rather poor. This has already been pointed out in [49] and should be attributed to the lack of the proper DGLAP evolution of the gluon distribution in the GBW model, *cf.* Eq. (3.14). Since the DGLAP evolution is important mostly for high photon virtualities Q^2, one would expect that restricting the Q^2 range of the fitted data from above should improve χ^2. In Table 3.4 we show the results of such fits. As we see, indeed, the GBW model describes fairly well the F_2 data with $Q^2 < 20 - 30$ GeV^2.

	σ_0 [mb]	λ	x_0	χ^2/ndf
light + c + b ($Q^2 < 50$ GeV^2)	19.26	0.301	$2.50{\cdot}10^{-4}$	1.27
light + c + b ($Q^2 < 30$ GeV^2)	19.52	0.290	$2.29{\cdot}10^{-4}$	1.04
light + c + b ($Q^2 < 20$ GeV^2)	19.73	0.284	$2.12{\cdot}10^{-4}$	0.94

Table 3.4: The parameters of the GBW model fitted to the new data set from HERA for three different upper limits on Q^2.

3.5 DGLAP improved saturation model with heavy quarks

Let us now turn to the BGK model. Similarly to the GBW case described in the previous section, we performed fits with the charm and beauty contributions in the sum in Eq. (3.1) using the recent data on the proton structure function F_2 from H1 [50] and ZEUS [51, 52]. We considered range $x \leq 0.01$ and $Q^2 \geq 0.04\,\mathrm{GeV}^2$, which gave 288 data points used in the fit. The statistical and systematic errors were added in quadrature and the H1 data were multiplied by the factor 1.05.

	σ_0 [mb]	A_g	λ_g	C	μ_0^2	χ^2/ndf
light + c + b	22.7	1.23	- 0.080	0.35	1.60	1.16
light + c	22.4	1.35	- 0.079	0.38	1.73	1.06

Table 3.5: The parameters from the fit of the BGK model with heavy quarks.

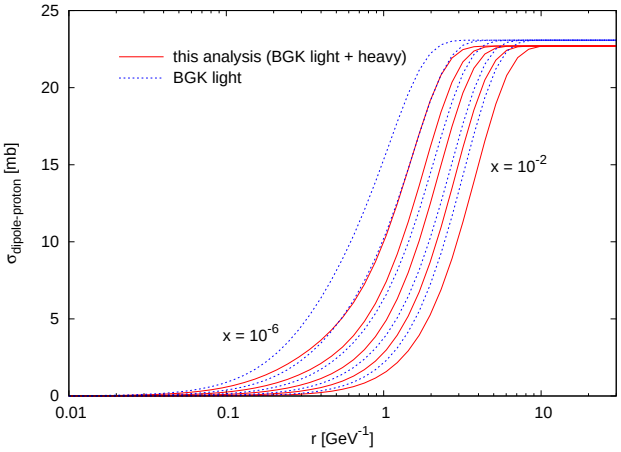

Figure 3.4: The dipole cross section in the BGK model with and without heavy quarks (solid and dashed lines, respectively) for $x = 10^{-2} \ldots 10^{-6}$.

To calculate gluon densities at the scales above Q_0^2 we used the leading order result (1.50) derived in Section 1.5.2 with the running coupling and the full splitting function (*i.e.* containing both regular and singular terms). After transforming the initial condition (3.17) into the Mellin space we obtain the explicitly real formula for the gluon density

$$xg(x,t) = \frac{A_g}{\pi}\, e^{n_0 \ln(1/x)} \Gamma(4.6) \int_0^\infty dy\, \mathrm{Re}\left\{ \frac{\Gamma(\lambda_g + n_0 + iy)\Gamma(4.6)}{\Gamma(\lambda_g + 4.6 + n_0 + iy)}\ \exp\left(iy \ln(1/x) + \tilde{\gamma}^{(0)}_{n_0+iy}\, t \right) \right\}, \tag{3.19}$$

where t was specified in Eq. (1.46). The parameters A_g and λ_g as well as the constant $4.6 = 5.6 - 1$ come from the definition of the initial condition (3.17). The inverse Mellin transform introduces, in tun, the real number n_0 that lies to the right of all singularities of the integrand in Eq. (3.19).

Similarly to the analysis [47, 49], we also modified the argument in the dipole cross section $\hat{\sigma}(x,r)$ in the heavy flavor contributions,

$$x \;\to\; x\left(1 + \frac{4m_f^2}{Q^2}\right) \;=\; \frac{Q^2 + 4m_f^2}{Q^2 + W^2}, \tag{3.20}$$

where W is the energy in the center of mass system of $\gamma^* p$. This is because for $Q^2 \ll m_{c,b}^2$ it is more appropriate to use the heavy quark mass as a hard scale.

In our fit, we set the light quark mass to zero and took typical values of the heavy quark masses, $m_\mathrm{c} = 1.3$ GeV and $m_\mathrm{b} = 5.0$ GeV. By taking light quarks to be massless we excluded the photoproduction point $Q^2 = 0$ from our considerations since in the dipole models $\sigma^{\gamma p}$ depends logarithmically on the quark mass in the limit $Q^2 \to 0$. However, for the case of the heavy quarks, when the quark mass provides the hard scale, the predictions for $Q^2 = 0$ can be made.

We performed two fits with the dipole cross section (3.15), taking into account the charm and beauty contribution in addition to the three light quarks. In the first fit only charm was considered

while in the second one both heavy flavors were present. We set the number of active flavors in α_s to 4 and 5, respectively and the value of $\Lambda = 300\ \mathrm{MeV}$ in both cases. The fit results for the five parameters of the model, σ_0, A, λ_g, C and μ_0^2, are presented in Table 3.5. As we see, the value of χ^2/ndf is still good for the fits with heavy flavors. Comparing to the result of Fit 2 from Table 3.2, we notice that the gluon parameters differ significantly from the light quark fit. In particular, the power λ_g is negative which means that the initial gluon distribution (3.17) grows with decreasing x, in contrast to the fit with light quarks only when the gluon distribution is valence–like (λ_g is positive). We have checked that with the found gluon density, the total proton momentum fraction carried by gluons is around 25% at the inital scale $Q_0^2 = 1\ \mathrm{GeV}^2$.

In Fig. 3.4 we show the comparison of the dipole cross sections from the present analysis with heavy quarks (solid lines) and the BGK analysis [49] (Fit 1) with light quarks only (dashed lines). The effect of heavy quarks is seen in the shift of the dipole cross section towards larger values of r, which means that for a given dipole size saturation occurs at lower x (higher energy). Similar effect was observed also in the GBW analysis [47].

Alternatively, when one compares our result with the cross section obtained from the massless Fit 2 from Table 3.2 one observes that the presence of heavy quarks in the DGLAP improved model cures the pathological behavior of the dipole cross section found in [49] for the case of massless fit.

3.6 Critical line and saturation scale

The shift of the dipole cross section towards larger values of r has direct impact on the position of the critical line which in the case of the BGK model, in analogy to the GBW definition form Section 3.2.1, is given by the following implicit relation between x and Q^2

$$\frac{4\pi^2}{3\sigma_0 Q^2}\,\alpha_s(\mu^2)\,xg(x,\mu^2) = 1\,, \tag{3.21}$$

with the scale $\mu^2 = CQ^2/4 + \mu_0^2$. This equation can be solved numerically to obtain the critical line shown in Fig. 3.5 as the solid line. The saturation effects are important to the left of this line. For the comparison, we also show the critical lines from the BGK and GBW analysis with light quarks only. We observe that the presence of heavy quarks shifts the critical line towards smaller values of Q^2. This means that for a given Q^2 we need lower x in order to stay in the domain where the saturation effects are important. In other words, heavy quarks make saturation more difficult to observe at present and also future colliders, which is indicated in Fig. 3.5 by the acceptance regions of HERA and the LHC.

It is appropriate to mention that some time after our analysis [63] appeared also the study of heavy quarks contribution within the IIM saturation model [56] was done [69]. In order to compare the critical line obtained in [69] with our result one has to take into account its slightly different definition in both cases. In the BGK model the critical line is defined in such a way that it corresponds to the value of the dipole cross section $\hat{\sigma}_0(x, 2/Q) \approx 0.63\,\sigma_0$ whereas in the IIM model we have the condition $\hat{\sigma}_0(x, 2/Q) \approx 0.7\,\sigma_0$. In Fig. 3.6 we compare the two critical lines calculated according to the definition adopted in [69]. As we see, in the region covered by the HERA data, *i.e.* the region used in the fit of F_2, the two results are very similar.

As discussed in Section 3.2, the GBW model features the *exact* scaling behavior of the dipole cross section, $\hat{\sigma}(x,r) = \hat{\sigma}(rQ_s(x))$. The BGK dipole cross section (3.15) seems to abandon these important element. Fortunately, when the heavy quarks are included in fitting the formula (3.1) the resulting value of C in the gluon scale (3.16) is small whereas $\mu_0^2 \approx 1.6\ \mathrm{GeV}^2$ is relatively large. It means that for not too small r, the dipole cross sections (3.15) effectively features the scaling at large values of r with the saturation scale proportional to the gluon distribution at the scale μ_0^2

$$Q_s^2(x) \simeq \frac{4\,\pi^2}{3\,\sigma_0}\,\alpha_s(\mu_0^2)\,xg(x,\mu_0^2)\,. \tag{3.22}$$

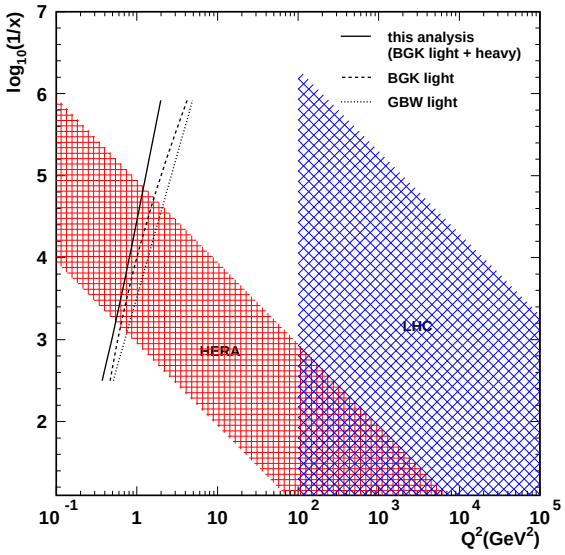

Figure 3.5: The critical line in the (x, Q^2)-plane from various saturation models indicating the position of the saturation region (to the left of these lines). The shaded areas show the acceptance regions of HERA and the LHC. The latter region corresponds to the production of an object with the minimal mass squared $Q^2 = 100\ \mathrm{GeV}^2$ [68].

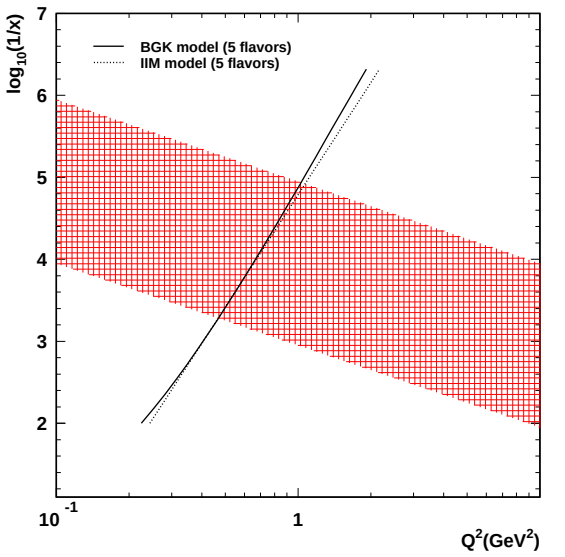

Figure 3.6: Comparison of the critical lines from two saturation models with heavy flavors, the BGK model (solid line) and the IIM model (dotted line) [69]. The definition of the critical line from [69] was used in both cases.

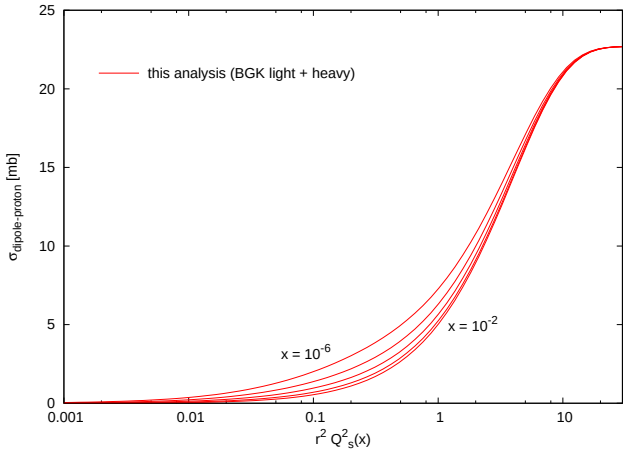

Figure 3.7: The dipole cross section in the BGK model with heavy quarks as a function of the scaling variable $r^2Q_s^2(x)$ with the saturation scale given by Eq. (3.21). Geometric scaling is preserved for moderate dipole sizes, and it is broken for small values of r due to the DGLAP modification.

Indeed, as we see in Fig. 3.7, which shows the dipole cross section as a function of the scaling variable $r^2Q_s^2(x)$, the geometric scaling is preserved for moderate values of r. It is broken, however, for small dipole sizes due to the DGLAP evolution of the gluon in the dipole cross section.

3.7 Predictions for inclusive structure functions

The parameters of the dipole cross sections (3.15) have been determined from the fit to the F_2 data. However, using Eq. (3.1) we can decompose F_2 into the sum of light and heavy quark contributions

$$F_2 = F_2^{\text{light}} + F_2^{c\bar{c}} + F_2^{b\bar{b}}\,. \tag{3.23}$$

Hence, taking the parameters from Table 3.5, which are now fixed, allows us to *predict* charm and beauty contributions separately. The dependence of the structure function on the flavor comes through the the photon wave function $\psi_{T,L}^f$, which is the function of electric charge e_f and quark mass m_f. In addition, the modification of the Bjorken variable (3.20) introduces an implicit dependence on m_f through x. Let us stress, however, that for the case of fits discussed here x-Bjorken is modified only in the heavy quark contributions to the structure function since we adopted $m_q = 0$ for the light quarks.

The predictions for $F_2^{c\bar{c}}$ and $F_2^{b\bar{b}}$ as functions of x for different Q^2 bins computed with the parameters from the first line of Table 3.5 are presented, as the solid lines, in Figs. 3.8 and 3.9, respectively. For the comparison, we put also the predictions of the GBW model with the parameters found in [47] (dashed lines). We see very good agreement with the data from HERA, both in the normalization and the slope in x, in contrast to the GBW results which overshoot the data at large values of Q^2. Thus, as already pointed out in this chapter, presence of the DGLAP evolution in the BGK model is essential for the correct predictions at large Q^2. In Figs. 3.10 and 3.11 we plot the same $F_2^{c\bar{c}}$ and $F_2^{b\bar{b}}$ contributions but this time as functions of Q^2. The agreement with the data manifested in Figs. 3.8–3.11 is quite remarkable given the simplicity of the framework we use. This may be an argument in favor of the $k_\perp$ factorization as a more efficient way of describing DIS at small x than the collinear factorization. It can also be considered as an evidence supporting the idea of parton saturation at HERA.

As pointed out in Section 3.5, due to the modification of the Bjorken variable and finite heavy quark mass one is also able to provide predictions for the photon-proton cross section in the photoproduction limit, $Q^2 \to 0$. We have found, for the HERA energy $W = 209$ GeV, the values $19.3\ \mu b$ and $0.7\ \mu b$,

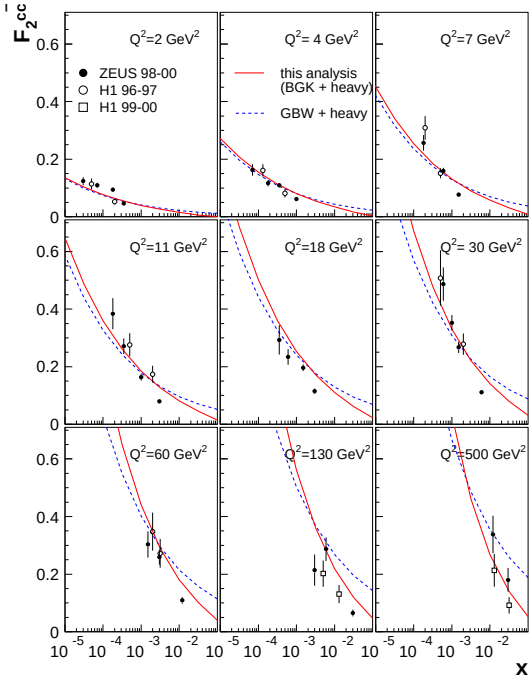

Figure 3.8: Predictions for the charm structure function $F_2^{c\bar{c}}$ in bins of Q^2 in the BGK model with heavy quarks (solid lines). Predictions in the GBW model [47] are shown for reference (dashed lines).

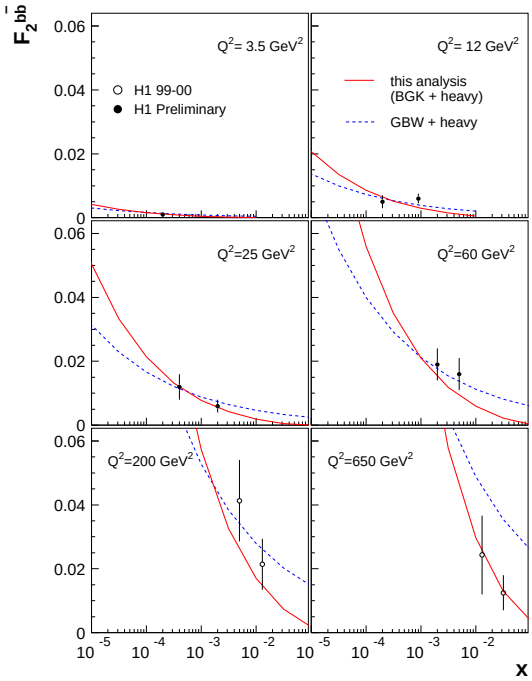

Figure 3.9: Predictions for the beauty structure function $F_2^{b\bar{b}}$ in bins of Q^2 in the BGK model with heavy quarks (solid lines). Predictions of the GBW model [47] are shown for reference (dashed lines).

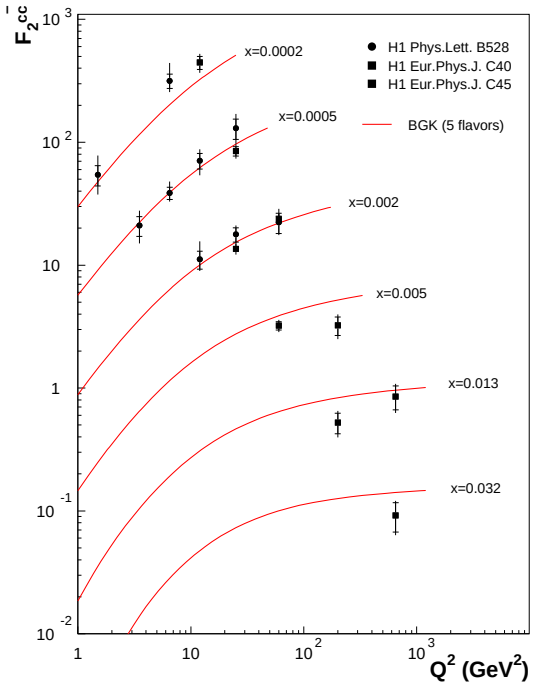

Figure 3.10: Predictions for the charm structure function $F_2^{c\bar{c}}$ in bins of Bjorken-x in the BGK model with heavy quarks (solid lines).

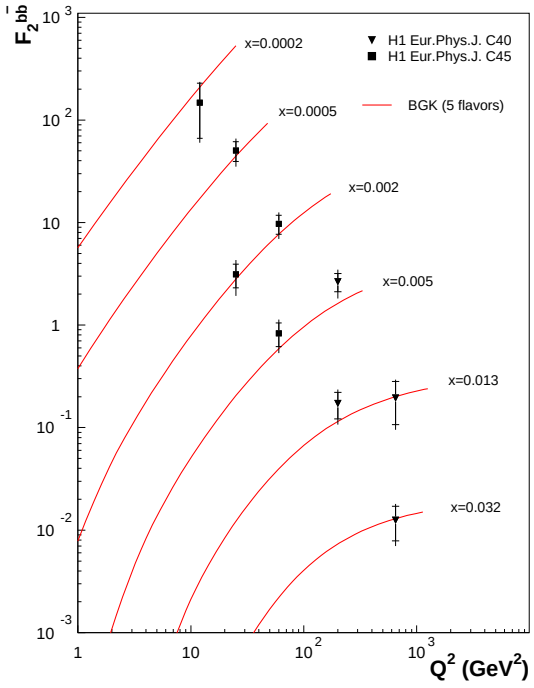

Figure 3.11: Predictions for the beauty structure function $F_2^{b\bar{b}}$ in bins of Bjorken-x in the BGK model with heavy quarks (solid lines).

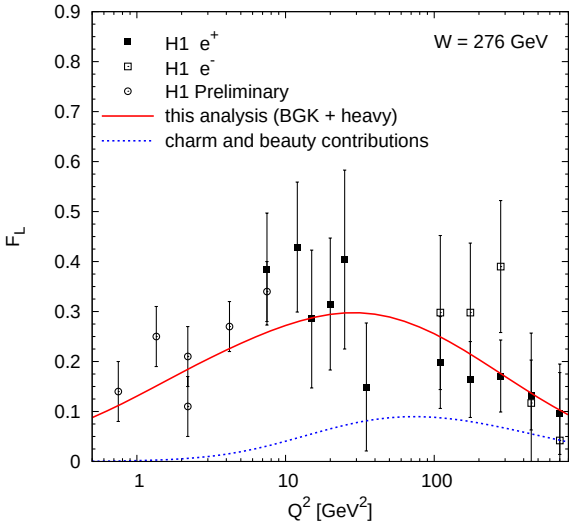

Figure 3.12: The longitudinal structure function predicted in the BGK model with heavy quarks together with the H1 estimations for various Q^2 at constant energy W = 276 GeV.

respectively. Surprisingly enough, substituting the mass $m_q = 140$ MeV for the three light quarks to the formula for $\sigma^{\gamma p}$ and performing then the photoproduction limit $Q^2 \to 0$, we found 177 μb which agrees with the measured value 174 μb up to the experimental errors.

Another interesting quantity that can be predicted using the BGK model with parameters form Table 3.5 is the longitudinal structure function F_L. In Figure 3.12 we present the longitudinal structure function from our analysis (solid line) plotted against Q^2 for $W = 276$ GeV. The experimental points represent the H1 estimations of F_L [50, 70, 71]. Reasonable agreement is observed, however, the estimation errors are too large to draw firm conclusions. Fortunately, in the last months of running of the HERA accelerator, by reduction of the pron beam energy, the center-of-mass energy of the ep system was decreased to $\sqrt{s} = 251$ GeV and $\sqrt{s} = 225$ GeV. Together with the data collected before at $\sqrt{s} = 318$ GeV, this allows for the model independent determination of F_L. Hence, one should expect much more precise data for the longitudinal structure function in the near future. In Fig. 3.12 we also show the charm and beauty contribution to F_L (dashed line). We observe that in our analysis heavy quarks are important for large values of Q^2 while for $Q^2 \lesssim 10$ GeV^2 they may safely be neglected.

3.8 Concluding remarks

In this chapter we studied the production of the charm and beauty flavors in the DGLAP improved saturation model [49]. Parameters of the model were fixed by the fit of the formula for the proton structure function F_2 to the recent data from HERA. Good quality of the fit was found with χ^2/ndf close to unity. Therefore, we conclude that the successful description of the inclusive F_2 data at low x, which was found for the BGK model with light quarks, is also preserved when the heavy flavors are considered. We observe, however, a number of differences with respect to the light quark fit from [49]. First of all, the parameters vary significantly for the models with and without heavy flavors, when one compares the fits with the massless light quarks. This results in the shift of the dipole cross section towards larger values of the dipole sizes r with respect to the light quark case. As a consequence, the critical line in the $(x,\ Q^2)$–plane moves in the direction of smaller values of Q^2 which makes saturation more difficult to observe.

The new predictions provided by our analysis concern the charm and beauty structure functions $F_2^{c\bar{c}}$ and $F_2^{b\bar{b}}$. We found a very good agreement with H1 and ZEUS data in all Q^2 bins. The significant improvement of the slope in x for high Q^2 with respect the GBW model is attributed to the DGLAP evolution.

In addition, the longitudinal structure function F_L has been predicted. We found reasonable agreement with the H1 estimations. However, large estimation errors prevent from making more precise statement. The comparison with the direct measurements, which is expected soon, will be particularly interesting.

Finally, we discussed the issues related to the essential features of parton saturation like the saturation scale and geometric scaling. We showed that the saturation scale is effectively present in the BGK model since the gluon distribution becomes frozen for small values of the factorization scale μ^2. Similarly, the property of geometric scaling of the dipole cross section, though in principle not exact, virtually persists for the moderate and large dipoles. It his however slightly violated in the regime of small dipoles.

Chapter 4

Balitsky-Kovchegov equation and the traveling waves approach

In the previous chapter we saw that the phenomenological analysis of saturation based on the idea of Golec-Biernat and Wüsthoff proves to be very successful in explaining the experimental data from HERA. The formal derivation of an equation which describes the dense gluonic system and reproduces all the essential features of the GBW model was presented afterwards, independently by Balitsky and Kovchegov (BK equation).

In this chapter we discuss the basic features of the leading order BK equation and its solutions. For this purpose, it proves to be the most convenient to work in the *color dipole framework*, developed by Mueller [72, 73], which we introduce in Section 4.1. This is an alternative description of the high energy scattering which leads, however, to the equation equivalent to the BFKL equation from Section 2.1. In Section 4.1, also the precise relation between the the standard approach, which we have used so far, and the Mueller's approach is established. The BK equation is introduced in Section 4.2, following the original paper of Kovchegov [74]. In Section 4.3 we discuss a method of analyzing the BK equation called the *traveling waves* approach, which we will exploit later on in Chapter 5. This method was introduced to QCD by Peschanski and Munier. In the series of papers [75–77] they found the relation between the leading order BK equation and the class of equations known in statistical physics which admit solutions in form of traveling waves. In terms of QCD the traveling wave solution is equivalent to the property of geometric scaling. In Section 4.4 we quote the derivation of the original results from [76] for the case of the leading order BK equation. The saturation scale and the gluon density are calculated in the limit of asymptotically small x for the equation with fixed as well as with the running coupling. The obtained results are in agreement with the expression for $Q_s^2(x)$ found earlier in [78] using a very different method.

4.1 BFKL equation from Mueller's dipole approach

As we have explained in Section 3.1, DIS at low x may be viewed as the two-stages process where at first γ^* forms a color dipole ($q\bar{q}$ pair) which in turn interacts with the hadronic target. In the framework of the Mueller dipole model the whole energy evolution takes place in the $q\bar{q}$ system rather than in the hadron target as in the standard description from Section 2.1, based on the notion of the unintegrated gluon distribution.

In Fig. 4.1a, we represent schematically the color dipole scattering off a target (a hadron or a nucleus). The quark and anti-quark coordinates in the transverse plane are denoted by ($\mathbf{x}$, $\mathbf{y}$), respectively. In the large N_c limit, the emission of the gluon from the q or $\bar{q}$ line proves to be equivalent to the splitting of the parent dipole into the two dipoles at ($\mathbf{x}$,$\mathbf{z}$) and ($\mathbf{z}$,$\mathbf{y}$). The whole procedure may

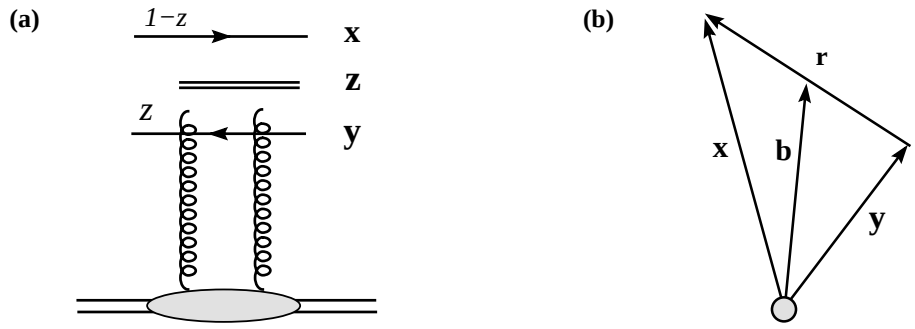

Figure 4.1: Color dipole approach: (a) In the large N_c limit, the energy evolution amounts to iterative dipole splittings and together with the single scattering of the system of dipoles leads to the BFKL equation. (b) Relation between vectors of the dipole position in the transverse plane , $\mathbf{x}$ and $\mathbf{y}$, the impact parameter, $\mathbf{b}$, and the dipole size, $\mathbf{r}$.

be iterated and one obtains the probabilistic picture of dipole splittings. This, in turn, leads to the evolution equation for the *dipole scattering amplitude*, which in the coordinate space has the form

$$\frac{\partial}{\partial \ln(1/x)}\mathcal{N}(x,\mathbf{x},\mathbf{y}) = \frac{\bar{\alpha}_s}{2\pi}\int d^2\mathbf{z}\frac{(\mathbf{x}-\mathbf{y})^2}{(\mathbf{x}-\mathbf{z})^2(\mathbf{z}-\mathbf{y})^2}\left[\mathcal{N}(x,\mathbf{x},\mathbf{z})+\mathcal{N}(x,\mathbf{z},\mathbf{y})-\mathcal{N}(x,\mathbf{x},\mathbf{y})\right]. \tag{4.1}$$

In the derivation of Eq. (4.1) it was assumed that in the single scattering only one dipole from the projectile interacts with the target.

For the purpose of our discussion, it is convenient to replace the coordinates $(\mathbf{x},\mathbf{y})$ by the dipole radius $\mathbf{r}=\mathbf{x}-\mathbf{y}$ and the impact parameter vector $\mathbf{b}=(\mathbf{x}+\mathbf{y})/2$. The corresponding relations between the vectors in the transverse plane are depicted in Fig. 4.1b. The elastic dipole scattering amplitude, $\mathcal{N}(x,\mathbf{r},\mathbf{b})$, is related to the total dipole cross section, which we have introduced in Section 3.1, by the optical theorem (see for instance [79])

$$\hat{\sigma}(x,\mathbf{r}) = 2\int d^2\mathbf{b}\,\mathcal{N}\,(x,\mathbf{r},\mathbf{b})\,. \tag{4.2}$$

The evolution equation (4.1) is equivalent to the BFKL equation written in the coordinate space. To see this, let we assume for simplicity that the amplitude depends only on the dipole size, *i.e.* $\mathcal{N}(x,\mathbf{r},\mathbf{b}) = \mathcal{N}(x,\mathbf{r})$. After applying the Fourier transform to $\mathcal{N}(x,\mathbf{r})/\mathbf{r}^2$

$$\tilde{\mathcal{N}}(x,\mathbf{k}) = \frac{1}{2\pi}\int\frac{d^2\mathbf{r}}{\mathbf{r}^2}\,e^{-i\mathbf{k}\cdot\mathbf{r}}\mathcal{N}(x,\mathbf{r}), \tag{4.3}$$

assuming in addition the azimuthal symmetry and denoting $k^2\equiv\mathbf{k}^2$, we obtain from (4.1) the following equation for the transform (4.3) of the dipole amplitude

$$\frac{\partial}{\partial\ln(1/x)}\tilde{\mathcal{N}}(x,k^2) = \bar{\alpha}_s\,\chi\left(-\frac{\partial}{\partial\ln k^2/k_0^2}\right)\tilde{\mathcal{N}}(x,k^2), \tag{4.4}$$

with χ being the Mellin transform of the BFKL kernel (Lipatov function) defined in Eq. (2.18). Finally, after using the relation between $\tilde{\mathcal{N}}(x,k^2)$ and the unintegrated gluon distribution $f(x,k^2)$ from Eq. (2.14)

$$\bar{\alpha}_s f(x,k^2) = k^4\,\nabla^2_{\mathbf{k}}\,\tilde{\mathcal{N}}(x,k^2) = 4k^2\,\partial^2_{\ln(k^2/k_0^2)}\,\tilde{\mathcal{N}}(x,k^2), \tag{4.5}$$

one arrives at the BFKL equation in the form given in Eq. (2.20).

One notices that the arguments of the leading order BFKL kernel in Eqs. (2.20) and (4.4) differ by the minus sign. This should be connected with the factor k^2 in the relation (4.5) between the unintegrated gluon distribution $f(x,k^2)$ and the function $\tilde{\mathcal{N}}(x,k^2)$. This additional power of k^2 corresponds to the shift of the Mellin variable $\gamma \to \gamma+1$. One can easily check that the Lipatov kernel (2.18) with the shifted argument gives $\chi(\gamma+1)=\chi(-\gamma)$ which explains the difference in sign.

4.2 BK evolution equation

As we have already mentioned in Section 2.3, the linear evolution equations, like DGLAP or BFKL, predict the untamed growth of the gluon density with decreasing x-Bjorken, which eventually leads to violation of unitarity. This indicates that in order to correctly describe dense gluonic systems one has to take into account not only splittings but also mergings of gluons. In terms of the Pomeron exchange, this means that also the multi Pomeron exchange diagrams should be resummed. The first equation of this sort was obtained by Gribov, Levin and Ryskin [34, 35]. The GLR equation is valid, however, only in the DLLA limit.

The non-linear equation for the dipole scattering amplitude, $\mathcal{N}$, valid at low x and for all values of Q^2, which is supposed to correctly describe the dense system of gluons, was found independently by Balitsky [37] and Kovchegov [38] (BK equation). It was derived, strictly speaking, for the case of the scattering of virtual photon on large nucleus with the atomic number A. Similarly to the GLR equation, discussed in Section 2.3, also here only the fan diagrams of Fig. 2.7a are resumed. This is because, as argued in [38, 74], other classes of multi Pomeron exchange graphs, like for instance those depicted in Fig. 2.7b, which contain Pomeron loops, are suppressed by powers of A and therefore can be neglected.

The BK equation was originally formulated in coordinate space [38], where it has the form

$$\begin{aligned}\frac{\partial}{\partial \ln(1/x)}\mathcal{N}(x,\mathbf{x},\mathbf{y}) &= \frac{\bar{\alpha}_s}{2\pi}\int d^2\mathbf{z}\frac{(\mathbf{x}-\mathbf{y})^2}{(\mathbf{x}-\mathbf{z})^2(\mathbf{z}-\mathbf{y})^2} \\ &\quad\times\left[\mathcal{N}(x,\mathbf{x},\mathbf{z})+\mathcal{N}(x,\mathbf{z},\mathbf{y})-\mathcal{N}(x,\mathbf{x},\mathbf{y})-\mathcal{N}(x,\mathbf{x},\mathbf{z})\mathcal{N}(x,\mathbf{z},\mathbf{y})\right].\end{aligned} \tag{4.6}$$

The quadratic term, which arises from the triple Pomeron vertex and enters Eq. (4.6) with a minus sign, is responsible for reducing the power-like BFKL growth of the gluon density and in this way unitarizes the cross section. In the language of the Mueller's dipole approach, here, in contrast to Eq. (4.1), also the simultaneous interaction of two or more dipoles from the projectile is present. In the region of phase space in which gluon densities are small this non-linear term may be neglected and the BK equation (4.6) reduces to the BFKL equation (4.1).

One can rewrite the BK equation (4.6) in momentum space [74]. Assuming in addition large size of the nucleus (which allows to neglect impact parameter dependence) and azimuthal symmetry the equation takes the form

$$\frac{\partial}{\partial \ln(1/x)}\tilde{\mathcal{N}}(x,k^2)=\bar{\alpha}_s\,\chi\left(-\frac{\partial}{\partial \ln k^2/k_0^2}\right)\tilde{\mathcal{N}}(x,k^2)-\bar{\alpha}_s\,\tilde{\mathcal{N}}^2(x,k^2), \tag{4.7}$$

with $\tilde{\mathcal{N}}$ defined in (4.3). The above equation in momentum space reduces to the BFKL equation (4.4) in the dilute regime and in the double logarithmic limit, after using the relation (2.49), it recovers the Gribov, Levin Ryskin result (2.53).

As demonstrated in the original paper of Kovchegov [74], Eq. (4.7) admits the solution which consists of two parts. This translates directly into the asymptotic (low x) behavior of the $F_2(x,Q^2)$ structure function. More precisely, one or the other part of the solution dominates depending on whether Q^2 is grater or smaller than some separation scale, decreasing with x, called in this context

the *saturation scale* and denoted by $Q_s^2(x)$. In the case $Q^2 > Q_s^2(x)$ the exchange of single BFKL Pomeron dominates. If we increase energy or decrease Q^2 so that $Q^2 < Q_s^2(x)$ the saturation scale starts acting like a cut-off on the transverse momenta and this way reduces the growth of F_2. Hence, the structure function predicted by the BK equation behaves at asymptotically small x like [74]

$$F_2(x,Q^2) \sim \begin{cases} x^{-(\alpha_{I\!P}-1)} & \text{for} \quad Q^2 > Q_s^2(x), \\ \ln(1/x) & \text{for} \quad Q^2 < Q_s^2(x). \end{cases} \tag{4.8}$$

We see that the emergence of the saturation scale from the BK equation and its implications of the behavior of F_2 are in agreement with the assumptions of the GBW model discussed the previous section.

Since the time the above the original result was obtained by Kovchegov, the properties of the leading order BK equation have been intensely studied using both analytic and numerical methods. One of the most important features established in many various ways [75–77] is the so called *geometric scaling*. It means that the solution of Eq. (4.7) is a function of a single variable combined from x and k, namely $k/Q_s(x)$. This, in turn, leads to the prediction of scaling for the $\gamma^* p$ cross section

$$\sigma^{\gamma^* p}(x,Q^2) = \sigma^{\gamma^* p}(Q^2/Q_s^2(x)). \tag{4.9}$$

The above property has been indeed found in the low x DIS data [64] as mentioned already in Section 3.2.2. Another interesting quality of the solution of Eq. (4.7), found in [80] and emerging from the existence of the saturation scale and geometric scaling, is the suppression of the diffusion into the infrared region known from the leading order BFKL.

Along with study of the leading order BK equation various ways to incorporate the next-to-leading logarithmic corrections where discussed. This involved in particular taking into account the running coupling effects. In the next chapter we discuss the results of our study of this type. However, formally correct extension of the Balitsky-Kovchegov equation to the next-to-leading order has been accomplished very recently. The corrections coming from the quark loop were obtained by Balitsky [81] and independently Kovchegov and Weigert [82]. These two groups arrived however at different results. Soon after, it was understood [83] that the discrepancy comes from neglecting in both cases the so called subtraction terms which were different in the two approaches. Once the subtraction terms are included, the two calculations give the same result. The gluon contribution was calculated by Balitsky and Chirilli [84]. The full NLL BK equation turns out to be much more complicated than in the leading order case and so far little is known about its solutions.

4.3 Traveling waves approach to BK

The Balitsky-Kovchegov equation (4.7) is a non-linear, partial differential equation containing the infinite order differential operator $\chi(-\partial_{\ln k^2/k_0^2})$. The exact analytic solution of this equation has not been found so far. Nevertheless, several approaches have been proposed, in which the BK equation can be solved approximately. The particularly interesting method was developed by Peschanski and Munier [75], who found the relationship between the BK equation and a class of nonlinear equations known from statistical physics. The asymptotic solutions of these equations have the form of a wave front. If certain conditions are fulfilled, the shape and the velocity of this front does not depend on the initial condition but it is determined solely by the linear part of the equation.

In what follows we introduce in detail the method of traveling waves and explain how it can be useful to study the BK equation. In addition, we present the derivation of the asymptotic solutions of the leading order BK equation in the limit of small x following the original papers [75, 76]. These solutions will be the starting point for the next chapter, where the next-to-leading logarithmic corrections to the BK equation will be studied in the framework of the traveling waves approach.

The starting point is to observe that the leading order BFKL kernel, which determines the behavior of the linear term in the BK equation (4.7), may be expanded around some value γ_c and truncated at the second order

$$\chi(-\partial_L) \simeq \chi(\gamma_c)\mathbb{1} + \chi'(\gamma_c)(-\partial_L - \gamma_c\mathbb{1}) + \frac{1}{2}\chi''(\gamma_c)(-\partial_L - \gamma_c\mathbb{1})^2, \tag{4.10}$$

where, hereafter, we adopt the notational shortcut $L = \ln(k^2/k_0^2)$, with an unspecified constant k_0^2, which only adjusts the dimension, and introduce rapidity defined as $Y = \ln(1/x)$. The constant γ_c is at this stage a parameter. Later on, we will explain how to choose its value optimally. The above approximation referred to as the *diffusive approximation* is justified when $8\bar{\alpha}_s Y \gg L$ [75]. By substituting the expansion (4.10) into Eq. (4.7) and after redefining variables so that $t = c_1 Y$ and $x = c_2 L + c_3 Y$, with c_1, c_2 and c_3 being known constants, the leading order BK equation with fixed coupling reduces to

$$\partial_t u(x,t) = \partial_x^2 u(x,t) + u(x,t) - u(x,t)^2, \tag{4.11}$$

which is the Fisher or Kolmogorov, Petrovsky and Piscounov (F-KPP) equation [85, 86]. The F-KPP equation (4.11) has been known for a long time and its properties are very well understood (see *e.g.* [87]). It belongs to a wider class of equations admitting the asymptotic solutions in the form of the traveling waves. The equation from this class satisfies the following conditions

(i) the equation is non-linear,

(ii) $u = 0$ is an *unstable* fixed point,

(iii) $u = 1$ is a *stable* fixed point.

The traveling wave solution means that $u(x,t)$ in the limit of large t has the form of the wave front $u(x,t) \sim f(x - m(t))$. The function $m(t)$ encodes information about the front velocity and can be determined by studying solely the linear limit of the F-KPP-like equation. The precise form of the solution of the F-KPP equation is given in the next section. There, we discuss also the issue of the front velocity.

The existence of traveling wave solutions is particularly appealing from the point of view of QCD since it translates directly to the property of geometric scaling of the function $\mathcal{N}(L,Y) = \mathcal{N}(L - m(Y)) \equiv \mathcal{N}(k/Q_s(x))$. (For notational simplicity, to this end, we drop the tilde and by $\mathcal{N}$ we denote the amplitude in the momentum space.) The original work of Munier and Peschanski [75] was, in fact, the first demonstration of geometric scaling for the BK equation based on the fully analytic approach.

Before we turn to the detailed description of how the traveling wave solution emerges from Eq. (4.11), let us notice that the BK equation in the diffusive approximations satisfies all the above conditions (i)-(iii). Indeed, $\mathcal{N} = 0$ and $\mathcal{N} = 1$ are the fixed point solutions and the former is moreover unstable since a small perturbation from zero results in the BFKL type growth of $\mathcal{N}$. This conclusion does not change if one considers the BK equations with running coupling or with a higher order kernel χ.

4.3.1 F-KPP equation

Let us introduce, using the example of the F-KPP equation, some basics facts about the solutions of the above mentioned class of nonlinear problems, which we will, in turn, use to study the properties of the Balitsky-Kovchegov equation. Traveling waves are formed due to presence of the non-linear damping term. However, some characteristics of the solution in the neighborhood of the front and at asymptotic

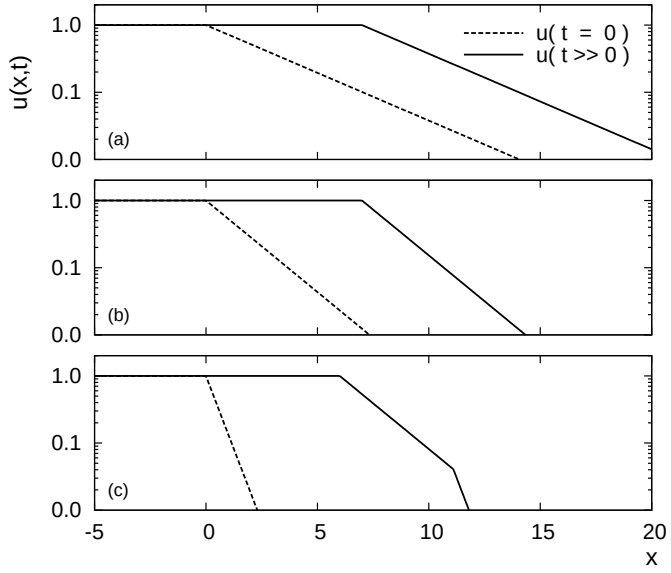

Figure 4.2: The tree possible shapes of the wave front at large time t: (a) $\gamma_0 < \gamma_c$, the results keeps the memory of the initial condition, (b) $\gamma_0 = \gamma_c$, (c) $\gamma_0 > \gamma_c$, the slope of the front is given by the universal value of γ_c apart from the narrow forward part with diminishes with time.

values of t can be determined from the linearized form of the equation. The general solution of the linear part of Eq. (4.11) is a superposition of plane waves

$$u(x,t) = \int_{\mathcal{C}} \frac{d\gamma}{2\pi i} u_0(\gamma) \exp\left(-\gamma\left(\bar{x} + \upsilon_{\text{WF}}\, t\right) + \omega(\gamma) t\right), \tag{4.12}$$

where $\omega(\gamma)$ is the Mellin transform of linear operator from the considered equation and $\mathcal{C}$ is the standard contour of the inverse Mellin transform (see Appendix A). The variable $\bar{x} = x - \upsilon_{\text{WF}}\, t$ is the position in the frame of the wave front, which moves with the velocity υ_{WF}. By the *wave front* we mean here the leading behavior of the package which can be calculated from Eq. (4.12) with aid of the saddle point method. The condition introduced by this method leads to $\upsilon_{\text{WF}} = \omega'(\gamma_c)$. Each wave (labeled by γ) from the package moves with the phase velocity

$$\upsilon_{\text{ph}}(\gamma) = \frac{\omega(\gamma)}{\gamma}, \tag{4.13}$$

and by definition the shape of the wave γ observed in the frame moving with the velocity $\upsilon_{\text{ph}}(\gamma)$ is time independent. So is the shape of the wave front observed in its own frame, which gives the second condition for the wave front velocity namely $\upsilon_{\text{WF}} = \omega(\gamma_c)/\gamma_c$. However, this is true only when the initial condition $u_0(\gamma)$ does not introduce singularity that could dominate the saddle point phase factor. Assuming for the moment that the above holds, we may compare the two conditions for υ_{WF} and obtain

$$\gamma_c\, \omega'(\gamma_c) = \omega(\gamma_c), \tag{4.14}$$

which is in fact a closed definition of γ_c. It turns out that Eq. (4.14) is identical with the condition for the minimum of the phase velocity (4.13).

As signaled above, form of the initial condition $u_0(\gamma)$ is of crucial importance since it determines which of the two possible asymptotic solutions is reached. Assuming quite general form of $u(x, t = 0)$,

namely $u(x,0) = 1$ for $x \leq 0$ and $u(x,0) = \exp(-\gamma_0 x)$ for $x > 0$, we obtain for large times

$$u(x,t) \sim \begin{cases} \exp(-\gamma_0\,\bar{x}) & \text{if} \quad \gamma_0 < \gamma_c, \\ \exp(-\gamma_c\,\bar{x}) & \text{if} \quad \gamma_0 \geq \gamma_c. \end{cases} \tag{4.15}$$

Hence, three distinct cases are possible. In the first case, $\gamma_0 < \gamma_c$, the traveling wave asymptotic solution keeps the memory of the initial condition. The wave front moves with velocity $v = \omega(\gamma_0)/\gamma_0$ and its slope at large t equals γ_0 as shown in Fig. 4.2a. In the second case, which we call critical, $\gamma_0 = \gamma_c$, the wave front velocity equals the minimal phase velocity, which we will also refer to as the *group velocity*, $v = \omega(\gamma_c)/\gamma_c = v_g$. This situation is depicted in Fig. 4.2b. In the third case, $\gamma_0 > \gamma_c$, information about the initial condition is lost at large t and the asymptotic properties of the solution, encoded in the values of γ_c and v_g, are determined solely by the form of the linear part of Eq. (4.11). The wave front velocity equals minimum of the phase velocity which is, in turn, the same as the group velocity. As shown in Fig. 4.2c, at large t the slope of the wave front equals γ_c except for the small forward part which decreases with t.

The general form of the solution of the F-KPP equation and other equations satisfying the conditions (i)-(iii), is known also beyond the asymptotic limit (4.15). As shown in [88], for the case $\gamma_0 > \gamma_c$ and large t we have

$$u(x,t) = t^{\alpha} G\left(\frac{\bar{x} + c(t)}{t^{\alpha}}\right) \exp\left(-\gamma_c(\bar{x} + c(t))\right), \tag{4.16}$$

where the time derivative of $c(t)$ is given by $\dot{c}(t) \simeq \beta t^{k-1}$. The parameters α, β and k can be determined by a matching procedure as we will show in what follows. Here, let us only comment that t^{α} gives the order of the width of this part of the front which is characterized by the slope γ_c. In turn, the function $\dot{c}(t)$ provides correction to the front velocity, v_{WF}, which is not exactly equal to the group velocity in the sub-asymptotic regime.

4.3.2 Initial condition for QCD

Let us come back to QCD. The remaining element which has to be specified before we attempt to study solutions of the BK equation by the traveling waves method is the form of the initial condition. As explained in Section 4.1, the function $\mathcal{N}(L,Y)$ is a Fourier transform of $\mathcal{N}(r,Y)/r^2$, where $\mathcal{N}(r,Y)$ is the dipole elastic scattering amplitude related, through the optical theorem, to the total dipole-proton cross section. Here, for simplicity, we assume that one can neglect the dependence on impact parameter. We have already mentioned that for small dipoles one expects from the amplitude to posses the color transparency property. In fact, we know precisely that

$$\mathcal{N}(r,Y)\Big|_{\text{small } r} \sim r^2, \tag{4.17}$$

which translates through (4.3) to the momentum space and takes the form

$$\mathcal{N}(k,Y)\Big|_{\text{large } k} \sim \frac{1}{k^2} \sim e^{-L}. \tag{4.18}$$

Hence, we can read from the above formula that for the case of QCD, $\gamma_0 = 1$. This value is to be compared with γ_c characteristic for a particular form of the BK equation under consideration.

4.4 Solution of the leading order BK equation

4.4.1 Fixed coupling case

In Section 4.3 we saw that the leading order BK equation with fixed coupling and in the diffusive approximation is equivalent to the F-KPP equation. To demonstrate this one must change variables

so that $t = c_1 Y$ and $x = c_2 L + c_3 Y$. However, since the BK equation (4.7) itself satisfies all the conditions (i)-(iii), it belongs to the desired class and, as demonstrated in [76], can be studied directly in the form (4.7).

The general solution of the linear part of the BK equation (4.7) is given by (*cf.* Eq. (4.12))

$$\mathcal{N}(L,Y) = \int \frac{d\gamma}{2\pi i} \mathcal{N}_0(\gamma) \exp\left(-\gamma\, L + \bar{\alpha}_s \chi(\gamma) Y\right), \tag{4.19}$$

where $\chi(\gamma) = \chi_0(\gamma)$ is the LL BFKL kernel (2.18). Following the general method discussed in Section 4.3.1, we identify $\omega(\gamma) = \bar{\alpha}_s \chi(\gamma)$ and write the expressions for the phase and group velocity

$$v_{\text{ph}}(\gamma) = \bar{\alpha}_s \frac{\chi(\gamma)}{\gamma}, \qquad\qquad v_g = \bar{\alpha}_s \left.\frac{d\chi(\gamma)}{d\gamma}\right|_{\gamma=\gamma_c}. \tag{4.20}$$

The critical value γ_c is determined from the saddle point condition at large Y, which in this case has has the form

$$\gamma_c\, \chi'(\gamma_c) = \chi(\gamma_c), \tag{4.21}$$

and gives the value $\gamma_c \simeq 0.6275$. We see that, since $\gamma_0 > \gamma_c$ for the case of the LL BK equation with fixed coupling, we are in the regime in which the asymptotic solution will not keep the memory of the initial condition. In the diffusive approximation Eq. (4.7) takes the form

$$\partial_Y \mathcal{N}(L,Y) = -v_g \partial_L \mathcal{N}(L,Y) + \frac{1}{2}\bar{\alpha}_s \chi''(\gamma_c)(\partial_L + \gamma_c \mathbb{1})^2 \mathcal{N}(L,Y) - \bar{\alpha}_s \mathcal{N}^2(L,Y). \tag{4.22}$$

After substituting the Ansatz (4.16), with the identification $x = L$, $t = Y$ and $u = \mathcal{N}$, into the above equation we obtain the ordinary differential equation for the function $G(z)$

$$\frac{1}{2}\bar{\alpha}_s \chi''(\gamma_c) Y^{-\alpha} \frac{d^2}{d^2 z} G(z) + (\alpha z Y^{\alpha-1} - \dot{c}(Y)) \frac{d}{dz} G(z) + Y^{\alpha-1}(\gamma_c\, \dot{c}(Y) Y - \alpha) G(z) = 0, \tag{4.23}$$

where by dot we mean the derivative with respect to Y and we have also denoted $z = Y^{-\alpha}(L - v_g Y + c(Y))$. If we want the different terms in Eq. (4.23) to contribute to the leading order in $1/Y$ we must set $\alpha = \frac{1}{2}$ and $k = 0$. Then, collecting all the terms leading in the limit of large Y, which for the case of Eq. (4.23) are proportional to $Y^{-1/2}$, we obtain

$$\bar{\alpha}_s \chi''(\gamma_c) \frac{d^2}{d^2 z} G(z) + z \frac{d}{dz} G(z) + (2\beta\gamma_c - 1) G(z) = 0. \tag{4.24}$$

In order to recover the asymptotic solution (4.15), the function $G(z)$ must behave like $G(z) \sim z$ for $z \to 0$. This fixes $\beta = 3/(2\gamma_c)$ and the solution of Eq. (4.24) is given by

$$G(z) = \text{const} \cdot \sqrt{\frac{2}{\bar{\alpha}_s \chi''(\gamma_c)}}\, z \exp\left(-\frac{z^2}{2\bar{\alpha}_s \chi''(\gamma_c)}\right). \tag{4.25}$$

Finally, the result for the gluon density, written in terms of k and Y, reads [76]

$$\mathcal{N}(k^2/Q_s^2(Y), Y) = \text{const} \cdot \sqrt{\frac{2}{\bar{\alpha}_s \chi''(\gamma_c)}} \ln\left(\frac{k^2}{Q_s^2(Y)}\right) \left(\frac{k^2}{Q_s^2(Y)}\right)^{-\gamma_c} \exp\left(-\frac{\ln^2\left(k^2/Q_s^2(Y)\right)}{2\bar{\alpha}_s \chi''(\gamma_c) Y}\right), \tag{4.26}$$

where we have defined the saturation scale

$$Q_s^2(Y) = k_0^2 \exp\left(\bar{\alpha}_s \frac{\chi(\gamma_c)}{\gamma_c} Y - \frac{3}{2\gamma_c} \ln Y\right), \tag{4.27}$$

where k_0^2 is an undetermined constant. The form of the dipole scattering amplitude (4.26) exhibits geometric scaling at asymptotic values of Y. However, in the sub-asymptotic region, this scaling is violated by the last exponential term. Also, we see that the two terms in the saturation scale (4.27), $\sim Y$ and $\sim \ln Y$, are universal, *i.e.* they depend only on the form of the BFKL kernel.

4.4.2 Running coupling case

Let us now, still following [76], consider Eq. (4.7) extended by taking $\bar{\alpha}_s$ to be running with L according to $\bar{\alpha}_s = 1/(bL)$, where $b = (11C_A - 2n_f)/(12N_c)$. Then, the Balitsky-Kovchegov equation takes the form

$$bL\partial_Y \mathcal{N}(L,Y) = \chi(-\partial_L)\,\mathcal{N}(L,Y) - \mathcal{N}^2(L,Y). \tag{4.28}$$

Here, we sketch briefly how this equation can be solved in the framework of the traveling waves approach. Detailed derivation will be given in the next section, where the more general equation is studied. As explained in [76], the solution of the linearized version of Eq. (4.28) can be expressed in terms of the double Mellin transform

$$\mathcal{N}(L,Y) = \int \frac{d\gamma}{2\pi i} \int \frac{d\omega}{2\pi i} \mathcal{N}_0(\gamma,\omega)\, \exp\left(-\gamma L + \omega Y + \frac{1}{b\omega} X(\gamma)\right), \tag{4.29}$$

with

$$X(\gamma) = \int_{\hat{\gamma}}^{\gamma} d\gamma'\, \chi(\gamma'), \tag{4.30}$$

and $\hat{\gamma}$ being an arbitrary constant. The saddle point integration over ω gives

$$\mathcal{N}(L,Y) = \int \frac{d\gamma}{2\pi i} \mathcal{N}_0(\gamma)\, \exp\left(-\gamma L + \sqrt{Y}\sqrt{\frac{4X(\gamma)}{b}}\right). \tag{4.31}$$

This result has the same "wave package structure" as the expression (4.12), which leads us to the identification of $\sqrt{Y}$ with time and $(1/\gamma)\sqrt{4X(\gamma)/b}$ with the phase velocity. By finding minimum of the latter we obtain the group velocity v_g. However, here v_g depends on the arbitrary constant $\hat{\gamma}$ introduced in Eq. (4.30). Hence, one imposes the condition $dv_g(\hat{\gamma})/d\hat{\gamma} \equiv 0$ and arrives at the value of the critical parameter $\gamma_c \simeq 0.6275$, which is identical as in the case of the LL BFKL equation with fixed coupling. Finally, we have

$$v_g = \sqrt{\frac{2\chi(\gamma_c)}{b\gamma_c}}. \tag{4.32}$$

In analogy to the fixed coupling case, after exploiting Eq. (4.16), one arrives at the differential equation for $G(z)$ in which the parameters must be set to $\alpha = \frac{1}{3}$ and $k = \frac{1}{3}$. By keeping only the leading terms in $1/Y$ this equation reduces to the Airy equation which gives

$$G(z) = \text{const} \cdot \text{Ai}\left(\xi_1 + \left(\frac{\gamma_c\, v_g\, b}{\chi''(\gamma_c)}\right)^{\frac{1}{3}} z\right), \tag{4.33}$$

where $\xi_1 = -2.338$ is the rightmost zero of the Airy function. The resulting gluon density is

$$\mathcal{N}(k^2/Q_s^2(Y), Y) = \text{const} \cdot Y^{\frac{1}{6}} \left(\frac{k^2}{Q_s^2(Y)}\right)^{-\gamma_c} \text{Ai}\left(\xi_1 + \left(\frac{\sqrt{2b\gamma_c\,\chi(\gamma_c)}}{\chi''(\gamma_c)}\right)^{\frac{1}{3}} \ln\left(\frac{k^2}{Q_s^2(Y)}\right) Y^{-\frac{1}{6}}\right), \tag{4.34}$$

and the saturation scale takes the form

$$Q_s^2(Y) = k_0^2 \exp\left(\sqrt{\frac{2\chi(\gamma_c)}{b\gamma_c}} Y + \frac{3}{4}\left(\frac{\chi''(\gamma_c)}{\sqrt{2b\gamma_c\,\chi(\gamma_c)}}\right)^{\frac{1}{3}} \xi_1\, Y^{\frac{1}{6}}\right). \tag{4.35}$$

Similarly to the fixed coupling case also the above solution admits geometric scaling property for $Y \to \infty$, which is violated in the sub-asymptotic regime. However, as we see by comparing Eqs. (4.27) and (4.35), the dependence of the saturation scale on Y differs significantly between the cases with fixed and running coupling.

Chapter 5

Balitsky-Kovchegov equation beyond the leading order

It is natural to ask whether the traveling waves method, introduced in the previous chapter, can be also applied to the BK equation with the NLL kernel and, if so, which asymptotic solutions one obtains. For the case of fixed coupling, the result has been obtained in [89]. The case of the running coupling, which has not been considered so far, is the subject of the study presented in this chapter.

The LL BK equation (4.7) in the limit of the dilute system of gluons reduces to the LL BFKL equation (4.4). Similarly, the NLL BK equation must reduce to the NLL BFKL equation. However, due to its pathologies, the NLL BFKL kernel should not be applied directly. Instead, one ought to replace it by one of the improved kernels, discussed in Section 2.1.3, which contains a class of higher order corrections. The resummed kernels acquire dependence on ω, which is the Mellin conjugate of the rapidity Y. In addition, as we will see in the next section, such kernel may depend explicitly on the coupling. Hence, the BK equation with the running coupling and the improved NLL BFKL kernel can be written as

$$bL\,\partial_Y \mathcal{N}(L,Y) = \chi(-\partial_L, \partial_Y, \bar{\alpha}_s)\,\mathcal{N}(L,Y) - \mathcal{N}^2(L,Y). \tag{5.1}$$

In what follows, the kernels resummed in three specific schemes, called S3, S4 [27] and CCS [28, 29], will be considered. These schemes are introduced briefly in Section 5.1. We stress, however, that our results can be easily applied to the case of any resummed kernel. In Section 5.2 we present the detailed calculations which lead to the asymptotic solutions of Eq. (5.1), in the limit of large Y. The issues related to the saturation scale and, in particular, its dependence on the resummation scheme are discussed in Section 5.3. There, we compare also our results with the previously known results for the CCS scheme obtained, using a very different method, in [90]. In Section 5.3 we make also an observation how, within the formalism of traveling waves, one can account for the sub-asymptotic, non-universal terms, relevant at phenomenological energies. In Section 5.4 we give the summary of our study of saturation in the deep inelastic scattering.

The results presented in Sections 5.2 and 5.3 are based on the original publication [91].

5.1 Schemes of collinear resummations of the NLL BFKL kernel

In Section 2.1.3 we pointed out the necessity to improve the NLL BFKL kernel by supplementing it with the resummed class of higher order corrections. In particular, we discussed the approach based on the study of the collinear and anti-collinear limits of the kernel in which, after imposing the renormalization group constraints, one is able to unambiguously reproduce the most divergent parts of the higher order corrections. The sub-leading and the regular terms are, however, arbitrary and they are

parametrized differently in various resummation schemes. Here, we discuss briefly three schemes introduces in [27–29]. The kernels resummed in these schemes will be used in our study of the BK equation described in the succeeding in Sections 5.2 and 5.3.

S3 scheme

In this scheme [27], considered for the symmetric choice of scale, the kernel from Eq. (2.40) is modified according to

$$\chi^{(0)}_{\rm S3}(\gamma,\omega) = (1-\bar{\alpha}_s A)\left(2\psi(1) - \psi\left(\gamma + \frac{\omega}{2} + \bar{\alpha}_s\, B\right) - \psi\left(1-\gamma + \frac{\omega}{2} + \bar{\alpha}_s\, B\right)\right). \tag{5.2}$$

The term of the order $\bar{\alpha}_s$ from $\chi^{(0)}_{\rm S3}$ is given by

$$\chi^{(0)}_{{\rm S3},\,1} = -\frac{1}{2\gamma^3} - \frac{B}{\gamma^2} - \frac{A+\frac{\pi^2}{6}}{\gamma} + \mathcal{O}(1), \tag{5.3}$$

and the constants A and B are fixed in such a way that the divergences $1/\gamma^k$ of the NLL kernel, $\chi_1(\gamma)$, from (2.36) for $k = 1, 2, 3$ are reproduced by $\chi^{(0)}_{\rm S3}$. Then, $\chi^{(0)}_{{\rm S3},\,1}$ has to be subtracted from χ_1 to avoid double counting and we obtain

$$\chi_{\rm S3}(\gamma,\omega,\bar{\alpha}_s) = \chi^{(0)}_{\rm S3}(\gamma,\omega) + \bar{\alpha}_s\left(\chi_1(\gamma) - \chi^{(0)}_{{\rm S3},\,1}\right). \tag{5.4}$$

The second term is finite since we removed all poles in $\gamma = 0$ and $\gamma = 1$. The kernel is exact up to NLL and, due to the modification (5.2) of the first term in (5.4), it is free of double logarithms after changing the scale to $W_0^2 = k_1^2$ or $W_0^2 = k_2^2$. Hence, it does justice to the renormalization group requirements.

S4 scheme

This scheme, which was also proposed in [27], is similar in spirit to the above, however, here, instead of the kernel (5.2), the following function is used

$$\chi^{(0)}_{\rm S4}(\gamma,\omega) = \chi_0(\gamma) - \frac{1}{\gamma} - \frac{1}{1-\gamma} + (1-\bar{\alpha}_s A)\left(\frac{1}{\gamma + \frac{\omega}{2} + \bar{\alpha}_s\, B} + \frac{1}{1-\gamma + \frac{\omega}{2} + \bar{\alpha}_s\, B}\right). \tag{5.5}$$

Since $\psi(\gamma) = 1/\gamma + \mathcal{O}(\gamma)$, the definitions (5.2) and (5.5) differ only by regular terms admitting the same collinear limit. The constants A and B are determined as in the S3 scheme and the full answer is given by

$$\chi_{\rm S4}(\gamma,\omega,\bar{\alpha}_s) = \chi^{(0)}_{\rm S4}(\gamma,\omega) + \bar{\alpha}_s\left(\chi_1(\gamma) - \chi^{(0)}_{{\rm S4},\,1}\right), \tag{5.6}$$

where $\chi^{(0)}_{{\rm S4},\,1}$ is calculated in analogy to $\chi^{(0)}_{{\rm S3},\,1}$. Again, all poles are removed from the second term in Eq. (5.6).

CCS scheme

Here, the resummed kernel for the symmetric scale choice has the form [28, 29]

$$\chi_{\rm CCS}(\gamma,\omega) = \chi^s_0(\gamma,\omega) + \omega\frac{\tilde{\chi}_1(\gamma,\omega)}{\chi^s_0(\gamma,\omega)}. \tag{5.7}$$

with χ_0^s defined in Eq. (2.40). One arrives at the above results after making the following steps. First, the double logarithmic terms $\mathcal{O}(\bar{\alpha}_s/\gamma^3)$ contained in the function (2.40) are subtracted from the χ_1 kernel to avoid double counting. These are

$$\frac{\chi_0(\gamma)}{2}\left(-\psi'(\gamma)-\psi'(1-\gamma)\right). \tag{5.8}$$

In contrast to the S3 and S4 schemes, the quadratic and single poles, are not eliminated from χ_1. They are instead changed in the same manner as in Eq. (2.40) for the leading order kernel χ_0. That is the $1/\gamma$ pole becomes $1/(\gamma+\omega/2)$ and the $1/(1-\gamma)$ pole is replaced by $1/(1-\gamma+\omega/2)$. This is done by subtracting the unchanged poles from χ_1 and adding the changed ones. Altogether, the we obtain

$$\begin{aligned}\tilde{\chi}_1(\gamma,\omega) &= \chi_1(\gamma)-\frac{\chi_0(\gamma)}{2}\left(-\psi'(\gamma)-\psi'(1-\gamma)\right)-A_1(0)\psi'(\gamma)+A_1(\omega)\psi'\left(\gamma+\frac{\omega}{2}\right)\\ &\quad -(A_1(0)-b)\psi'(1-\gamma)+(A_1(\omega)-b)\psi'\left(1-\gamma+\frac{\omega}{2}\right)+\frac{\pi^2}{6}\left(\chi_0^s(\gamma,\omega)-\chi_0(\gamma)\right),\end{aligned} \tag{5.9}$$

where by taking $A_1(\omega)$ in the shifted poles the resummation of running coupling and finite terms of splitting functions effects is included. Ultimately, the coupling is replaced by the ratio $\omega/\chi_0^s(\gamma,\omega)=\bar{\alpha}_s+\mathcal{O}(\bar{\alpha}_s^2)$. Hence, the NLL BFKL kernel is correctly reproduced to the order $\bar{\alpha}_s$.

5.2 BK equation with NLL BFKL kernel and running coupling

In this and the succeeding sections we study the BK equation (5.1) with the running coupling and the resumed NLL BFKL kernel $\chi(-\partial_L,\partial_Y,\bar{\alpha})$. In some schemes, like the CCS scheme, the kernel does not depend explicitly on the coupling. In those which in which the explicit dependence appears, *e.g.* S3, S4 schemes, we fix $\bar{\alpha}_s$ in the kernel at some phenomenologically motivated value. In order to simplify the notation we do not write the dependence on $\bar{\alpha}_s$ explicitly in what follows. In principle, the NLL corrections could affect also the nonlinear term from (5.1). However, as we explained in the previous chapter this will not change the traveling-wave properties since they are determined solely by the linear part of the equation.

Following the method developed in [76], applied already in Section 4.4.2 to the leading order case, we first write the solution to the linearized version of Eq. (5.1). It has the form of the double Mellin transform [28]

$$\mathcal{N}(L,Y)=\int\frac{d\gamma}{2\pi i}\int\frac{d\omega}{2\pi i}\,\mathcal{N}_0(\gamma,\omega)\,\exp\left(-\gamma L+\omega Y+\frac{1}{b\omega}X(\gamma,\omega)\right), \tag{5.10}$$

where this time the function X depends also on ω

$$X(\gamma,\omega)=\int_{\hat{\gamma}}^{\gamma}d\gamma'\,\chi(\gamma',\omega), \tag{5.11}$$

with $\hat{\gamma}$ being an unspecified constant. With such a form of X in the limit of large L, using the saddle point method, one recovers the relation

$$\omega=\bar{\alpha}_s\chi(\gamma,\omega). \tag{5.12}$$

The saddle point integration over ω, justified in the limit of large Y, results in

$$\mathcal{N}(L,Y)=\int\frac{d\gamma}{2\pi i}\,\mathcal{N}_0(\gamma)\,\exp\Big(-\gamma L+F(\omega_s)\,Y\Big), \tag{5.13}$$

where we introduced

$$F(\omega_s) = \frac{1}{Yb\,\omega_s}\left(2X(\gamma,\omega_s) - \omega_s \dot{X}(\gamma,\omega_s)\right), \tag{5.14}$$

and the condition for the saddle point ω_s is given by the implicit equation

$$Yb\omega_s^2 - X(\gamma,\omega_s) + \omega_s \dot{X}(\gamma,\omega_s) = 0. \tag{5.15}$$

The last term arises due to the dependence of the resummed NLL kernel on ω. We adopted the notation in which the prime means the derivative with respect to γ whereas the dot means the derivative with respect to ω. Now we face the problem of extracting the leading behavior of ω_s from the implicit relation (5.15). If we expand $X(\gamma,\omega)$ near $\omega = 0$

$$X\left(\gamma,\omega\right) = \sum_{p=0}^{\infty} \frac{X^{(p)}(\gamma,0)}{p!}\,\omega^p, \tag{5.16}$$

and similarly expand the derivative $\dot{X}$, after substituting both quantities into Eq. (5.15) we obtain

$$\left[Yb + \frac{1}{2}\ddot{X}\left(\gamma,0\right)\right]\omega_s^2 = X\left(\gamma,0\right) - \left\{\sum_{p=3}^{\infty} \frac{1}{p(p-2)!} X^{(p)}\left(\gamma,0\right)\omega_s^p\right\}. \tag{5.17}$$

The leading behavior for asymptotic Y, is $\omega_s \sim Y^{-1/2}$. It is easy check that, the subleading corrections, are of the order of $Y^{-3/2}$. Hence, as we will show later on, they may contribute only to non-universal sub-asymptotic terms.

5.2.1 Traveling wave critical parameters

Since we are interested in the NLL corrections to the first two universal terms from the saturation scale it suffices to truncate Eq. (5.17) at the second order in ω_s. This gives

$$\omega_s = \sqrt{\frac{X\left(\gamma,0\right)}{Yb + \frac{1}{2}\ddot{X}(\gamma,0)}}, \tag{5.18}$$

which we use as an argument of the function defined in Eq. (5.14). Hence, the formula (5.13) for the gluon density takes the familiar form

$$\mathcal{N}(L,Y) = \int \frac{d\gamma}{2\pi i}\mathcal{N}_0(\gamma)\exp(-\gamma L + \Omega(\gamma)t), \tag{5.19}$$

where now time is interpreted as

$$t = \sqrt{Y + Y_0}, \tag{5.20}$$

with $Y_0 = \ddot{X}(\gamma,0)/2b$ and the dispersion relation reads

$$\Omega(\gamma) = \sqrt{\frac{4}{b}X(\gamma,0)}\,. \tag{5.21}$$

Noteworthy, here, the rapidity Y in the time definition is shifted by Y_0 with respect to the leading order result. The constant Y_0 absorbs the arbitrary parameter $\hat{\gamma}$ from $\ddot{X}(\gamma,0)$. Similarly to the LL case the equation for the minimum of phase velocity provides the definition of γ_c

$$\gamma_c\,\Omega'(\gamma_c) = \Omega(\gamma_c). \tag{5.22}$$

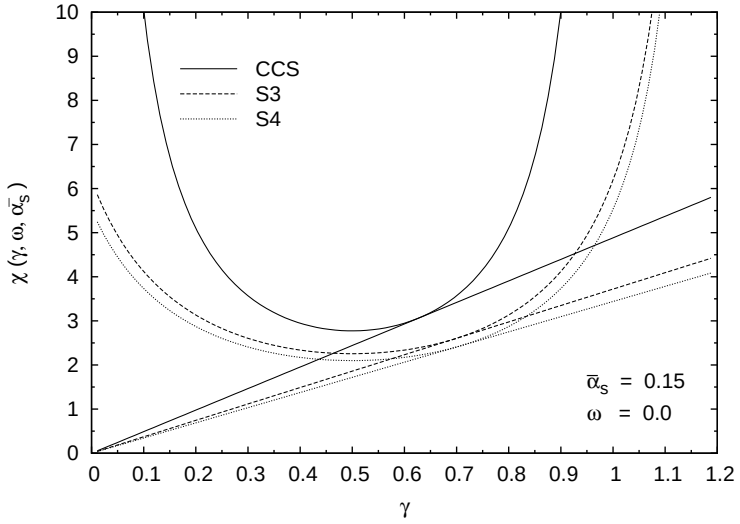

Figure 5.1: Graphical determination of the critical exponent γ_c for three resummed NLL kernels. The curve corresponding to the CCS scheme (at $\omega = 0$) coincides with the LL curve.

However, γ_c determined in such a way still depends on the arbitrary constant $\hat{\gamma}$ via the function $X(\gamma, 0)$. Thus, requiring v_g to be independent of the choice of $\hat{\gamma}$ leads to the condition $dv_g(\hat{\gamma})/d\hat{\gamma} = 0 = dv_g(\gamma_c)/d\gamma_c$. This is because the dependence of the velocity on $\hat{\gamma}$ comes through γ_c only. Applying this condition to Eq. (5.21) leads to

$$\gamma_c \chi'(\gamma_c, 0) = \chi(\gamma_c, 0) \quad \Rightarrow \quad v_g \;=\; \sqrt{\frac{2\chi(\gamma_c, 0)}{b\,\gamma_c}}\,, \tag{5.23}$$

and the arbitrariness related to $\hat{\gamma}$ is eliminated.

As we see from (5.23), the value of γ_c at the NLL level in general depends on the resummation scheme. This is shown in graphical form in Fig. 5.1. Geometrically, the value of γ_c is given by the tangent to the characteristic function of the kernel, different for each NLL scheme. Note also that the curve corresponding to the CCS scheme at $\omega = 0$ is nothing else than the LL curve (*cf.* Eq. (5.7)), and thus the critical parameters are the same in this case. This holds for any other "implicit" scheme which recovers the LL kernel at $\omega = 0$.

5.2.2 Asymptotic solution of the BK equation

The linearized version of the BK equation (5.1) with the kernel expanded around $\omega = 0$ up to the second order and the rapidity variable Y changed to the time variable $t = \sqrt{Y + Y_0}$ is given by

$$\frac{bL}{2t}\,\partial_t \mathcal{N} \;=\; \Big\{ \overbrace{-\frac{b}{2} v_g^2\,\partial_L + \frac{1}{2}\chi''(\,\partial_L^2 + 2\gamma_c\,\partial_L + \gamma_c^2)}^{\text{“LL”}} \underbrace{+\,\frac{1}{2t}\,\dot{\chi}\,\partial_t - \frac{1}{2t}\,\dot{\chi}'\,\partial_L\partial_t - \frac{1}{2t}\,\dot{\chi}'\,\gamma_c\partial_t + \frac{1}{8t^2}\,\ddot{\chi}\,(\partial_t^2 - \frac{1}{t}\,\partial_t)}_{\text{“NLL”}} \Big\}\mathcal{N}, \tag{5.24}$$

were we have used the form of the group velocity from Eq. (5.23) and introduced the following notational shorthands: $\mathcal{N} \equiv \mathcal{N}(L, Y)$, $\chi \equiv \chi(\gamma_c, 0)$ and similarly for the derivatives of the kernel. We singled out two parts in the above equation. The part denoted as "LL" has already been present in the

LL case (*cf.* Eq. (33) from [76]). The remaining part called "NLL" contains new terms which originate from the dependence of the resummed NLL BFKL kernel on ω. In analogy with the leading order case we use the Ansatz (4.16) which transforms Eq. (5.24) into the ordinary differential equation for the function $G(z)$.

The NLL equation (5.24) taken in the limit $\dot{\chi}, \dot{\chi}', \ddot{\chi} \to 0$, when the "NLL" part vanishes, must recover the LL result. This can be obtained only by setting the free parameters α and k to the values determined already in Section 4.4.2, namely $\alpha = \frac{1}{3}$ and $k = \frac{1}{3}$. If we now write the equation for $G(z)$ and organize it in terms of the powers of time, t, we notice that the leading terms are proportional to $t^{-1/3}$. Therefore, in the "NLL" part we should keep only those terms which contribute to the order $t^{-1/3}$. As can be easily checked and as is demonstrated explicitly in Appendix B, the leading behavior of the time derivatives of $\mathcal{N}$ from the "NLL" piece is $t^{1/3}$. However, since each derivative is multiplied by at least the factor t^{-1} this means that the terms in "NLL" part contribute only at the order $t^{-2/3}$. Consequently, the BK NLL linearized equation in this approach has exactly the same form as in the LL case and reduces to the Airy equation

$$\frac{d^2}{d^2 z} G(z) = \frac{b\gamma_c \upsilon_g}{\chi''(\gamma_c, 0)} (z - 4\beta)\, G(z). \tag{5.25}$$

The condition $G(z) \sim z$ as $z \to 0$ allows to fix the constant β to

$$\beta = -\frac{1}{4} \left(\frac{\chi''(\gamma_c, 0)}{\gamma_c\, \upsilon_g\, b} \right)^{\frac{1}{3}} \xi_1, \tag{5.26}$$

where $\xi_1 = -2.338$ is the zero of the Airy function. Finally, the result for the gluon density is given by

$$\mathcal{N}(L, t) = \text{const} \cdot t^{\frac{1}{3}} \cdot \text{Ai} \left(\left(\frac{\sqrt{2\gamma_c b\, \chi(\gamma_c, 0)}}{\chi''(\gamma_c, 0)} \right)^{\frac{1}{3}} \ln \frac{k^2}{Q_s^2(t)}\, t^{-\frac{1}{3}} + \xi_1 \right) \cdot \left(\frac{k^2}{Q_s^2(t)} \right)^{-\gamma_c}, \tag{5.27}$$

and the saturation scale up to a multiplicative constant, k_0^2, has the form

$$Q_s^2(t) = k_0^2 \, \exp \left(\sqrt{\frac{2\chi(\gamma_c, 0)}{b\gamma_c}}\, t + \frac{3}{4} \left(\frac{\chi''(\gamma_c, 0)}{\sqrt{2\gamma_c b\, \chi(\gamma_c, 0)}} \right)^{\frac{1}{3}} \xi_1\, t^{\frac{1}{3}} \right). \tag{5.28}$$

Hence, the solution of the BK equation with the resummed NLL kernel and running coupling, written in terms of t and L, has the same functional form as the solution for the LL kernel found in [76] and recalled in Section 4.4.2, Eqs. (4.34) and (4.35). In particular, in the saturation scale the leading exponential term proportional to the time variable t is supplemented by the second universal term in $t^{1/3}$, sub-leading by order $t^{-2/3}$. There are, however, two potential sources of differences between the solutions at the LL and NLL level. First is the NLL BFKL kernel, $\chi(\gamma_c, 0)$, which is in general different for various resummation schemes. Second difference is the definition of time. Namely, in the NLL case, see Eq. (5.20), we have the shift of Y by some undetermined constant Y_0. Both the issue of the resummation scheme and Y_0 dependence will be addressed in the next section.

5.3 Saturation scales beyond leading order

The saturation scale (5.28) obtained for the BK equation with running coupling and the resummed NLL BFKL kernel contains a dimensional constant k_0^2, which cannot be determined in the framework of the traveling wave approach. Therefore, for the qualitative studies, it is convenient to define the

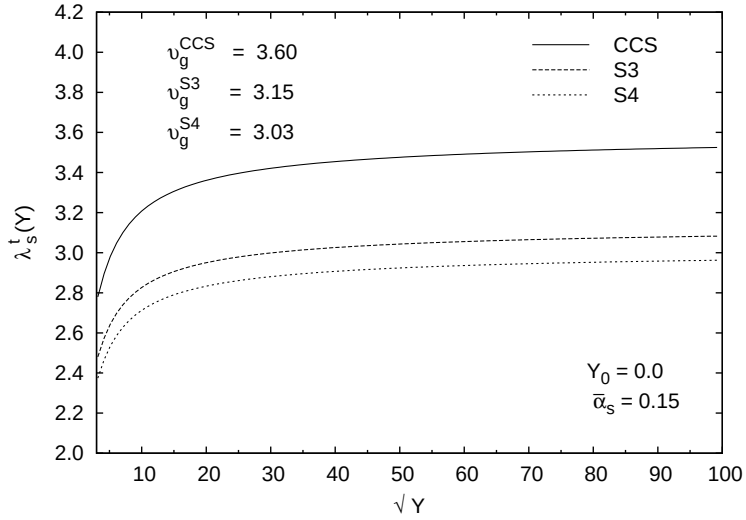

Figure 5.2: The logarithmic derivative λ_s^t for various resummation schemes calculated at $Y_0 = 0$ and $\bar{\alpha}_s = 0.15$.

logarithmic derivatives of Q_s^2. One possible definition, which is motivated by the result (5.28), has the form

$$\lambda_s^t(Y) = \frac{d \ln Q_s^2(Y)}{dt} \,. \tag{5.29}$$

Another commonly adopted definition, reads

$$\lambda_s^{\text{eff}}(Y) = \frac{d \ln Q_s^2(Y)}{dY}. \tag{5.30}$$

The relation between the two derivatives is $\lambda_s^t(Y) = 2t\, \lambda_s^{\text{eff}}(Y)$.

From Eq. (5.29) we obtain

$$\lambda_s^t(Y) = \sqrt{\frac{2\chi(\gamma_c, 0)}{b\gamma_c}} + \frac{1}{4} \left(\frac{\chi''(\gamma_c, 0)}{\sqrt{2\gamma_c b \chi(\gamma_c, 0)}} \right)^{\frac{1}{3}} \xi_1\, t^{-\frac{2}{3}}. \tag{5.31}$$

We recall that the time t is defined by Eq. (5.20), so it contains the arbitrary constant Y_0. In Fig. 5.2 we show λ_s^t from Eq. (5.31), with $Y_0 = 0$, as a function of $\sqrt{Y}$ for the three different resummation schemes S3, S4 and CCS and the value of the coupling $\bar{\alpha}_s = 0.15$. The result depends on the scheme used. In the limit $\sqrt{Y} \to \infty$ the logarithmic derivative λ_s^t approaches its asymptotic value equal to the group velocity υ_g. As we see in Fig. 5.2, in agreement with Eq. (5.23), the value of υ_g is also scheme-dependent.

5.3.1 CCS scheme

By construction, the NLL BFKL kernel resummed in this scheme and taken at $\omega = 0$ reduces to the LL kernel. Indeed, from Eq. (5.7) we have $\chi_{\text{CCS}}(\gamma, \omega = 0) = \chi_0(\gamma)$. In mathematical terms, this means that the CCS scheme falls into the same universality class of solutions as the equation with the LL kernel and running coupling constant.

The result for the saturation scale from the evolution equation with the NLL BFKL kernel resummed in the CCS scheme was also obtained earlier, using a different method, by Triantafyllopou-

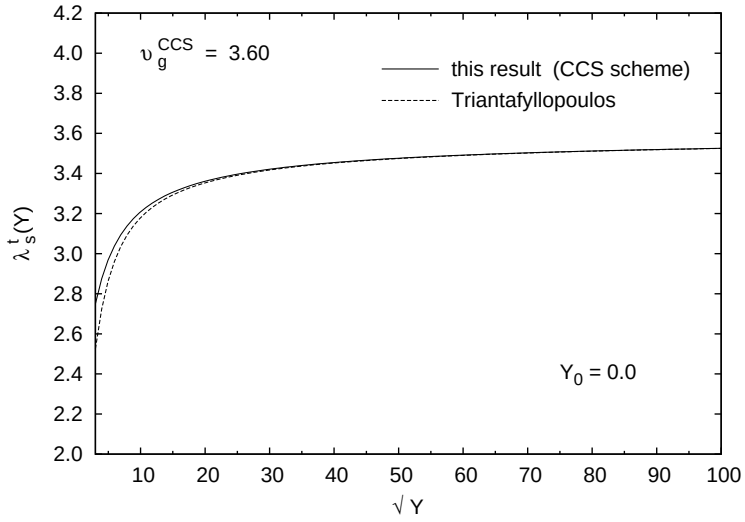

Figure 5.3: Comparison of the logarithmic derivative λ_s^t obtained in the traveling waves approach with the result of [90]. For the sake of compatibility we use CCS scheme and $Y_0 = 0$. The corresponding formulas are given in Eqs. (5.31) and (5.32).

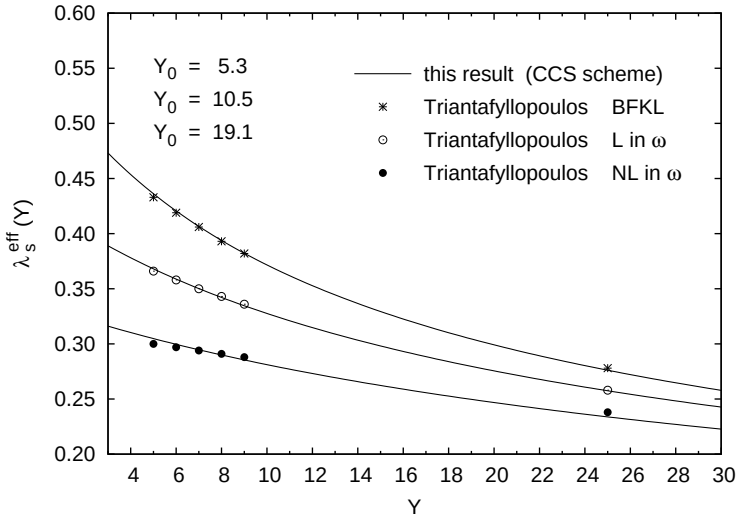

Figure 5.4: Comparison of the logarithmic derivative $\lambda_s^{\rm eff}$ obtained in the traveling waves approach in the CCS scheme and for various Y_0 values with the results of [90]. The notations BFKL, "L in ω", "NL in ω" correspond to the running coupling with the LL kernel and two different treatments of the CCS scheme, respectively. See [90] for details.

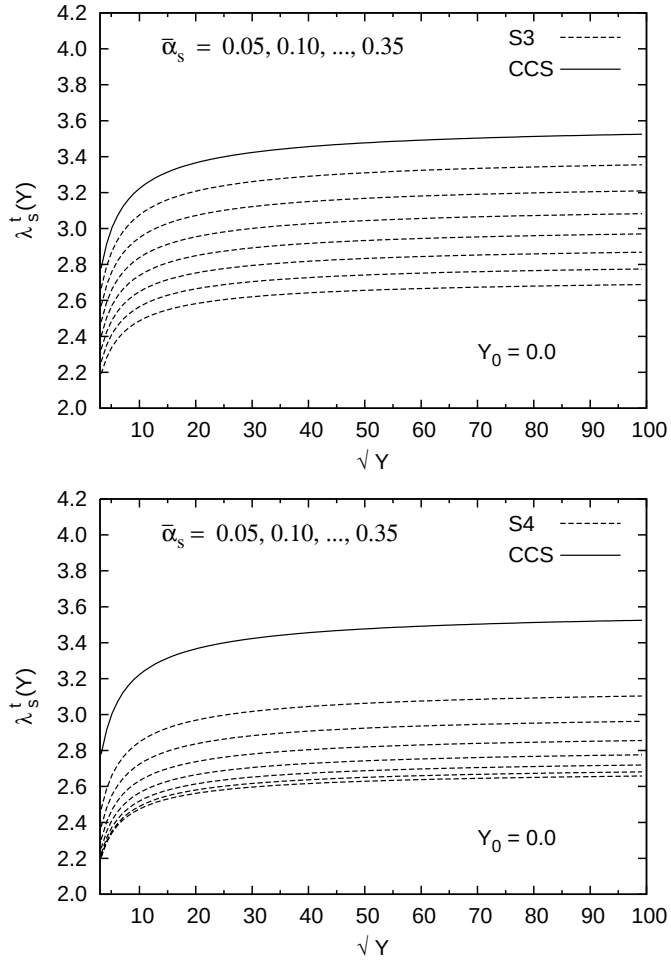

Figure 5.5: Dependence of the logarithmic derivative λ_s^t obtained in the traveling waves approach in the S3 and S4 schemes as a function of $\bar{\alpha}_s$. Top: S3 scheme; Bottom: S4 scheme. The curves go up when the value of $\bar{\alpha}_s$ decreases. The fixed curve corresponding to the CCS scheme, *i.e.* the same as for LL kernel, is also indicated in both cases.

los [90]. In this approach applied first to the LL case in [78], one considers only the linear evolution supplemented by the absorbing boundary conditions. This results at LL level have been shown in [75–77] to agree with the traveling waves approach for fixed and running coupling.

The NLL result [90] goes beyond the asymptotic regime, which unavoidably requires some parametrization of the subleading, non-universal terms. Extracting the asymptotic analytic form of the solution found in [90] (*cf.* Eqs. (58) and (59) therein) , and after changing it to our notations, one obtains

$$\lambda_s^t(Y)\Big|_{\text{from [90]}} = \sqrt{\frac{2\chi(\gamma_c,0)}{b\gamma_c}} + \frac{1}{4}\left(\frac{\chi''(\gamma_c,0)}{\sqrt{2\gamma_c b\chi(\gamma_c,0)}}\right)^{\frac{1}{3}} \xi_1\left(t - \sqrt{\frac{2b}{\gamma_c\chi(\gamma_c,0)}}\right)^{-\frac{2}{3}}. \qquad (5.32)$$

We see that the two results (5.31) and (5.32) are consistent up to the corrections of the order $t^{-5/3}$. However, this are the higher order corrections, which are not expected to be universal and are beyond the scope of our analysis. In Fig. 5.3 we show the comparison of our result for λ_s^t from Eq. (5.31) and the expression (5.32) derived from the result obtained by Triantafyllopoulos [90]. We observe that they converge for the asymptotic values of Y.

Let us finally comment on the following observation. Even though our expression for the saturation scale was obtained for asymptotic Y it can successfully mimic the results from [90] valid at phenomenological rapidities. This is attained by adjusting the value of Y_0 in the definition of time. In Fig. 5.4 we compare λ_s^{eff}, defined in Eq. (5.30), with appropriate Y_0, with the same quantity calculated by Triantafyllopoulos within three scenarios. These scenarios are called by the author: BFKL, L in ω and NLL in ω (see [90] for details). Here we mention only that the last case, NLL in ω, contains most of the higher order, non-universal corrections and is therefore expected to give values of λ_s^{eff} which are the closest to those extracted from the experimental data. The agreement manifested in Fig. 5.4 means that in our approach, varying Y_0 plays the rôle of parametrizing typical non-universal terms, *i.e.* terms which depend on the initial conditions, details of the kernel, or of the method used for extracting the asymptotic behavior. We note also that when Y_0 is large compare to Y the effective leading energy growth of the saturation scale changes from $e^{\lambda\sqrt{Y}}$ to $e^{\lambda Y}$. This is because for $Y_0 \gg Y$ we have $\sqrt{Y+Y_0} \simeq \sqrt{Y_0} + Y/(2\sqrt{Y_0})$.

5.3.2 S3 and S4 schemes

These schemes give the values of γ_c and υ_g different than those from the LL analysis. In that sense, one can say that they do not lie in the same universality class as the previous scheme. This is because the resummed kernels depend explicitly on the the value of the coupling constant. This is depicted in Fig. 5.5, where one can see how the time derivative of the saturation scale varies with $\bar{\alpha}_s$.

Hence, we obtain the new result from the QCD traveling waves approach that the specific asymptotic solutions of the BK equation at NLL accuracy depend parametrically on the resummation schemes. In our case, we identify two distinct classes or resummation kernels which we call “explicit” and “implicit”.

5.4 Concluding remarks

In this chapter we have studied the Balitsky-Kovchegov equation with the running coupling and the renormalization group improved NLL BFKL kernel. Using the method of traveling waves we obtained the asymptotic solution of this equation, valid in the limit of large rapidities Y. This solution obeys universality properties, *i.e.* it is independent of the specific form of the initial conditions, the detailed form of the kernel and the nonlinearities.

We have found that the results for the gluon density and the saturation scale take the same functional forms as in the case of leading order BK equation with running coupling studied in [76]. This is because those pieces in the NLL BK equation (5.1) which originate from the dependence of the kernel on ω and are new with respect to the LL BK equation (4.28), do not contribute to the first two universal terms in the solution. We have shown, however, that the result acquires a parametric dependence on the scheme in which the NLL BFKL kernel is resummed.

We summarize our discussion of the proton structure, studied in the deep inelastic scattering processes, in Fig. 5.6. Perturbative QCD is applicable if $Q^2 \gg \Lambda^2$. The non-perturbative regime must be modeled. The photon with virtuality Q^2 can only resolve objects with the transverse size larger than $\sim 1/Q$. Hence, increasing Q^2 may be interpreted as improving the resolution which leads to the growth of the number of partons seen by the virtual photon, hence, the increase of the parton distribution functions. In the regime of the moderate values of x-Bjorken, the rise of parton distribution functions with increasing Q^2 is described by the linear DGLAP equation. As shown schematically in Fig. 5.6, the spatial density of partons in the transverse plane decreases with improved resolution. This density can be, however increased if, at the fixed value of Q^2, one increases the center-of-mass energy of the $\gamma^* p$ system, W^2. This is equivalent to reducing x. If the photon virtuality is not too large and the system of gluons is dilute the evolution of parton densities with x follows the linear BFKL

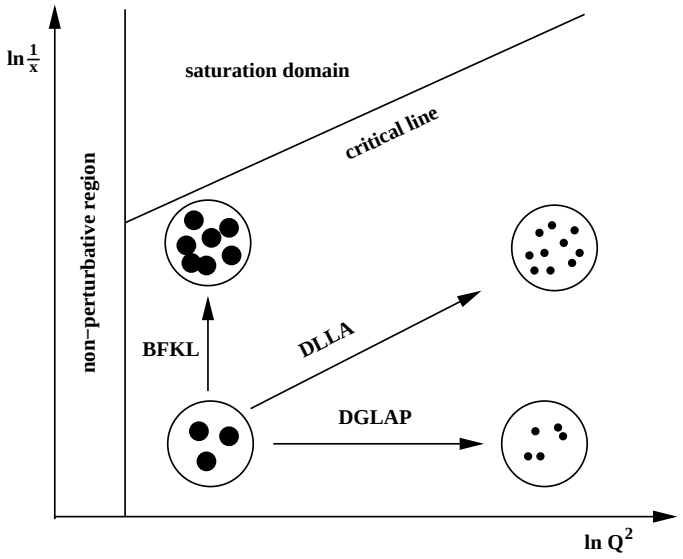

Figure 5.6: Parton densities in the proton and their evolution in the (x, Q^2) space.

equation. However, the power-like energy growth generated by this equation must be slowed down if the system of gluons becomes dense and one enters the so called saturation regime. The line which marks the transition to this regime is called the saturation line or the saturation scale. In this Thesis, we have analyzed, in particular, the proton structure in the region in the (x, Q^2) plane that is close to the saturation line. In Chapter 3 we studied the phenomenological GBW model and its extensions. In this chapter we analyzed the nonlinear BK equation.

The properties of the solutions of the BK equation with running coupling and the LL as well as NLL BFKL kernel are in qualitative agreement with the features of the saturation model from Chapter 3.

In particular, in both cases the elastic dipole scattering amplitude (or the dipole cross section, *cf.* Eq. (4.2)) admit the geometric scaling property. This scaling is, however, not exact. In the saturation model it is broken by the finite quark mass or the DGLAP evolution of gluon density, as reflected in the behavior of the dipole cross section in Fig. 3.4. In the solution of the BK equation (5.27) we have, in turn, the explicit dependence on t, that is on rapidity Y, which amounts to the violation of scaling. Let us stress that the scaling of the cross section, which is to some extent broken is also suggested by the experimental data as depicted in Fig. 3.3.

The result for the saturation scale obtained in this chapter is, in principle, valid only at asymptotically large values of Y. We have shown, *cf.* Eq. (5.28), that the leading behavior of the saturation scale in the limit of large rapidities is $Q_s^2(Y) \sim \exp(\lambda\sqrt{Y + Y_0})$, where Y_0 is an arbitrary parameter in our approach. In the saturation model, in turn, this scale, which is valid also at phenomenological rapidities has the form $Q_s^2(Y) \sim \exp(\lambda Y)$.

In our study of the BK equation we have found that the dependence of the saturation scale may effectively look as $\exp(\lambda Y)$ provided that one adjusts accordingly the value of Y_0. This is because the non-zero value of Y_0 in the traveling waves formalism generates and parametrizes the higher order, non-universal corrections, which are relevant at phenomenological rapidities. In addition we have shown that by this simple procedure one reproduces the result from [90] for the non-asymptotic Y.

Let us finish the discussion of the saturation physics in DIS by commenting that our considerations were confined to the mean field approximation in which one neglects the effects of fluctuations in the number of color dipoles in the photon wave function. These effects are important in the low density

region of dipoles with very small sizes. As has been shown in [92–99], at extremely small x one should expect the geometric scaling to be washed out be the fluctuations. Instead, the new form of scaling, called *diffusive scaling* appears with the scaling variable of the $\gamma^* p$ cross section being $\ln[Q^2/Q_s^2(x)]/\sqrt{D\ln(1/x)}$, which replaces $Q^2/Q_s^2(x)$. The values of x-Bjorken at which this new type of scaling should be visible are probably very small, especially that, as shown in [100], taking into account the running coupling effects strongly suppresses fluctuations.

Chapter 6

Time-like branchings and jets

Quarks and gluons can be either exchanged or emitted. In the first case the virtuality $t \equiv E^2 - p^2$ is negative, $t < 0$, and we call the parton *space-like*. In the second case, $t > 0$, we deal with the *time-like* parton. Those partons may, in turn, split into objects with lower virtualities. When the space-like quark or gluon emits a time-like parton, the process is called space-like (or t-channel) branching. The deep inelastic scattering, which we have studied in the preceding chapters, is certainly the most important example of the t-channel process. In analogy, if the time-like parton splits into two time-like objects, we call the branching time-like (or s-channel). The sequence of time-like branchings leads to the production of jets of particles. In the current chapter, we discuss the basic facts concerning these interesting objects as well as introduce a formalism in which they can be studied.

Before we turn entirely to the discussion of the time-like processes, let us try to point out the similarities of the latter to the space-like processes, studied in detail in the previous part of this Thesis. The space-like and time-like branching, for the process $g \to gg$, is represented in a diagrammatic form in Figs. 6.1a and 6.1b, respectively. The leading behavior of the corresponding expressions for the radiation probability is given by

$$d\sigma = \frac{\alpha_s}{2\pi}\frac{dz}{z}\frac{dk_\perp^2}{k_\perp^2} \qquad \text{for space-like branching,} \tag{6.1}$$

$$d\sigma = \frac{\alpha_s}{2\pi}\frac{dz}{z}\frac{d\theta}{\theta} \qquad \text{for time-like branching,} \tag{6.2}$$

where, in accordance with the notation introduced in Figs. 6.1a and 6.1b, z may be interpreted as the parent parton energy fraction carried by the emitted gluon whereas $\mathbf{k}_\perp$ is its transverse momentum. In the case of time-like branching θ, denotes the angle between the two gluons created in the splitting.

We see from Eqs. (6.1) and (6.2) that the branching probability is greatly enhanced if the emitted *gluon is collinear*, which means that it has small transverse momentum (or equivalently small emission angle), and the *gluon is soft* which means that it carries a tiny fraction of the parent parton energy. In fact, the formula (6.1) has been already introduced in Chapter 1, see Eqs. (1.28) and (1.31), where we have shown that it leads to the appearance of the large logarithms of transverse momentum or energy, which compensate the smallness of the coupling. Here, we see that this formula has its time-like analogue (6.2), which will lead to the enhancement of the soft and small-angle branchings in the s-channel.

As argued in Chapters 1 and 2, the infinite resummations are required in order to properly describe the DIS processes. Due to the similar nature of the gluon radiation in the t- and s-channel, which is manifested in Eqs. (6.1) and (6.2), the infinite set of graphs must be also resummed if one studies the production of highly energetic jets. In the case of DIS the space-like quark or gluon from the hadron decreases its virtuality by successive emissions of collinear gluons until it reaches the scale of the

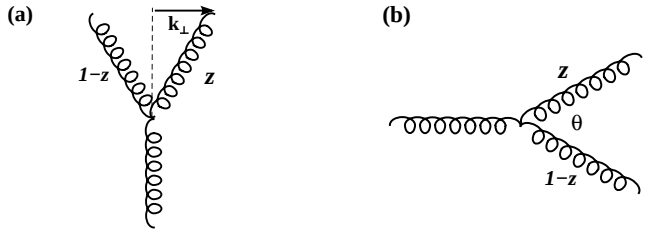

Figure 6.1: Space-like (t-channel) and time like (s-channel) branchings.

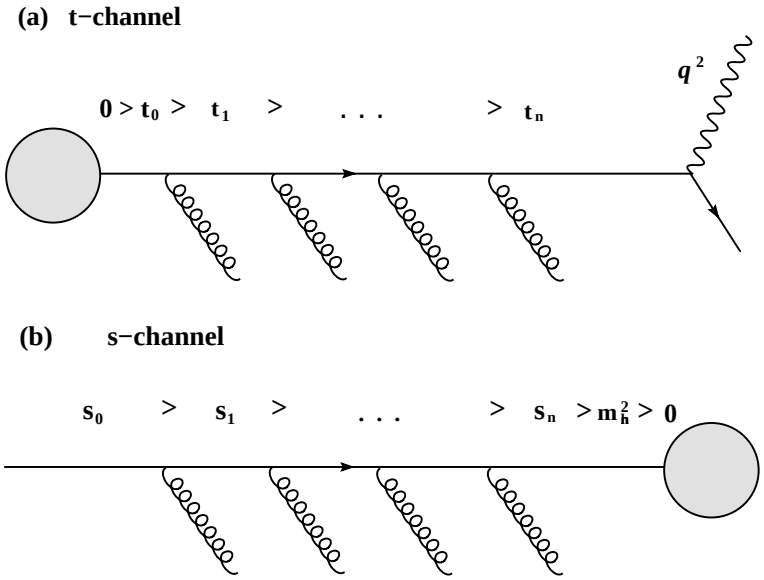

Figure 6.2: Multi-gluon branching processes: (a) Initial-state branching in deep inelastic scattering. (b) Final state branching in the production of jet.

photon with virtuality $q^2 < 0$. The corresponding multi-gluon emission process, depicted in Fig. 6.2a, is also called the *initial state branching*. In the case of jets the cascade is initiated by the time-like parton created for instance in the e^+e^- or $p\bar{p}$ collision at high center-of-mass energy. Such parton also looses its virtuality by the series of emissions of collinear (or collinear and soft) gluons, as shown in Fig. 6.2b, and it hadronizes at the virtuality scale of the hadron mass. This process is called the *final state branching*.

6.1 Fragmentation of time-like partons

Let focus on the case in which, at the beginning of the evolution, we have a quark or a gluon with positive virtuality. This parent parton will reduce its virtuality by emitting soft, time-like gluons. Such process will continue until a non-perturbative scale Q_0^2 is reached. At this virtuality, called the *hadronization scale*, we loose the theoretical control over the evolution. All that happens below Q_0^2, in particular the transition of colored quarks and gluons into colorless hadrons, can be only modeled. This comes under the name of *hadronization*.

The distributions of hadrons inside a quark or a gluon are called the hadronic *fragmentation functions*. These objects are complementary to the distributions of partons inside a hadron, *i.e.* the parton

distribution functions, discussed in Sections 1.4 and 1.5. Similarly to the space-like case, also here the perturbative and the non-perturbative contributions can be factorized. Hence, the fragmentation function D_a^h for the parton a with positive virtuality Q^2 going into the hadron h which carries the fraction x of the parton light-cone momentum can be written in the form [101]

$$D_a^h(x,Q^2) = \int_0^1 \frac{dy}{y} D_a^b(y,Q^2,Q_0^2) h_b^h\left(\frac{x}{y},Q_0^2\right), \tag{6.3}$$

where $D_b^a(y,Q^2,Q_0^2)$ is the partonic and $h_b^h\left(\frac{x}{y},Q_0^2\right)$ the hadronic fragmentation function. The former is the inclusive distributions of partons of type b evaluated the scale Q_0^2 in the parton a with virtuality Q^2. This function is an entirely perturbative object. The latter, being in contrast non-perturbative, describes the transition of the parton b with virtuality Q_0^2 into the hadron h.

This collinear factorization formula (6.3) is a time-like analogue of Eq. (1.42) and, as in the space-like case, the evolution of $D_b^a(y,Q^2,Q_0^2)$ is governed by the equation that can be derived in the framework of pQCD. The analogy is, however, not exact since it turns out that in the case of time-like evolution the interference terms can be neglected only if the momentum fraction x is of the order of unity. Customary, one uses the DGLAP equation to calculate the partonic fragmentation function just for $x \gtrsim 0.1$. In these equations, similarly to the space-like case, the evolution parameter is a decreasing parton virtuality. However, the space-like and time-like splitting functions are the same exclusively at the leading order. As we will explain in Section 6.2, the destructive quantum interference plays a crucial role in the description of small-x fragmentation. The equation which has to replace DGLAP in this regime is called MLLA [102, 103]. The evolution parameter in this equation is no longer parton virtuality but the decreasing angle between two partons created in the splitting. The MLLA equation is discussed at length in Section 6.3.

To obtain a physical cross section the structure functions have to be convoluted with the cross section for hard process in which the quark or gluon is created. For instance, if we consider e^+e^- annihilation at the center-of-mass energy $\sqrt{s}$, the cross section for the inclusive production of hadron h at the lowest order is given by

$$\frac{1}{\sigma_{\text{tot}}}\frac{d\sigma^h}{dx} = \frac{\sum_q e_q^2 D_q^h(x,Q^2)}{\sum_q e_q^2}, \tag{6.4}$$

where σ_{tot} is the total hadronic cross section, $Q = \sqrt{s}/2$ and $x = 2p/\sqrt{s}$, with p denoting the hadron momentum.

As signaled already at the beginning of this chapter, due to the collinear enhancement of the gluon emission, the produced partons are highly collimated in the direction of the original parent quark or gluon. Such an object is called *jet*. The leading order formula (6.4) corresponds to creation of two back-to-back jets in the process $e^+e^- \to q\bar{q} \to (2\text{ Jets})$. The emission of the large angle gluon off the quark or anti-quark line is suppressed by α_s, which in contrast to the collinear gluon, is not balanced by the large logarithm. Such process, although less probable, occurs and leads to the three jets event. Similarly, the events with N jets can be discussed. This goes under the name of the *inter-jet structure*. At the same time, each jet has its own substructure characterized *e.g.* by longitudinal or transverse momentum distributions of particles as well as by ratios of hadron species. This belongs to *intra-jet structure*, which will be the subject of the succeeding sections and the study described in Chapter 7. Let us conclude that the separation of the inter- and intra-jet activity is always somewhat arbitrary, depending on the precise definition of the jet. This concerns, in particular, the adopted size of the *jet opening angle*, which is a polar angle measured with respect to the jet axis. The issue of jet finding algorithms is, however, beyond the scope of our discussion. Hence, it what follows we assume that we have a well separated jet characterized by an opening angle θ_c.

6.2 Coherent branchings and double logarithmic approximation (DLA)

In this section we are interested in calculating the dominant contribution to the distribution of soft gluons inside a quark or a gluon or, equivalently, the partonic fragmentation functions. This means that we are going to study a multi-gluon final states of the type

$$q(g) \to q(g) + g_1 + g_2 + \dots g_N, \tag{6.5}$$

where the parent quark (q) or gluon (g) may be created for instance in the e^+e^- or pp collisions.

As in the space-like case, we exploit the freedom of the gauge choice and this time we select the *planar gauge* defined as [6]

$$A^a_\mu n^\mu = B^a(x), \tag{6.6}$$

where $B^a(x)$ is the scalar field taking values in the Lie algebra of SU(3). The gluon propagator in this ghost-free gauge has the relatively simple form [4]

$$\begin{aligned} G^{ab}_{\mu\nu}(k) &= \delta^{ab}\frac{d_{\mu\nu}(k)}{k^2+i\epsilon}, \\ d_{\mu\nu}(k) &= g_{\mu\nu} - \frac{k_\mu n_\nu + n_\mu k_\nu}{k\cdot n}, \qquad n^2 < 0. \end{aligned} \tag{6.7}$$

In contrast to the light-cone gauge, discussed in Section 1.3, here the vector n is not light-like. For the specific case of e^+e^- collision choosing n to be proportional to the total four-momentum of the e^+e^- pair proves to be most convenient since this results in vanishing of the interference terms between the emissions from q and $\bar{q}$. Hence, the quark and anti-quark radiate soft gluons independently. We may also write $d_{\mu\nu}$ in terms of the gluon polarization vectors $e^{(\lambda)}_\mu(k)$

$$d_{\mu\nu}(k) = -\sum_{\lambda=0}^{3} e^{(\lambda)}_\mu(k) e^{(\lambda)}_\nu(k). \tag{6.8}$$

In the planar gauge the unphysical polarizations, $e^{(0)}_\mu$ and $e^{(3)}_\mu$, are strongly suppressed and gluon has, effectively, only two transverse polarizations. This is the reason why the above gauge is also referred to as the physical gauge.

Since we study the leading order approximation we need to identify in the first place the regions of phase space from which the dominant contributions to the cross section come. Let us begin with a simple process of two gluon emission off a quark

$$q \to q(p) + g_1(k_1) + g_2(k_2). \tag{6.9}$$

The three possible, leading order graphs are shown in Fig. 6.3, where $k_i = (\omega_i, \mathbf{k}_i)$ is the four-momentum of the ith gluon. The corresponding amplitudes can be written as

$$M_a = g^2 \frac{e^{(2)}p}{k_2 p}\frac{e^{(1)}p}{(k_1+k_2)p} t^{a_2}t^{a_1}, \tag{6.10}$$

$$M_b = g^2 \frac{e^{(1)}p}{k_1 p}\frac{e^{(2)}p}{(k_1+k_2)p} t^{a_1}t^{a_2}, \tag{6.11}$$

$$M_c = g^2 e^{(1)\mu} e^{(2)\nu} \gamma_{\mu\nu\rho}(k_1, k_2, -k)\frac{d^{\rho\sigma}(k)}{k^2}\frac{e^{(2)}p_\sigma}{kp}\, i\, f_{a_1 a_2 c} t^c, \tag{6.12}$$

where a_1, a_2, c denote the gluon color indices and t^{a_1}, t^{a_2}, t^c are the SU(3) generators in the fundamental representation. The gluon polarization vectors are $e^{(1)}$ and $e^{(2)}$. Let us examine first the

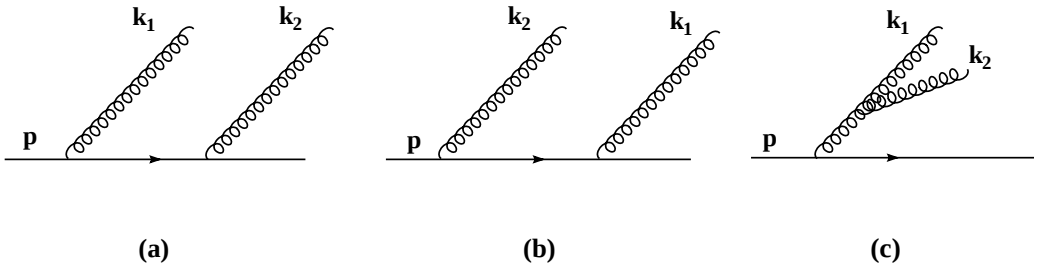

Figure 6.3: Two gluon emission graphs off a quark at leading order.

amplitude M_a. In the region of small emission angles the denominator of (6.10) is proportional to $\omega_2\theta_2^2\,(\omega_1\theta_1^2+\omega_2\theta_2^2)$, where $\theta_{1,2}$ are the angles between $\mathbf{p}$ and $\mathbf{k}_{1,2}$. After taking into account phase space element the contribution to the cross section reads

$$d\sigma_a \sim \alpha_s^2 \frac{d\omega_1}{\omega_1}\,\frac{d\omega_2}{\omega_2}\,\frac{\theta_1\,d\theta_1}{\theta_1^2+\frac{\omega_2}{\omega_1}\,\theta_2^2}\,\frac{d\theta_2}{\theta_2}. \tag{6.13}$$

Thus, we see that in the kinematical region $\theta_1^2 \gg \frac{\omega_2}{\omega_1}\,\theta_2^2$ we obtain the *double logarithmic* (DL) terms in the cross section with one soft energy and one collinear logarithm associated with each gluon emission

$$\sigma_a \sim \alpha_s^2 \int \frac{d\omega_1}{\omega_1}\,\frac{d\omega_2}{\omega_2}\,\frac{d\theta_1}{\theta_1}\,\frac{d\theta_2}{\theta_2} = \left(\alpha_s \ln\omega\,\ln\theta\right)^2. \tag{6.14}$$

This is the region in which the graph from Fig. 6.3a dominates. From symmetry we can instantly establish that the region in which the amplitude M_b, corresponding to Fig. 6.3b, acquires the DL enhancement is $\theta_2^2 \gg \frac{\omega_1}{\omega_2}\,\theta_1^2$. We also notice that the two regions never overlap so the interference term of the type $M_aM_b^*$ is not enhanced logarithmically.

In the above derivation we made no statement about the relative size of the gluon energies ω_1 and ω_2. In fact, without imposing any condition on the ω_2/ω_1 ratio, the only DL contributions come from the graphs (a) and (b) and the cross section is just a sum of $|M_a|^2$ and $|M_b|^2$ with no additional interference terms. This is the case of the time-like DGLAP equation. However, we still have the third graph of Fig. 6.3 c and it turns out that this graph can also contribute to the DL terms in the kinematical region

$$\frac{\omega_1}{\omega_2}\theta_1^2 \gg \theta_2^2 \geq \theta_1^2. \tag{6.15}$$

We see that this contribution can be neglected when $\omega_2/\omega_1 \sim 1$ but it starts to be as important as the diagrams (a) and (b) in the region of the *strong energy ordering*, $\omega_1 \gg \omega_2$. Moreover, in the this case the double logarithmic regions of (a) and (c) overlap and therefore one should expect the interference terms $M_aM_c^*$ to appear in the cross section. The quantum coherence effects are therefore negligible only for relatively large x and in this regime the DGLAP equation may be used to calculate partonic distributions. However, below a certain value of x, typically 0.1, the interference terms provide substantial contribution to the cross section.

Instead of analyzing the interference diagrams, it is more convenient to use a slightly different approach. In the above, we first wrote the diagrams and then associated with them the regions of phase space where each of the diagrams gives the DL contribution. We could approach the problem from the opposite direction by starting from considering three distinct angular regions

$$\begin{aligned} &\text{(I)} && \theta_1 \gg \theta_2, \\ &\text{(II)} && \theta_2 \gg \theta_1, \\ &\text{(III)} && \theta_{12} \ll \theta_1 \approx \theta_2. \end{aligned} \tag{6.16}$$

It is easy to check that in (I) only the graph (a) gives the DL contribution. Similarly, graph (c) dominates in the region (III). For the case of (II) we can split the (θ_1^2, θ_2^2) plane into the region $\theta_2^2 \gg \frac{\omega_1}{\omega_2}\theta_1^2$, where amplitude M_b dominates, and the region $\frac{\omega_1}{\omega_2}\theta_1^2 \gg \theta_2^2 \gg \theta_1^2$, where both M_a and M_c contribute. It can be shown that in this case $M_a + M_c \simeq M_b$ and the expression (6.11) is valid over the entire region (II).

We summarize our considerations on the two gluon emission process by writing down the cross section in the double logarithmic approximation

$$d\sigma \sim \begin{cases} |M_a|^2 & \text{for} \quad \theta_1 \gg \theta_2, \\ |M_b|^2 & \text{for} \quad \theta_2 \gg \theta_1, \\ |M_c|^2 & \text{for} \quad \theta_1 \approx \theta_2 \gg \theta_{12}. \end{cases} \tag{6.17}$$

Other regions of phase space do not provide the terms of the DL type. This, in turn, means that the contribution is non-vanishing only when the second gluon is emitted at the angle which is much smaller than the emission angle of the first gluon. This property is known as the *strong angular ordering*. It can be generalized to the multi-gluon emission processes, which allows to regard this processes as a probabilistic cascade of independent gluon emissions. Hence, imposing the strong angular ordering on the parton shower is equivalent to including interference terms. Since we consider only those terms in the cross section which are enhanced by two large logarithms this approach is known as the *double logarithmic approximation* (DLA). In general, the DLA cross section for N-gluon emission can be written as [4]

$$d\sigma_N = d\sigma_0\, \mathcal{F}^2 \prod_i d\mathcal{K}(\mathbf{k}_i), \tag{6.18}$$

where

$$d\mathcal{K}(\mathbf{k}_i) = \frac{2C_F\, \alpha_s}{\pi} \frac{d\omega_i}{\omega_i} \frac{d^2\mathbf{k}_{\perp,i}}{2\pi\, \mathbf{k}_{\perp,i}^2}, \tag{6.19}$$

and $d\sigma_0$ denotes the cross section for the hard process in which the parent parton is produced. For the case of e^+e^- collision this is just the annihilation process. The factor $\mathcal{F}$ accounts for virtual corrections. All the gluons in (6.18) are strongly ordered in their emission angles. Here, we discussed the cascade initiated by a quark, which we will also call in what follows the *quark jet*. For the case of the multi-gluon emission process off a gluon, *i.e.* the *gluon jet*, the Casimir invariant C_F in Eq. (6.19) has to be replaced by C_A.

When analyzing multi-gluon final states, it is useful to introduce the concept of the *generating functional*. Then, the cross section may be written in the functional form as

$$d\sigma\{u\} = d\sigma_0\, Z\left(\{u\}\right), \tag{6.20}$$

with

$$Z\left(\{u\}\right) = \sum_{N=0}^{\infty} \mathcal{F}^2 \prod_i \int_\Gamma d\mathcal{K}(\mathbf{k}_i)\, u(\mathbf{k}_i). \tag{6.21}$$

We see that the *exclusive* cross section for N-gluon production can be obtained from Eq. (6.20) after applying N functional derivatives and taking the result at $u = 0$

$$d\sigma_N^{\text{excl}} = \left(\prod_{j=1}^{N} d^3\mathbf{k} \frac{\delta}{\delta u(\mathbf{k}_j)} \right) d\sigma\{u\} \Bigg|_{u=0}, \tag{6.22}$$

where the functional derivative is defined as

$$\left(\frac{\delta}{\delta u(\mathbf{k}_i)} \right) u(\mathbf{k}) \equiv \delta^3(\mathbf{k}_i - \mathbf{k}). \tag{6.23}$$

The generating functional also allows to calculate the N-gluon *inclusive* cross section

$$d\sigma_N^{\rm incl} = \left(\prod_{j=1}^{N} d^3\mathbf{k}_j \frac{\delta}{\delta u(\mathbf{k}_j)} \right) d\sigma\{u\} \Bigg|_{u=1} . \tag{6.24}$$

Hence, we see that the functional $Z(\{u\})$ contains all information about the intra-jet momentum distributions.

A gluonic cascade forms the tree-like structure, which can be defined recursively. Let us assume that we have a parton R, which can be either quark ($R = Q$) or gluon ($R = G$), with momentum k emitted at the angle θ. This parton, after a sequence of splittings, will eventually produce a jet described by $Z_R(k, \theta; \{u\})$. If, instead of the whole evolution, we consider only the interval $d\theta$, the parton R can either stay intact or split by emitting a soft gluon. The products of the splitting will evolve to form the jets $Z_R(k, \theta + d\theta; \{u\})$ and $Z_G(k, \theta + d\theta; \{u\})$. This, in turn, leads to the differential equation for the evolution of the generating functional Z with the angle θ. The solution can be easily found and has the form

$$Z_R(p, \theta; \{u\}) = u(p) \exp\left(\int_\Gamma \frac{d\omega}{\omega} \frac{d^2k_\perp}{2\pi k_\perp^2} \frac{C_R}{N_c} \gamma_0^2 \left[Z_G(k, \theta_k; \{u\}) - 1 \right] \right), \tag{6.25}$$

where we have introduced the notational shorthand: $\gamma_0^2 = 4N_c\alpha_s(k_\perp^2)/(2\pi)$. The evolution terminates when $k\theta = Q_0$, with Q_0 being a cut-off on transverse momentum which equals the virtuality at which hadronization starts. In the above, we took the initial condition

$$Z_R(k, \theta; \{u\}) \Big|_{k\theta = Q_0} = u(k), \tag{6.26}$$

which states that if we start the cascade at the hadronization scale Q_0 we can only have the original parton R in the jet.

One of the most important characteristics of a jet is the single parton distribution. It can be obtained from the generating functional using

$$x D_R^i(x, E_R, \theta) \equiv E_i \frac{\delta}{\delta\, u(\mathbf{k}_i)} Z_R(E_R, \theta; \{u(\mathbf{k}_i)\}) \Bigg|_{u=1} . \tag{6.27}$$

The function $D_R^i(x, E_R, \theta)$ is the distribution (density) of partons of type i in the jet with the opening angle θ initiated by the parton R. Here, by x we denote the energy momentum fraction $x = E_i/E_R \approx |\mathbf{k}_i|/E_R$. It is convenient to introduce new variables

$$\begin{aligned} \xi &= \ln\frac{1}{x}, & \xi' &= \ln\frac{E_k}{E_i} = \ln\frac{x}{z}, \\ Y &= \ln\frac{E_R\theta}{Q_0}, & Y' &= \ln\frac{E_R\theta'}{Q_0}, \end{aligned} \tag{6.28}$$

with $z = E_k/E_R \approx |\mathbf{k}|/E_R$ and E_k, θ' being the energy and the emission angle of the intermediate gluons in the cascade. Let us stress that the variable Y from Eq. (6.28) is unrelated to the rapidity Y used frequently in the previous chapters. The motivation for the notation introduced here and adopted in what follows is purely historical. The single power of x on the left hand side of the definition (6.27) comes from the Jacobian related to the change of variables from x to ξ. This is because the function D_R^i is in fact the differential expression, $D_R^i \equiv dD_R^i/dx$, *cf.* Eq. (6.4). Hereafter, for notational simplicity, we will not write this Jacobian explicitly, which means that we adopt the notation $D_R^i \equiv x\, dD_R^i/dx$.

Applying the functional derivative to Eq. (6.25) gives the *DLA equation for particle spectrum* in a jet which reads

$$D_R^i(\xi,Y) = \delta_R^i\delta(\xi) + \int_0^\xi d\xi' \int_0^Y dY' \, \frac{C_R}{N_c}\gamma_0^2 \, D_G^i(\xi', Y' - \xi + \xi'). \tag{6.29}$$

A few comments are in order. Firstly, let us notice that the shift $-\xi + \xi'$ of the second argument of D_R on the right hand side of Eq. (6.29) means that only cascades with strong decrease of energy contribute to the spectrum. Secondly, the lack of the virtual term in Eq. (6.29) reflects the fact that in DLA the recoil effects are not taken into account. In other words, partons do not change their energies even after the emission of an arbitrary number of soft gluons. In the next section we discuss how this important deficiency can be treated by formulating the equation which does justice to the exact kinematics.

The next comment concerns the anomalous dimension. This useful quantity, defined as the derivative of the spectrum with respect to the evolution variable, Y, can be estimated for the case of DLA from Eq. (6.29). Let us notice that the functions $D_{R,G}^i$ on both sides of Eq. (6.29) are of the same order of magnitude. Therefore, the logarithmic integrations have to compensate the coupling, $\int_0^Y dY' \int_0^\xi d\xi' \alpha_s \sim 1$, which means that the integration over Y' as well as ξ' acts effectively as the $\alpha_s^{-1/2}$ factor

$$\int_0^Y dY' \sim \int_0^\xi d\xi' \sim \alpha_s^{-1/2}. \tag{6.30}$$

This should not be surprising given the fact that we are working in the double logarithmic approximation which by definition keeps only terms of the type $\alpha_s \ln^2 \sim 1$. Differentiating Eq. (6.29) with respect to Y gives

$$\partial_Y D_R^i(\xi,Y) = \int_0^\xi d\xi' \, \frac{C_R}{N_c}\gamma_0^2 \, D_R^i(\xi', Y - \xi + \xi'). \tag{6.31}$$

Hence, from the fact that $D_{Q,G}^i \sim 1$ and from Eq. (6.30) we estimate the DLA anomalous dimension as

$$\gamma^{\mathrm{DLA}}(\alpha_s) \sim \partial_Y D_R^i(\xi,Y) \sim \sqrt{\alpha_s}. \tag{6.32}$$

We conclude this section by mentioning that the solution of Eq. (6.29) in the limit of large values of Y has the form

$$D_R^i(\xi,Y) \sim \exp\left(2\gamma_0\sqrt{(Y-\xi)\xi}\right). \tag{6.33}$$

It can be easily checked that the above spectrum has a maximum at

$$\xi_{\mathrm{max}}^{\mathrm{DLA}} = \frac{1}{2}Y, \tag{6.34}$$

the feature which is often referred to as the *hump-backed plateau*. Thus, the particle distribution decreases for large values of x. This is the consequence of the color coherence since imposing strong angular ordering significantly reduces the phase space for emission of soft particles. The small x decrease of the spectrum is expected also from kinematics, however it would lead to twice as rapid growth of the peak position with Y which is excluded by data.

6.3 Modified leading logarithmic approximation (MLLA)

The double logarithmic approximation to the soft gluonic cascades discussed in the previous section gives a very interesting result of the small x decrease of single particle spectra. However, the approximation made in DLA happen to be too severe to obtain the qualitative agreement with experimental data. Therefore, a more refined approach was developed by Dokshitzer, Khoze and Troyan [4, 102, 103], who included the following subleading effects with respect to DLA:

- The effects of running of the strong coupling are taken into account with $k_\perp$ of parton being the argument of α_s.

- The full splitting functions are used instead of solely logarithmically enhanced $1/z$ terms and all splittings are considered that is $g \to gg$, $q \to qg$ and $g \to q\bar{q}$. This means that the decays with $z \sim 1$, which loose one energy logarithm, are also included.

- The configurations with the emission angles comparable in size $\theta_1 \sim \theta_2$ are considered, which results in the loss of one collinear logarithm. This amounts to the prescription of the exact angular ordering.

All these effects provide the contributions of the order α_s to the anomalous dimension and of the order $\sqrt{\alpha_s}$ to the particle spectra. So, we can symbolically write

$$\gamma^{\rm MLLA}(\alpha_s) \sim \sqrt{\alpha_s} + \alpha_s, \tag{6.35}$$

$$D_R^{i,\rm MLLA}(\xi, Y) \sim 1 + \sqrt{\alpha_s}. \tag{6.36}$$

We see that in addition to the DL terms now also the *single logarithmic* (SL) contributions are taken into account. It is highly nontrivial to show that at this accuracy the probabilistic pattern of iterative, independent emissions may be retained. In fact, as demonstrated in [4, 102, 103], the graphs that spoil the probabilistic picture also appear. They provide contributions to the anomalous dimension which are, however, beyond the MLLA accuracy. Hence, the parton decay probability for the process $A \to B + C$ has the the following form, which replaces the DLA formula (6.19)

$$d\mathcal{K}_{BA} = \frac{\alpha(\mathbf{k}_\perp^2)}{2\pi} P_{BA}(z) dz V(\mathbf{n}) \frac{d\Omega}{8\pi}, \tag{6.37}$$

where

$$V_{fg}^s(\mathbf{n}) = \frac{a_{sg} + a_{fg} - a_{sf}}{a_{sf} a_{sg}}, \tag{6.38}$$

$$a_{ik} = 1 - \mathbf{n}_i \cdot \mathbf{n}_k = 1 - \cos\theta_{ik}. \tag{6.39}$$

The partonic cascade forms a "family" where grand the father g emits the father f, which in turn emits the son s. It can be shown that the integration of V_{fg}^s over the azimuthal angle gives the property of the exact angular ordering, namely

$$\int_0^{2\pi} \frac{d\phi}{2\pi} V_{fg}^s(\mathbf{n}) = \frac{2}{a_{sf}} \Theta\left(a_{fg} - a_{sf}\right), \tag{6.40}$$

where Θ is the Heaviside step function.

The *MLLA master equation* for the generating functional reads

$$\frac{\partial}{\partial \ln\theta} Z_A(p,\theta) = \frac{1}{2} \sum_{B,C} \int_0^1 dz \frac{\alpha(k_\perp^2)}{2\pi} \hat{P}_{BA}(z) \left[Z_B(zp,\theta)\, Z_C((1-z)p,\theta) - Z_A(p,\theta) \right], \tag{6.41}$$

where $\hat{P}_{BA}(z)$ are the *unregularized* leading order splitting functions. The term $Z_C((1-z)p,\theta)$ comes from considering also the decays with $z \sim 1$ and the virtual term $Z_A(p,\theta)$ reflect the fact that energy is conserved exactly at each splitting. After applying the functional derivative to (6.41) one obtains the

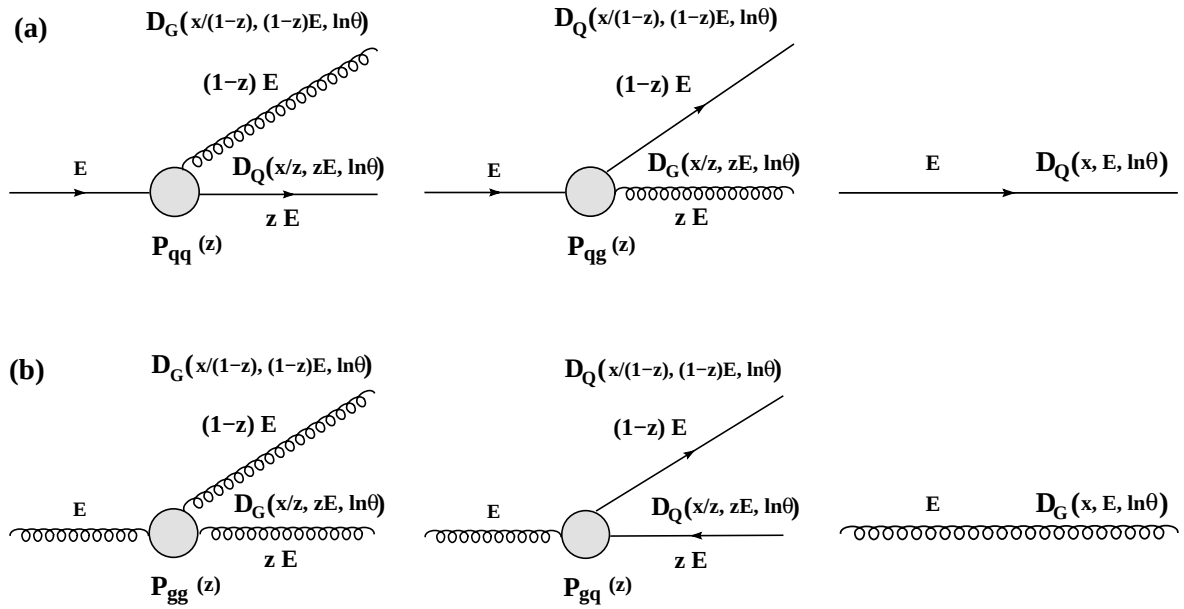

Figure 6.4: The possible processes that may give contribution to the parton density inside the quark (a) or gluon (b) jet at the scale $\ln\theta + \delta h$ and lead to the evolution equations (6.42).

system of two coupled equations for the single inclusive parton momentum distributions in the quark and gluon jet

$$
\begin{aligned}
\partial_Y D_Q(x,Y) &= \frac{1}{2}\int_0^1 dz\,\frac{\alpha_s(k_\perp^2)}{\pi}\,\Theta(z(1-z)E\theta - Q_0) \\
&\cdot\Bigg\{\hat{P}_{qq}(z)\left[D_Q\Big(\frac{x}{z},Y+\ln z\Big)+D_G\Big(\frac{x}{1-z},Y+\ln(1-z)\Big)-D_Q(x,Y)\right] \\
&+\hat{P}_{gq}(z)\left[D_G\Big(\frac{x}{z},Y+\ln z\Big)+D_Q\Big(\frac{x}{1-z},Y+\ln(1-z)\Big)-D_Q(x,Y)\right]\Bigg\}, \\
\partial_Y D_G(x,Y) &= \frac{1}{2}\int_0^1 dz\,\frac{\alpha_s(k_\perp^2)}{\pi}\,\Theta(z(1-z)E\theta - Q_0) \\
&\cdot\Bigg\{\hat{P}_{gg}(z)\left[D_G\Big(\frac{x}{z},Y+\ln z\Big)+D_G\Big(\frac{x}{1-z},Y+\ln(1-z)\Big)-D_G(x,Y)\right] \\
&+2n_f\,\hat{P}_{qg}(z)\left[D_Q\Big(\frac{x}{z},Y+\ln z\Big)+D_Q\Big(\frac{x}{1-z},Y+\ln(1-z)\Big)-D_G(x,Y)\right]\Bigg\},
\end{aligned}
\tag{6.42}
$$

where the Heaviside theta function guaranties that there are no emissions of partons with $k_\perp$ below the cut-off value Q_0. The above equations have a clear probabilistic interpretation. Let us consider the probability of finding some parton with momentum fraction x in a quark with energy E and emission angle (being the scale or time of the evolution) corresponding to $\ln\theta + \delta h$. We denote this distribution by $D_Q(x, E, \ln\theta + \delta h)$. During the interval δh our initial quark characterized by E and $\ln\theta + \delta h$ can split according to $\hat{P}_{qq}(z)$ or $\hat{P}_{gq}(z)$ producing the quark and gluon with energies zE and $(1-z)E$. Subsequently, the parton with the energy fraction x can be created by fragmentation of the quark and

gluon with $D_{Q,G}(\frac{x}{z}, zE, \ln\theta)$ or $D_{G,Q}(\frac{x}{1-z}, (1-z)E, \ln\theta)$. There is, however, always a possibility that during the time of evolution δh nothing will happen with the initial quark and afterwards it will fragment with $D_Q(x, E, \ln\theta)$. Thus, on the whole, the quark with energy E at scale $\ln\theta + \delta h$ left alone for the time δh produces the following number of partons with energy fraction x

$$\begin{aligned} & \delta h \int_0^1 dz\, \hat{P}_{qq}(z) \left[D_Q\Big(\frac{x}{z}, zE, \ln\theta\Big) + D_G\Big(\frac{x}{1-z}, (1-z)E, \ln\theta\Big) \right] \\ + \quad & \delta h \int_0^1 dz\, \hat{P}_{gq}(z) \left[D_G\Big(\frac{x}{z}, zE, \ln\theta\Big) + D_Q\Big(\frac{x}{1-z}, (1-z)E, \ln\theta\Big) \right] \\ + \quad & \left[1 - \delta h \int_0^1 dz \left(\hat{P}_{qq}(z) + \hat{P}_{gq}(z) \right) \right] D_Q\Big(x, E, \ln\theta\Big). \end{aligned} \tag{6.43}$$

However, by definition, the same number is given, by the quark fragmentation function $D_Q(x, E, \ln\theta + \delta h)$. Hence, we obtain the equation whose diagrammatic representation is shown in Fig. 6.4a. By taking the limit $\delta h \to 0$ we arrive at the first equation from (6.42). Similarly, the second equation, schematically represented in Fig 6.4b, can be derived.

6.3.1 Solutions of the MLLA equation

The system of equations (6.42) has been approximately solved in the limit of large Y and small x in which one can perform the expansion in powers of $\sqrt{\alpha_s}$. Keeping only the terms of the order $\mathcal{O}(\sqrt{\alpha_s})$ on the right hand side of Eq. (6.42) (*i.e.* terms $\mathcal{O}(1)$ kept in the distributions D_G and D_Q) would reduce the above equations to the DLA equation with running coupling. When one goes one step further and keeps also the terms $\mathcal{O}(\alpha_s)$ (thus terms $\mathcal{O}(\sqrt{\alpha_s})$ in D_G and D_Q) one obtains, in the limit $x \ll 1$, the following approximation of Eq. (6.42)

$$\partial_Y D_Q(x,Y) = \frac{C_F}{N_c} \left\{ \int_0^1 \frac{dz}{z}\, \gamma_0^2(Y + \ln z)\, D_G\Big(\frac{x}{z}, Y + \ln z\Big) - \frac{3}{4}\, \gamma_0^2(Y)\, D_G\,(x,Y) \right\}, \tag{6.44}$$

$$\partial_Y D_G(x,Y) = \int_0^1 \frac{dz}{z}\, \gamma_0^2(Y + \ln z)\, D_G\Big(\frac{x}{z}, Y + \ln z\Big) - \gamma_0^2(Y)\, a_1 D_G\,(x,Y)\,, \tag{6.45}$$

where

$$\gamma_0^2(Y) = \frac{1}{\beta}\, \frac{1}{Y + \ln z + \ln(1-z) + \lambda}, \qquad \lambda = \ln\frac{Q_0}{\Lambda}, \tag{6.46}$$

and

$$a_1 = \frac{1}{4N_c} \left[\frac{11}{3} N_c + \frac{4}{3} n_f T_R \left(1 - \frac{2C_F}{N_c} \right) \right], \qquad \beta = \frac{1}{4N_c} \left(\frac{11}{3} N_c - \frac{4}{3} n_f T_R \right). \tag{6.47}$$

We see, in particular, that at this level of accuracy the equation for the gluon distribution (6.45) is diagonal. Since Eqs. (6.44) and (6.45) are supposed to be valid in the limit of small x, the semi-hard splittings $z \sim 1$ are taken into account only partially and therefore the energy is not conserved exactly. Nevertheless, with respect to the DLA equation (6.31) the two essential improvements are included in Eqs. (6.44) and (6.45):

- the recoil effects, accounted for by the negative term proportional to $-\gamma_0^2(Y) D_G\,(x,Y)$, lead to the softening of the spectra with respect to DLA,
- the running coupling.

It is easy to show that at this accuracy the following relation between the distributions in the quark and gluon jets holds for $\xi \neq 0$

$$D_Q(\xi, Y) = \frac{C_F}{N_c}\left\{ D_G(\xi, Y) + \left(a_1 - \frac{3}{4}\right)\left[\partial_\xi D_G(\xi, Y) + \partial_Y D_G(\xi, Y)\right] + \mathcal{O}(\alpha_s)\right\}, \qquad (6.48)$$

which replaces the DLA relation $D_Q(\xi, Y) = C_F/N_c D_G(\xi, Y)$. This means that in MLLA the intra-jet distributions in a quark and in a gluon differ not only in normalization but also in shape.

The analytic solution of the equation for the gluon jet has been obtained in [4, 102, 103]. In the Mellin space Eq. (6.45) has the form

$$(\omega + \partial_Y)\,\partial_Y D_G(\omega, Y) = \gamma_0^2(Y) D_G(\omega, Y) - a_1\,(\omega + \partial_Y)\,\gamma_0^2(Y) D_G(\omega, Y). \qquad (6.49)$$

After introducing the function $m(\omega, Y) = \gamma_0^2(Y) D_G(\omega, Y)$ and consecutively changing the variable from Y to $t = -\omega(Y + \lambda)$, Eq. (6.49) boils down to the Kummer's equation

$$t\,\partial_t^2\, m(\omega, t) - (t - (B+2))\,\partial_t\, m(\omega, t) - \left(1 - \frac{A}{\omega} + B\right) m(\omega, t) = 0, \qquad (6.50)$$

where we have introduced the notation

$$A = \frac{1}{\beta}, \qquad\qquad B = \frac{a_1}{\beta}. \qquad (6.51)$$

This equation has two independent solutions which are the confluent hypergeometric functions Φ and Ψ. Taking into account the initial conditions for D_G and $\partial_Y D_G$ and transforming the result back to ξ space we finally obtain the solution of Eq. (6.45)

$$D_G(x, Y, \lambda) = \frac{A(Y+\lambda)}{B(B+1)} \int \frac{d\omega}{2\pi i} x^{-\omega}\, K(\omega, \lambda)\, \Phi\left(-\frac{A}{\omega} + B + 1, B + 2, -\omega(Y+\lambda)\right), \qquad (6.52)$$

where we denoted

$$K(\omega, \lambda) = \frac{\Gamma(\frac{A}{\omega})}{\Gamma(B)}\,(\lambda\,\omega)^B\,\Psi\left(\frac{A}{\omega}, B+1, \omega\lambda\right). \qquad (6.53)$$

6.3.2 Hypothesis of local parton-hadron duality (LPHD)

The solution (6.52) gives the momentum distribution of partons inside the gluon characterized by Y. Here, λ (or equivalently Q_0) is a free parameter. Having obtained the partonic spectrum (6.52), can we say something about the distribution of hadrons inside the gluon? Let us recall that the parameter Q_0, introduced to regularize the collinear divergences ($k_\perp > Q_0$), sets the formal boundary on the perturbative approach. We expect that below Q_0 some non-perturbative description of how partons change into hadrons should be used. In principle, one could stop the cascade at $k_\perp = Q_0$ and subsequently employ one of the available hadronization models. Here, however, we are going to proceed differently.

Let us first notice that for large values of Y we can make the approximation $Y + \lambda \approx Y$ in Eq. (6.52). Then, the dependence on λ, and therefore on Q_0, comes only through $K(\omega, \lambda)$. It can be shown that $\omega\lambda \sim \lambda/\sqrt{Y}$, so in the limit of large Y, which we discuss here, we have $\omega\lambda \ll 1$ and it is easy to check that

$$K(\omega, \lambda) \approx \frac{2}{\Gamma(B)}\,(A\lambda)^{B/2}\,K_B\left(\sqrt{4A\lambda}\right) = \text{const}, \qquad (6.54)$$

where K_B is the modified Bessel function of the third kind and of the order B, with B from Eq. (6.51). The above result suggests that for asymptotically large energies the dependence of the shape of the

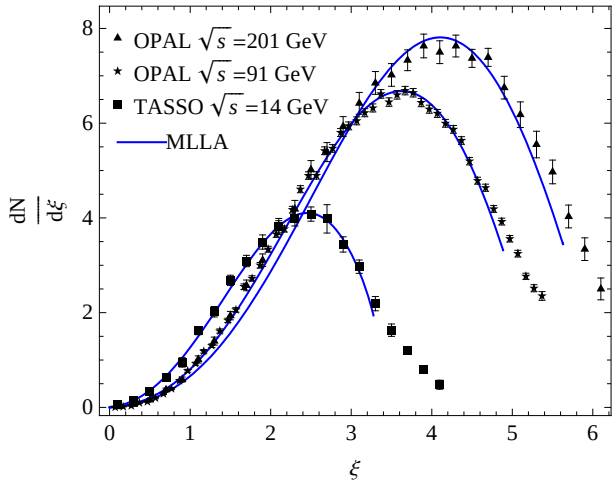

Figure 6.5: Comparison of the MLLA+LPHD predictions with intra-jet distributions of all charged hadrons measured in e^+e^- annihilation by TASSO [107] and OPAL [108, 109].

spectra on the hadronization scale Q_0 disappears and one can expect the hadronic spectra to be very similar to the partonic ones.

This observation supports the idea of the *local parton-hadron duality* [104–106] which states that confinement acts locally in the phase space and consequently the hadronic spectra should be very similar to the partonic spectra differing only by the overall normalization factor, which we will denote in what follows as K_{LPHD}. This means that perturbative evolution determines all the essential features of the hadronic system such as distributions, correlations of particles *etc.*

6.3.3 Limiting spectrum

If, as just argued, the Q_0 dependence is washed out at large Y, it should suffice to study the spectra at $\lambda = 0$. At this value of λ

$$K(\omega, 0) = 1, \tag{6.55}$$

and we obtain the simplified version of Eq. (6.52) which is called the *limiting spectrum*. It has the form

$$D_G^{\lim}(x, Y) = \frac{AY}{B(B+1)} \int \frac{d\omega}{2\pi i} x^{-\omega}\, \Phi\left(-\frac{A}{\omega} + B + 1, B + 2, -\omega Y\right). \tag{6.56}$$

Strictly speaking, choosing the limiting spectrum is some particular way of modeling confinement. Using the integral representation of the confluent hypergeometric function Φ one can derive the expression for the limiting spectrum which is especially convenient for numerical evaluation [102, 103]

$$\begin{aligned} D_G^{\lim}(\xi, Y) \;=\; & A\,\Gamma(B) \int_{-\frac{\pi}{2}}^{\frac{\pi}{2}} \frac{d\tau}{\pi} e^{-B\alpha} \left[\frac{\cosh\alpha + (1-2\zeta)\sinh\alpha}{AY\frac{\alpha}{\sinh\alpha}}\right]^{B/2} \\ & \cdot I_B\left(\sqrt{4\,AY\frac{\alpha}{\sinh\alpha}[\cosh\alpha + (1-2\zeta)\sinh\alpha]}\right), \end{aligned} \tag{6.57}$$

where

$$\alpha = \alpha_0 + i\tau, \qquad \tanh\alpha_0 = 2\zeta - 1, \qquad \zeta = 1 - \frac{\xi}{Y}. \tag{6.58}$$

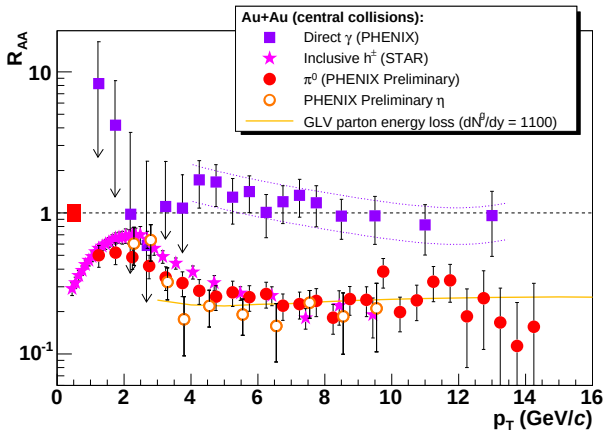

Figure 6.6: Suppression of the high momentum hadrons produced in central Au+Au collisions at 200 GeV at RHIC. Figure from [110].

In Fig. 6.5, we compare the intra-jet distributions of all charged hadrons from the e^+e^- collisions at three center-of-mass energies, $\sqrt{s}$, with the results of MLLA+LPHD. The theoretical curves were obtained from the limiting spectrum (6.57), with $Q_0 = \Lambda = 253$ MeV, multiplied by the accordingly adjusted LPHD factor $K_{\rm LPHD}$. The position of the maximum of the MLLA limiting spectrum (6.57) reads [4]

$$\xi^{\rm MLLA}_{\rm max} = Y\left[\frac{1}{2} + \sqrt{\frac{c}{Y}} - \frac{c}{Y} + \mathcal{O}(Y^{-3/2})\right], \tag{6.59}$$

with $c \simeq 0.29$ for $n_f = 3$. As we see it is larger than in the case of DLA, *cf.* Eq. (6.34). In other words the MLLA spectrum is softer.

6.4 Jet quenching

The particles observed in experiments are hadrons. However, these are not the degrees of freedom of the fundamental theory but the bound states of fields that enter the QCD Lagrangian, namely quarks and gluons. Impossibility of observation of free quarks or gluons has its origin in the essential property of QCD called confinement. It is argued, however, that the confined phase is not the only possible phase of QCD but also the state with *deconfinement* may be attained above a certain value of the energy density. Such phase is referred to as the *quark gluon plasma* (QGP) and is most likely to be created in the collisions of heavy nuclei, with large atomic number A.

Among several possible signatures of the appearance of QGP one considers the phenomenon of attenuation of the yield of high-p_T particles, called *jet quenching*. Hereafter, by p_T we mean the momentum component form the plane that is transverse to the beam axis. At the present state of the art, the following mechanism is believed to dominate. The partons created in the hard process loose more energy when they traverse the medium than in the case of the vacuum. This is due to the medium-induced emission of soft gluons. Hence, the probability that the hadron with high momentum appears at the hadronization scale is diminished for the case of the heavy ion collision.

To quantify the suppression, one defines the *nuclear modification factor* R_{AA}. It is formed as the ratio of the hadron yield in the AA collision to the yield for the case in which one collides the system being the incoherent superposition of A protons.

$$R_{AA}(p_T, y, b) = \frac{d^2N_{AA}/dp_T dy}{\langle T_{AA}(b)\rangle d^2\sigma_{pp}/dp_T dy}. \tag{6.60}$$

Here, p_T is the component of the hadron momentum transverse with respect to the beam and y is the rapidity of the hadron, *cf.* Eq. (2.7). The distance in the transverse plane between the colliding objects well before the interaction is called impact parameter and we denote it as b. The collisions with $b = 0$ are called central and the collisions with large b peripheral. Finally, $\langle T_{AA}(b) \rangle$ is the Glauber overlap function which gives the number of binary pp collisions.

The experimental results from RHIC, where two gold ions are collided at $\sqrt{s} = 200$ GeV, provide the evidence in favor of the attenuation of the high momenta particles [111–114]. As we see in Fig. 6.6, the magnitude of the suppression of hadrons for central collision is $R_{AA} \simeq 0.2$. In Fig. 6.6, data for the modification factor for the case of direct photons is also shown. As we see they are not suppressed. This is because for photons the medium is transparent since they do not interact strongly.

Unfortunately, the measurements of jets is very difficult at RHIC mostly because of the high background and relatively low jet energies. However, this will be possible at the LHC and will allow to test other signatures of jet modification like: jet broadening, softening of the spectra or change of the hadronic composition.

Chapter 7

Hadronic composition as a characteristic of jet quenching

Apart from being excellent objects for the precise study of perturbative QCD, jets may serve also as probes on which new phenomena can leave their signatures. In particular, as briefly discussed in Section 6.4, if the new state of the deconfined matter called the quark gluon plasma is created, the jet that traverses it will certainly differ from the jet which develops in the vacuum. This is because fragmentation pattern changes in the presence of a strongly interacting medium. The experimental result supporting the above picture is the suppression of the high-momentum particles observed at RHIC [111–114]. These measurements can be accounted for by introducing the mechanism of the radiative parton energy loss [115–120], in which the additional medium-induced parton splitting leads to softening of the spectrum and therefore reducing the yield of particles with large p_T.

The p_T-distribution of particles, which is the transverse distribution with respect to the beam axis but the longitudinal distribution with respect to the axis of the jet, is however not the only quantity that can be affected by the medium. Also, the distribution in the momentum transverse to the jet axis is expected to change in the case of medium modified jet. There is however a third class of characteristics, which may show significant medium effects and this is the hadrochemical composition of jet. The current chapter is devoted precisely to this problem.

As a theoretical framework we shall use the perturbative formalism of MLLA, introduced already in Section 6.3, supplemented by the simplest model of hadronization, namely LPHD. This framework is known to provide a reliable description of the charged and identified hadron spectra inside jets and it allows for easy implementation of the medium effects. The analysis presented in this chapter considers only some aspects of the medium modification of jets. Nevertheless, an interesting behavior of the particle spectra and particle ratios can be noticed even in this simplified framework. Moreover, it can serve as a baseline on top of which other effects can be established.

We begin by discussing in Section 7.1 the possible mechanisms that may lead to the change of hadrochemistry of the jets which develop in a medium. In the two following sections we introduce some further facts concerning the MLLA+LPHD formalism. That is, in Section 7.2 the case of jets with restricted opening angles is discussed and in Section 7.3 we explain how one obtains the MLLA jet spectra for identified hadrons. A specific model of the medium modification of jets proposed in [121] is described in Section 7.4. In Section 7.5, we introduce briefly the model of the underlying event which provides an estimate of the background expected at the LHC. The predictions for the modification of jet hadrochemistry at the LHC are given in Sections 7.6, for the case of pure jets, and in Section 7.7, for the case of jets which are not separated from the background. The concluding remarks concerning our study of jet quenching are given in Section 7.8.

The results presented in Sections 7.6 and 7.7 are based on the original publication [122].

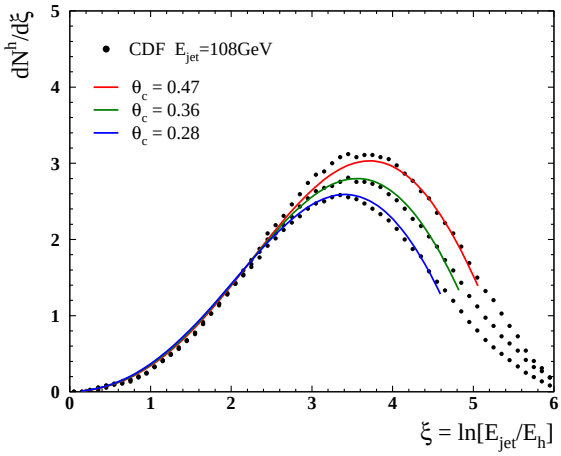

Figure 7.1: The MLLA+LPHD distribution of all charged hadrons in the jet of energy $E_{\rm jet} = 108$ GeV for various opening angles θ_c, compared to CDF data from $p\bar{p}$ collisions [129].

7.1 Conceivable mechanisms of hadrochemistry change

A number of mechanisms of parton energy loss may lead to the change of the hadronic composition of a jet. In particular, the fully realistic model of radiative energy loss (see for instance [123–128]) should take into account the transfer of color between the partons from the cascade and the QCD medium, since this changes the color flow in the parton shower is thus likely to affect hadronization. Similarly, other quantum numbers like flavor or baryon number can, in principle, be exchanged between the medium and the partonic cascade. Another conceivable mechanism would be the recombination of the partons from the shower with those from the medium. In addition, if the energy loss via inelastic collisions is non-negligible than one should take into account also the recoil effects. This, in turn, can lead to the medium components being kicked into the jet cone, which will certainly alter the hadronic composition of the jet. Finally, the elastic interaction of the partons from jet with the medium results in the enhancement of the parton branching probability.

In this study, we consider solely this last mechanism of medium induced radiative energy loss that is we take into account only the elastic scatterings between the partons from the cascade and the medium. Moreover, we do not introduce any changes with respect to the vacuum case at the level of hadronization.

7.2 MLLA spectra within restricted jet opening angle

In Section 6.3 we wrote the solutions of the MLLA equation in terms of the evolution variable Y. The definition of Y for the case of small angles was given in Eq. (6.28). The solution evaluated at a given value of Y corresponds to the jet with energy $E_{\rm jet}$ and opening angle θ_c, which we define as the half-angle of the jet cone. Therefore, the MLLA formalism allows also to determine the spectra of hadrons for the jets with restricted opening angles. When θ_c is not very small one should, however, use the exact definition

$$Y = \ln \frac{E_{\rm jet} \sin \theta_c}{Q_0}. \tag{7.1}$$

To illustrate this point we have plotted in Fig. 7.1 the intra-jet distributions of all charged hadrons, contained inside three different jet subcones of opening angles θ_c. As expected, the yield of hadrons is

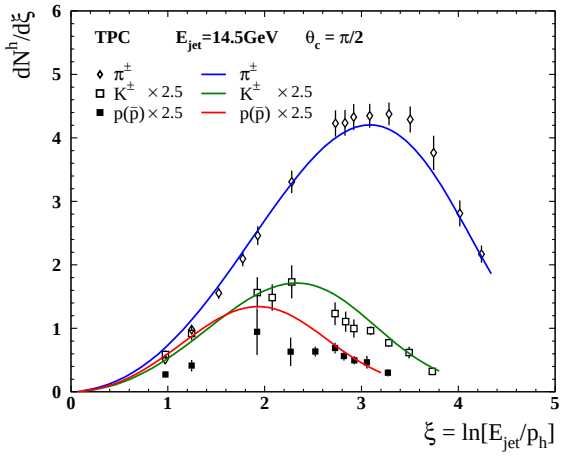

Figure 7.2: The distribution (7.5) of charged pions ($\pi^+ + \pi^-$), kaons ($K^+ + K^-$) and (anti)-protons ($p + \bar{p}$) in the jet of energy $E_{\rm jet} = 14.5$ GeV, compared to TPC data on e^+e^- collisions [130]. For better visibility, rates of kaons and protons are multiplied by the factor 2.5.

greater for the jets with larger aperture. Moreover, with increasing θ_c, the momentum range broadens and the peak position moves towards larger ξ, that is smaller hadron momenta. We also see that the MLLA limiting spectra agree fairly well with the data. Let us stress at this point that we used the common parameters for the three curves that is $\Lambda = Q_0 = 235$ MeV and $K_{\rm LPHD} = 0.555$.

7.3 MLLA spectra of identified hadrons

The MLLA formalism also allows to calculate the spectra of identified hadrons. We have already mentioned that the parameter Q_0 specifies the endpoint of the partonic cascade. In the case of the identified spectra one relates this point with the mass of the hadron, $Q_0 \approx M_h$ [105, 106]. In other words, for the case of heavier hadrons, the perturbative evolution stops earlier and the hadronization occurs at higher virtuality scale.

In order to calculate the spectrum $D_G(\xi, Y, \lambda)$ for $M_h \neq \Lambda$, that is $\lambda \neq 0$, one should in principle perform the complex integration in Eq. (6.52). However, as noticed in Section 6.3.2, at large energies the dependence on λ, and hence on the hadron mass, comes only via the function $K(\omega, \lambda)$, defined in Eq. (6.53), and can be factorized out. Therefore, it is expected in this limit that the shape of the spectrum for $\lambda \sim 1$ will be very close to the shape of the limiting spectrum and the two spectra will differ only by normalization fixed by the factor

$$K_0(M_h) = \frac{2}{\Gamma(B)} (A\,\lambda)^{B/2} K_B\left(\sqrt{4\,A\,\lambda}\right), \qquad \lambda = \ln\frac{M_h}{\Lambda}. \tag{7.2}$$

The energies reached in experiments are, however, not large enough for this asymptotic result to be applicable. Nevertheless, as argued in [105, 106], one can correctly describe the spectra that are presently available by redefinition of the variable ζ appearing in Eq. (6.57), which has the interpretation of normalized rapidity. The more suitable definition of the normalized rapidity is [105, 106],

$$\bar{\zeta} = \frac{y}{y_{\rm max}}, \qquad y = \ln\frac{E_h + p_h}{M_h}, \tag{7.3}$$

and the limiting spectrum (6.57) may be written as a function of $\bar{\zeta}$ by substituting

$$\zeta = 1 - \frac{1}{Y} \ln \frac{\cosh y_{\text{max}}}{\cosh(\bar{\zeta}\, y_{\text{max}})}. \tag{7.4}$$

It can be easily shown that for ultra high energies ζ and $\bar{\zeta}$ coincide. There is, however, another element which has to be taken into account. Namely, in order to properly describe the region of small ξ where the mass of a particle is comparable with its momentum one has to correct the original expression for $D_G^{\text{lim}}(\xi, Y)$ by using exact definition of momentum fraction that is $x_p = p_h/E_{\text{jet}}$ rather than $x = E_h/E_{\text{jet}}$ which appears in Eq. (6.57). By combining all the elements described above one is able to express the distribution of identified hadrons h in the gluon jet by the limiting spectrum

$$x_p \frac{dN^h}{dx_p}(x_p, E_{\text{jet}}, \theta_c, M_h) = K_{\text{LPHD}}\, K_0(M_h)\, \gamma_h\, \frac{x_p^2}{x_p^2 + \left(\frac{M_h}{E_{\text{jet}}}\right)^2}\, D_G^{\text{lim}}(\zeta(\bar{\zeta}), Y, \theta_c), \tag{7.5}$$

where, following [106], we have introduced the factor γ_h, which depends on the hadron species. This factor in commonly used and for instance in the case of kaons it accounts for the fact that the probability of hadronizing into strange hadrons is reduced due to the larger mass of the strange quark. This effect is known as the strangeness suppression. For more details on the derivation of Eq. (7.5), we refer to Appendix C as well as to the original papers [105, 106].

In Fig. 7.2, we compare the distribution (7.5) with the spectra of identified hadrons in jets produced in e^+e^- collision, measured by the TPC collaboration. The limiting spectrum was calculated taking $Q_0 = \Lambda \approx M_\pi$. The parameters were set to $\Lambda = 155$ MeV and $K_{\text{LPHD}} = 1.22$. In accordance with data, one observes that the spectrum becomes harder for more massive hadrons. Also, the mass-dependent hierarchy of hadron multiplicity is reproduced. To account for the strangeness suppression, following [106], we adopted $\gamma_K = 0.73$. The relative normalization $K_0(M_h)$ was calculated from (7.2), in contrast to the original analysis [106], where it was extracted from the fit to the TPC data.

Since we are not aware of an experimental study of the jet hadrochemical composition as a function of the jet opening angle, we assume in what follows that the relative distributions of identified hadron species inside a jet do not change significantly as a function of θ_c, so that the definition (7.1) applies also in this case.

7.4 Borghini-Wiedemann model of medium modification

After discussing the formalism of MLLA+LPHD, which provides a reliable framework for studying the vacuum jets produces in e^+e^- or $pp/p\bar{p}$ collisions, let us turn to the description of jets modified by the dense QCD medium created in the collisions of heavy ions. There is no unique prescription of how to model the fragmentation inside a medium. One possibility to introduce the medium induced gluon radiation into the formalism is to enhance the probability of parton branching. The model of this sort, in which the singular parts of the unregularized splitting functions $\hat{P}_{qq}(x)$, $\hat{P}_{gg}(x)$ and $\hat{P}_{qg}(x)$ are enhanced by one common model-dependent factor $(1 + f_{\text{med}})$, was proposed by Borghini and Wiedemann [121]. Such a treatment is motivated by the calculations of medium-induced gluon radiation of hard partons [123–128]. The regular parts of the splitting functions are beyond control and they are left unchanged in order to avoid introducing additional parameters. Consequently, we have [121]

$$\hat{P}_{qq}(x) \;=\; C_F \left[\frac{2\,(1 + f_{\text{med}})}{1 - x} - (1 + x) \right], \tag{7.6}$$

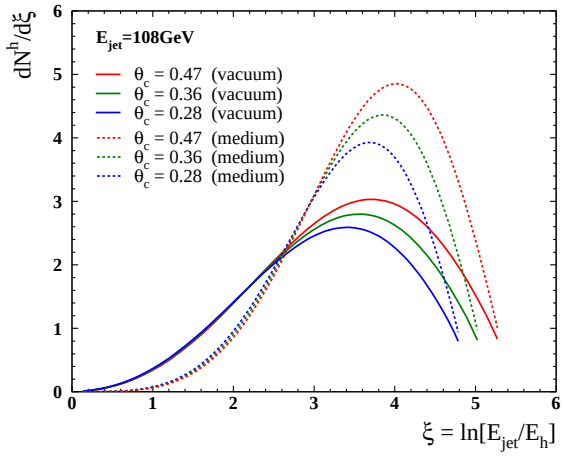

Figure 7.3: Medium modification of the all charged hadrons spectra inside a jet calculated within the radiative energy loss model of Borghini and Wiedemann [121].

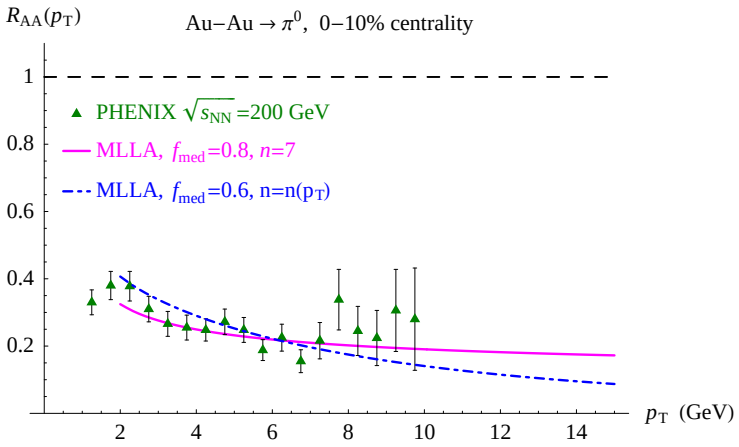

Figure 7.4: Nuclear modification factor $R_{\rm AA}$ obtained from the model [121] compared to the PHENIX data taken from [131]. Figure from [121].

$$\hat{P}_{gq}(x) = C_F \left[\frac{2\,(1+f_{\rm med})}{x} + x - 2 \right], \tag{7.7}$$

$$\hat{P}_{gg}(x) = 2C_A \left[(1+f_{\rm med}) \frac{x}{1-x} + (1+f_{\rm med}) \frac{1-x}{x} + x(1-x) \right], \tag{7.8}$$

$$\hat{P}_{qg}(x) = T_R \left[x^2 + (1-x)^2 \right]. \tag{7.9}$$

The above modification is very easy to implement within the MLLA formalism since it amounts solely to redefinition of the parameters A and B, which appear in Eq. (6.57) as well as in Eq. (7.2) and were originally defined in Eq. (6.51). In the case of medium modified fragmentation these parameters take the form

$$A = \frac{1+f_{\rm med}}{\beta}, \qquad B = \left(\frac{11+12\,f_{\rm med}}{3} N_c + \frac{2}{3} \frac{n_f}{N_c^2} \right) / (4N_c\beta). \tag{7.10}$$

The LPHD-prescription is adopted unchanged in the model [121].

As shown in Fig. 7.3, the single particle intra-jet spectra soften when the partonic cascade develops inside a medium. In Section 6.1 we have explained that these spectra can be interpreted as the fragmentation functions. By convoluting the fragmentation function with the parent parton spectrum one obtains the *single inclusive spectrum* of the leading hadrons that can be used to calculate the nuclear modification factor R_{AA}. The typical distribution of parent partons is power like $1/p_T^{n(p_T)}$, where p_T is the component of the momentum perpendicular to the beam axis. The power $n(p_T)$ depends on the center-of-mass energy and can be taken either as a constant or a more sophisticated function of p_T. The simple model of medium modification proposed in [121] is able to account for the R_{AA} suppression measured at RHIC. As shown in Fig. 7.4, the correct magnitude of quenching is obtained both for the case of partonic spectrum with the constant power, $n = 7$, as well as with the power parametrized as $n(p_T) = 7 + 0.003p_T^2$ and with the value of $f_{\text{med}} = 0.8$ or $f_{\text{med}} = 0.6$, respectively.

7.5 Two component model of underlying event

Jets measured in the heavy ion collisions at the LHC will be always accompanied by a large abundance of the underlying event particles. Therefore, it is important to examine whether the hadrochemistry of the background is similar to that of the jet or whether they are qualitatively different. Moreover, the estimation of the relative yields of the jet and the background particles would allow to asses if the modification of jets can be observed without separating it from background.

In order to estimate the underlying event we use the model proposed in [132, 133] and further explored in [134], in which hadrons are produced via two competing mechanisms, recombination and fragmentation. We limit ourselves to central collisions and we specify the input following [134]. The transverse momentum spectra of hadrons are modeled by a two-component distribution, showing an exponential "thermal" slope at low transverse momentum and displaying a characteristic power-law at high transverse momentum.

We characterize the exponential component of the quark and anti-quark spectrum by the distribution

$$w_i(R,p) \sim e^{-p^\mu u_\mu(R)/T}\,. \tag{7.11}$$

This distribution is assumed to be emitted from spatio-temporal positions $R^\mu = (\tau\cosh\eta, \rho\cos\phi, \rho\sin\phi, \tau\sinh\eta)$, which lie in a thermally equilibrated system at temperature T along a space-like freeze-out hypersurface Σ. Here, η is the space-time rapidity, ρ the radial coordinate, and a suitable hypersurface can be specified by fixing $\tau = \sqrt{t^2 - z^2} = \text{const}$. The system is expanding at position R^μ with a longitudinally boost-invariant flow profile $u_\mu(R)$, which displays a velocity $v_T = \tanh\eta_T$ in the transverse direction. Integrating w_i along the freeze-out hypersurface is a standard procedure to find the soft contribution to the quark spectrum, $dN_a^{\text{soft}}/d^2p_{a,T}\,dy$. In the following, we denote by $p_{a,T}$ the momentum of partons, and by p_T the momentum of hadrons.

The hard, power-law contribution to the quark spectrum is determined by

$$\left.\frac{dN_a^{\text{hard}}}{d^2p_{a,T}\,dy}\right|_{y=0} = K\frac{\bar{C}}{(1+p_{a,T}/\bar{B})^{\bar{\beta}}}. \tag{7.12}$$

Here, the parameters $\bar{C}$, $\bar{B}$ and $\bar{\beta}$ are taken from the leading order perturbative QCD calculations [135] and the constant $K \simeq 1.5$ accounts for higher order corrections [132, 133]. Parton energy loss is modeled by quenching this partonic spectrum via shifting its momentum distribution by $\Delta p_{a,T}(p_{a,T}) = \epsilon_0\sqrt{p_{a,T}}$, as suggested in [136].

We now explain how these partonic spectra are turned into hadronic yields. For an exponential spectrum based on (7.11), recombination always wins over fragmentation, since there are exponentially many recombination partners at soft p_T. For a power-law tail (7.12), however, fragmentation

wins over recombination, since there are sufficiently many high-p_T components which can fragment into softer ones. Thus, the partonic $p_{a,T}$-scale at which the power-law contribution (7.12) overcomes the exponential one sets the hadronic p_T-scale at which fragmentation starts to dominate over recombination [132].

The momentum spectrum for mesons and baryons from recombination can be written as [132,134]

$$\left.\frac{dN_{M,B}}{d^2p_T\,dy}\right|_{y=0} = C_{M,B} M_T \frac{\tau A_T}{(2\pi)^3}\, 2\,\Pi_a\,\gamma_a\, I_0\left[\frac{p_T \sinh\eta_T}{T}\right] k_{2,3}(p_T)\,, \tag{7.13}$$

where γ_a are quark fugacities, $C_{M,B}$ the degeneracy factors for meson and baryon respectively, and M_T their transverse mass. $A_T = \pi\rho_0^2$ is the transverse area of the parton system at freeze-out and τ the hadronization time. Here, we also introduced the shorthand $k_N(p_T) = K_1\left[\frac{\cosh\eta_T}{T}\sum_{a=1}^{N}\sqrt{m_a^2+\frac{p_T^2}{N^2}}\right]$.

The spectrum for hadrons from fragmentation is given by

$$E\frac{dN_h}{d^3p_T} = \sum_a \int_0^1 \frac{dz}{z^2} D_a^h(z,Q^2) E_a \frac{dN_a^{\text{hard}}}{d^3p_{a,T}} \tag{7.14}$$

with $D_a^h(z,Q^2)$ denoting the fragmentation function of a parton a into a hadron h. We use KKP fragmentation functions [137].

It has been shown [132–134] that with appropriately chosen parameters, this two component model accounts successfully for the baryon-to-meson enhancement observed in a large class of RHIC data on Au+Au collisions at intermediate p_T. In particular, recombination models can reproduce the proton to pion and kaon to pion ratio at intermediate transverse momentum [132–134]. Recombination dominates at RHIC up to $p_T^{\text{hadron}} \simeq 4-6$ GeV, and fragmentation takes over for higher transverse momentum.

This model has been extrapolated to the LHC, where two lead nuclei will be collided at the center-of-mass energy $\sqrt{s} = 5.5$ TeV [134,138]. The temperature of the quark phase was fixed at hadronization at 175 MeV, similarly to the RHIC case the parameters υ_T and τA_T have been rescaled such that the results of fluid simulations [139] are reproduced: $\upsilon_T = 0.68$ and $\tau A_T = 11.5\times10^3$ fm^3 [134]. The quenching of high-p_T partons is fixed by the choice $\epsilon_0 = 2.5$, which amounts to a factor $\simeq 10$ suppression of the single inclusive hadron spectra at $p_T = 10$ GeV. The single inclusive hadron spectra calculated for LHC are dominated by recombination up to a scale which lies $\simeq 2$ GeV higher than the corresponding scale at RHIC [134, 138].

7.6 Hadronic composition of jets produced in heavy ion collision at LHC

The change of jet hadrochemistry resulting from the modification of the fragmentation pattern via enhancing the splitting rate according to Eqs. (7.6)–(7.9) can be studied directly using the formula (7.5). In what follows we adopt the choice $f_{\text{med}} = 1$ for this only parameter characterizing the medium. This value clearly lies in the right order of magnitude given the fact that the choice $f_{\text{med}} = 0.6-0.8$ was compatible with R_{AA} measured at RHIC [121]. This choice should be also regarded as an estimate for the LHC that, in the absence of other constraints, is fair enough for our illustrative purposes.

The effect of the medium modification of the partonic cascade for the case of identified hadron spectra is seen in Fig. 7.5. The modified spectra are softened and the hierarchy of the intra-jet distributions is preserved, *i.e.* the peak position moves towards smaller values of ξ (larger values of momenta) with increasing the hadron mass.

Let us now investigate how the change observed in Fig. 7.5 influences the ratios of identified hadron yields. For that purpose, we translate the ξ-dependence at fixed E_{jet} into a transverse momentum

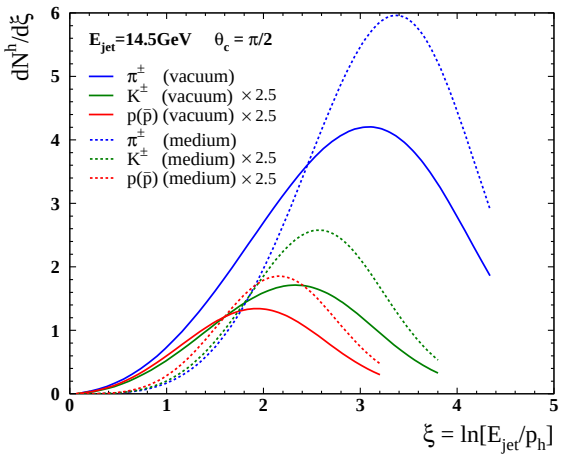

Figure 7.5: The modification of the pion, kaon and proton spectra in the jet of energy $E_{\rm jet} = 14.5$ GeV and opening angle $\theta_c = \pi/2$ expected in our approach with $f_{\rm med} = 1$.

dependence. For a single jet of energy $E_{\rm jet}$, the p_T-spectrum of identified hadron of type h, collected within the opening angle θ_c, takes the form

$$\left[\frac{dN^h(\theta_c)}{dp_T}\right]_{\rm jet} = K_{\rm LPHD}\,\gamma_h\,K_0(M_h)\,\frac{p_T}{p_T^2+M_h^2}\,D^{\rm lim}\Big(\bar{\zeta}(p_T,M_h,E_{\rm jet}),E_{\rm jet},\theta_c,\Lambda\Big). \qquad (7.15)$$

We choose $\gamma_h = 1$ for pions and protons, and $\gamma_K = 0.73$ for kaons [106], which are the same choices as those made in Section 7.3. The limiting spectrum was calculated with $\Lambda \approx M_\pi = 155$ MeV. For the local parton-hadron duality parameter, we took $K_{\rm LPHD} = 0.5$. This factor must be slightly lower than the one used in Fig. 7.2, since it determines the normalization of the identified hadron spectra, while Fig. 7.2 shows the spectrum of all charged particles. The prefactor $K_0(M_h)$ itself depends on $f_{\rm med}$ according to Eq. (7.2). We have checked, however, that it changes only mildly for protons ($\sim 5\%$) and for kaons ($\sim 12\%$). By definition K_0 does not change for the case of pions, which in our approach are described by the limitting spectrum. In the following, we shall focus on results for the opening angle $\theta_c = 0.28$ rad although, in principle, the calculations can be carried out for any value of θ_c, as discussed in Section 7.2. We have tested that the dependence on the opening angle Θ_c is, in fact, very weak .

One of the main results of our study is shown in Fig. 7.6. We observe that in our model the hadrochemical composition of jet fragments changes significantly in the presence of parton energy loss (*i.e.* for finite $f_{\rm med}$). Heavier hadrons become more abundant. For instance, for the case of jets with $E_{\rm jet} = 50$ GeV, the kaon to pion ratio increases by $\sim 50\%$, the proton to pion ratio by $\sim 100\%$. These medium-induced changes persist over the entire transverse momentum range. They decrease slightly with the increase of jet energy but remain clearly visible even for the $E_{\rm jet} = 200$ GeV jets.

Let us stress once more that the significant medium modification of jet hadrochemistry manifested in Fig. 7.6 comes solely form the modification of the probability of parton splitting. In our approach, we have not changed the process of hadronization. Besides, other effects that could be present at the partonic level were not included in our analysis like for instance the transfer of quantum numbers. Therefore, since the enhanced parton splitting alone is capable of changing the jet hadronic composition one expects that measuring the identified hadron jet spectra provides an additional and important handle to study the phenomenon of jet quenching.

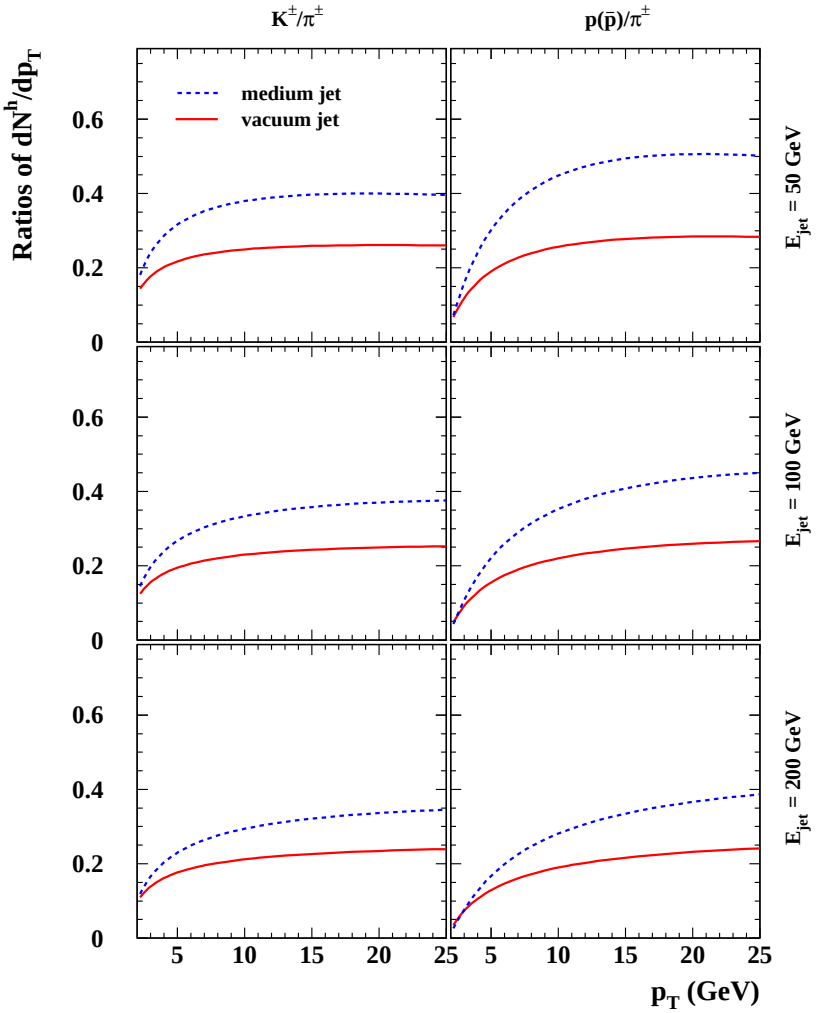

Figure 7.6: Results of our calculations for $K^{\pm}/\pi^{\pm}$ and $p(\bar{p})/\pi^{\pm}$ ratios in the vacuum and medium modified jets with energies $E_{\rm jet} = 50$, 100 and 200 GeV and opening angle $\theta_c = 0.28$.

We have also investigated whether medium effects generally enhance the yield of heavier hadrons, as seen in Fig. 7.6, or whether the opposite may be possible. It is difficult to answer this question strictly and in general. Let us notice, however, by looking at Fig. 7.5, that there is always such region of ξ in which the medium modified spectrum of the heavier hadron is enhanced with respect to the vacuum case whereas the medium modified spectrum of the lighter hadron is depleted. Specifically, in the range $1.5 < \xi < 2.5$ the pion yield decreases with increasing $f_{\rm med}$ for $\xi < 2.5$, while the proton yield increases for $\xi > 1.5$. This opposite $f_{\rm med}$-dependence at intermediate ξ excludes the possibility that the ratios $K^{\pm}/\pi^{\pm}$ and $p(\bar{p})/\pi^{\pm}$ decrease over the entire transverse momentum range with increasing medium-effects. This gives support to the idea that the enhancement of heavier hadrons, observed in Fig. 7.6, is rather generic for jet quenching models.

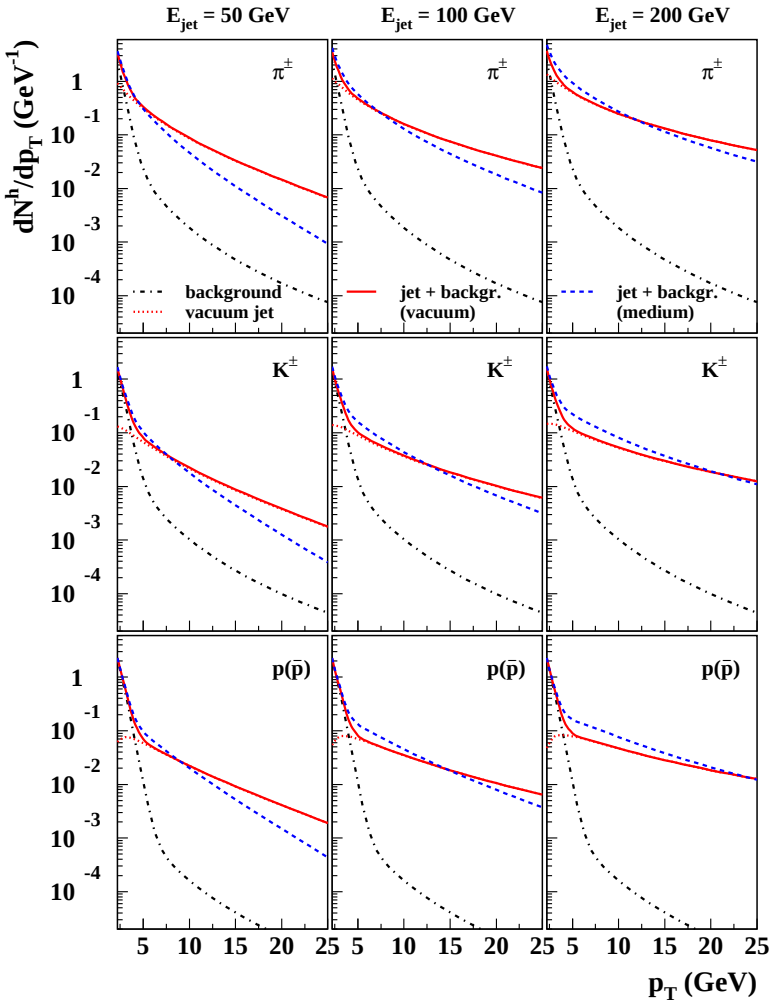

Figure 7.7: Identified transverse momentum spectra within a cone of opening angle $\theta_c = 0.28$ for pions, kaons and protons.

7.7 Hadronic composition of jets within high multiplicity background

In the realistic event of the heavy ions collision the highly energetic jet will sit on the top of the background. In order to see to what extent this background may obscure the effects discussed in the previous section we must determine its yield within the cone of opening angle θ_c. Using the result for the double differential spectrum for mesons and baryons $dN_{M,B}/d^2p_T\,dy|_{y=0}$ from Section 7.5 we integrate it over one unit in rapidity and the full azimuthal phase space. In the $\Delta y \times \Delta\phi$-space, this is an area of 2π. We subsequently have multiplied our result by the fraction $\pi\theta_c^2/2\pi$, which a cone of opening angle θ_c occupies in this plane. Since the spectrum is flat around mid-rapidity, the phase-space integral is trivial and we obtain

$$\left[\frac{dN^h(\theta_c)}{dp_T}\right]_{\text{background}} \simeq \theta_c^2\,\pi\,p_T\,\frac{dN^h}{d^2p_T\,dy}\bigg|_{y=0}. \tag{7.16}$$

In Fig. 7.7, we compare the above background yield in the cone of opening angle $\theta_c = 0.28$ rad

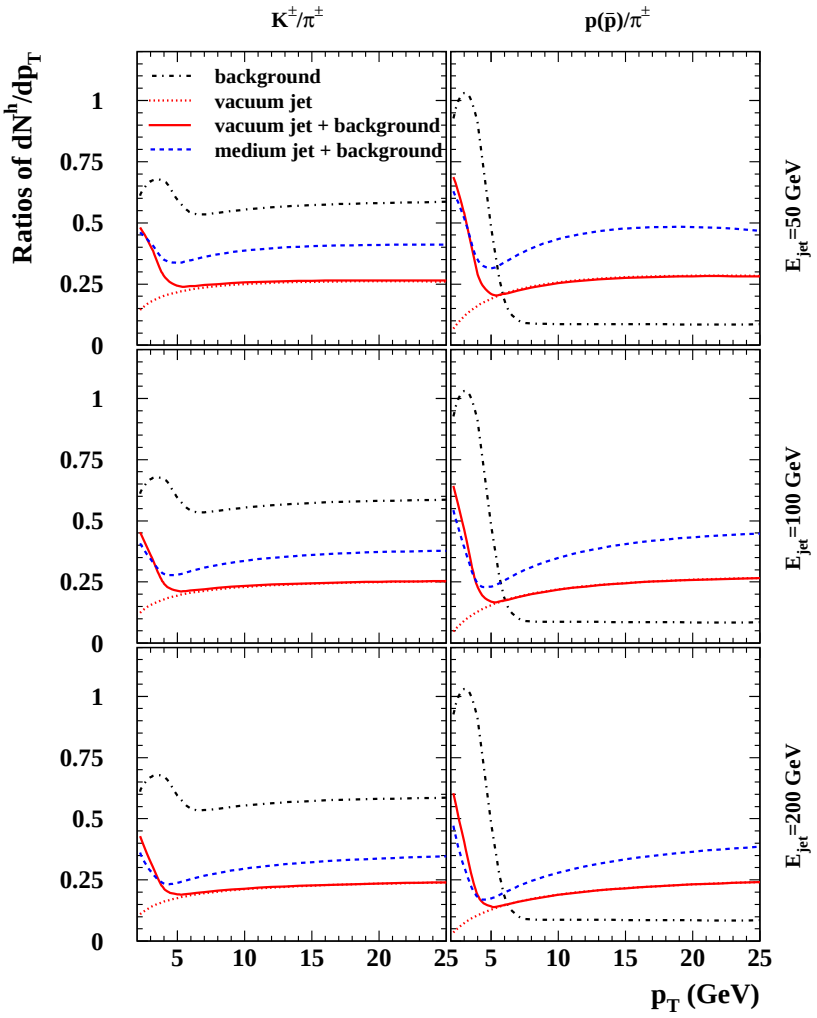

Figure 7.8: The particle ratios $K^{\pm}/\pi^{\pm}$ and $p(\bar{p})/\pi^{\pm}$ obtained from the spectra shown in Fig. 7.7. These ratios are measured in a cone of opening angle $\theta_c = 0.28$ in the $\Delta y \times \Delta\phi$-plane, which contains both soft background and a jet of energy $E_{\rm jet}$.

with the spectrum of hadrons from the vacuum jet given in Eq. (7.15). We observe that this two spectra differ significantly and the harder distribution of jet fragments dominates rapidly over the distribution of the background particles at transverse momenta larger than $5-7$ GeV. Consequently, if one adds the two contributions one obtains the total yield of particles entering the cone with the opening angle θ_c. As we see in Fig. 7.7, in the high-p_T region, the slope of this combined transverse momentum spectrum is entirely dominated by jet fragments. This slope steepens in the presence of medium-induced parton energy loss. Hence, if the energy of a jet can be measured reliably in heavy ion collisions, then such transverse momentum spectra provide direct experimental access to the longitudinal jet fragmentation function without the necessity to subtract the background.

In Fig. 7.8, we have plotted the identified particle ratios $K^{\pm}/\pi^{\pm}$ and $p(\bar{p})/\pi^{\pm}$, in the cone of opening angle $\theta_c = 0.28$ rad. The measurement of such ratios should be much easier and more direct than the measurement of the ratios in pure jets discussed in the previous section and depicted in Fig. 7.6. This is because here it suffices to count all particles within the cone with the opening angle θ_c

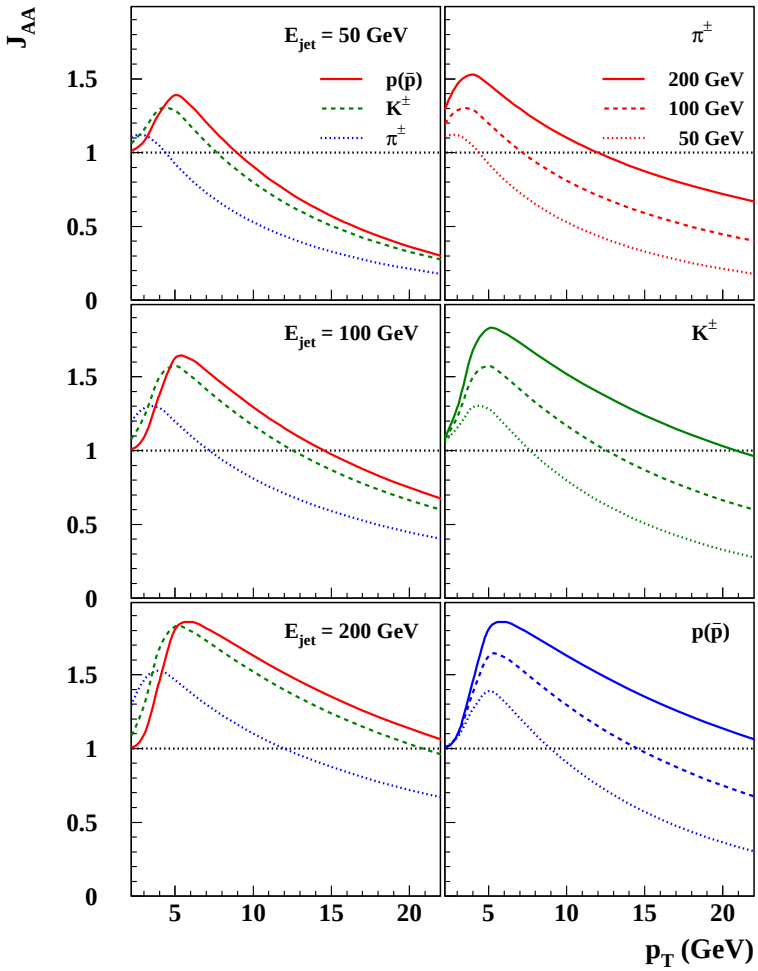

Figure 7.9: The jet modification factor J_{AA}, defined in (7.17) within the cone of opening angle $\theta_c = 0.28$ as a function of transverse momentum for different jet energies and different hadron species.

as a function of p_T without separating those hadrons which come from the jet and those that belong to the background. Let us also notice that the determination of E_{jet} does not need to be particularly good, since the hadronic ratios shown in Fig. 7.8 depend weakly on E_{jet}. Since above $p_T > 5-7$ GeV the spectra within the cone are essentially background free, also the particle ratios above this values of transverse momenta match those shown in Fig. 7.6. which were calculated for pure jets.

It is worth noticing that in this high-p_T range, medium-effects enhance the particle ratios, which for the case of the protons means that they become even more distinct than those of the background. As depicted in Fig. 7.8, at lower transverse momentum, the background yield dominates the hadronic abundances and particle ratios.

The complementary way of presenting information about the hadrochemical composition of jets and their change in a medium is by forming another type of ratio

$$J_{AA} \equiv \frac{\left.\frac{dN^h}{dp_T}\right|_{\text{med}}}{\left.\frac{dN^h}{dp_T}\right|_{\text{vac}}}, \tag{7.17}$$

which we will call the jet modification factor, in analogy with the nuclear modification factor. Here, we have the same hadron species in the numerator and in the denominator. In both cases they are calculated as a sum of the jet (7.15) an the background (7.16) particles entering the cone θ_c. The numerator corresponds, however, to the quenched jet ($f_{\rm med} = 1$) whereas the denominator to the vacuum jet ($f_{\rm med} = 0$). As we have seen several times already, and in particular in Fig. 7.5, jet quenching amounts to the reshuffling of hadronic yield from high to low transverse momentum. This is reflected also in the behavior of the jet modification factor depicted in Fig. 7.9. Above a certain value of the transverse momentum $p_T^{\rm crit}$, at which $J_{AA}(p_T^{\rm crit}) = 1$, the yield of particles in the medium modified jet is depleted with respect to the vacuum case. At the same time the subleading fragments, additionally produced due to the medium, populate the region below $p_T^{\rm crit}$ and therefore enhance J_{AA}. As manifested in Fig. 7.9, the value of $p_T^{\rm crit}$ varies significantly both with the jet energy and with hadron species. In particular, since the total amount of additional multiplicity, produced due to parton energy loss, increases with the jet energy also J_{AA} increases with $E_{\rm jet}$. Similarly, the order of the particle species dependence of J_{AA}, seen in the left column of Fig. 7.9, is a direct consequence of the medium-induced enhancement of the ratios $K^{\pm}/\pi^{\pm}$ and $p\,(\bar{p})/\pi^{\pm}$ from Figs. 7.6 and 7.8. Namely, if for instance at fixed transverse momentum, $\langle K^{\pm}\rangle_{\rm med}/\langle\pi^{\pm}\rangle_{\rm med} > \langle K^{\pm}\rangle_{\rm vac}/\langle\pi^{\pm}\rangle_{\rm vac}$, then $\langle K^{\pm}\rangle_{\rm med}/\langle K^{\pm}\rangle_{\rm vac} > \langle\pi^{\pm}\rangle_{\rm med}/\langle\pi^{\pm}\rangle_{\rm vac}$, and this order is reflected in Fig. 7.9.

7.8 Concluding remarks

We have analyzed the phenomenon of jet quenching in heavy ion collisions at the LHC. Specifically, we studied change of the hadronic composition of jets due to interactions with the QCD medium. In order to describe the development of the partonic cascade, we used the framework of MLLA. Together with this formalism the hypothesis of LPHD was employed as a simple hadronization model. The interaction of the jet with the medium was assumed in the form of radiative energy loss. It was implemented, following the model proposed in [121], by enhancing the singular parts of the splitting functions.

We observe that the modification of the partonic cascade alone, without changing the process of hadronization, is capable to significantly affect the hadrochemical composition of jets. Our main prediction for the LHC concerns the rations $K^{\pm}/\pi^{\pm}$ and $p(\bar{p})/\pi^{\pm}$, which, according to our analysis, increase if the jet is modified by the medium. We give arguments why this is likely to be a generic feature for a wide class of jet quenching models.

We have also checked whether this effect persists when the jet is not separated from the abundant underlying event particles. Using the prediction of the LHC background from [132, 133] we calculated the background yield inside the jet cone and added it to the MLLA+LPHD jets spectra. We observe that above the transverse momentum $p_T = 5 - 7$ GeV the slope of such combined distributions is entirely dominated by the slope of the jet spectrum. Moreover, this slope steepens in the presence of a medium. Finally, we have shown that the increase of $K^{\pm}/\pi^{\pm}$ and $p(\bar{p})/\pi^{\pm}$ ratios due to the medium modification, found for the case of pure jets, is not obscured in the presence of the background. This results from the characteristically different hadrochemistry of the jet and the underlying event. For the case of $p(\bar{p})/\pi^{\pm}$ ratios the medium modification leads to further increase of the difference in hadrochemistry between the jet and the background. On the other hand, any jet quenching mechanism which kicks components of the background into the jet cone may be expected to have the opposite effect. Therefore, the results of our study can also be viewed as a baseline, on top of which effects indicative of specific microscopic mechanisms of parton energy loss may be established.

The identified hadron spectra inside the jets created in heavy ion collisions as well as their ratios predicted from our study differ significantly from those observed in the vacuum case. This conclusion remains valid also if the jets are not separated from the background. The ALICE collaboration has

an extensive program devoted to the measurement of the intra-jet distributions of identified hadrons. Therefore, we expect that, in the near future, the set of predictions concerning the medium-modified jets, which we have presented in this chapter, will be able to be tested against the experimental data from the LHC.

Chapter 8

Summary

In this Thesis we have presented theoretical study of two important processes, which are experimentally investigated in the collisions of particles at high center-of-mass energy. The first process, discussed in Chapters 1–5, was deep inelastic electron-proton scattering, for which a large abundance of data from the experiments at HERA is available. We focused, in particular, on the phenomenological and theoretical study of the phenomenon of saturation. The second process, examined in Chapter 6 and 7, was the production of jets and their modification in the heavy ion collisions at the LHC.

The phenomenological analysis of saturation, documented in Chapter 3, was performed in the framework of the model of Bartels, Golec-Biernat and Kowalski [49]. This is an extension of the Golec-Biernat and Wüsthoff model [47], which was improved by including the proper DGLAP evolution of the gluon density at large virtuality scales. Such improvement modifies slightly the behavior of the dipole cross section at small values of dipole size and allows for better description of the proton structure function $F_2(x, Q^2)$ at large photon virtuality Q^2. We studied the production of the charm and beauty flavors within the BGK model [49]. The five model parameters were set by the fit to the recent data for the proton structure $F_2(x, Q^2)$ at low x. We assumed the light quarks to be massless. We found the values of $\chi^2/\text{ndf} = 1.06 - 1.16$, which is close to unity and enables us to conclude that the quality of the fit is good. Consequently, the model fitted with heavy quarks correctly describes the inclusive proton structure function. We observe that the parameters of the model differ significantly from those obtained in [49], in the fit without heavy quarks. Also, the the dipole cross section is changed. Adding the heavy quarks cures its pathological behavior found in [49] for the case of fit with massless light quarks. Comparing our result for the dipole cross section with the result from [49], obtained in the fit with the massive light quarks, we see that the fit with heavy quarks leads to the shift of the dipole cross section towards smaller values of the dipole size. This has a consequence on the position of the critical line which moves in the direction of smaller values of Q^2 making the saturation more difficult to observe in the future experiments. This last finding agrees with the result obtained in a different saturation model [56] by Soyez [69]. In addition, we were able to predict the charm and beauty contributions to the proton structure function. We found very good agreement of our results for $F_2^{c\bar{c}}$ and $F_2^{b\bar{b}}$ with the data from H1 and ZEUS collaborations. Although this was not discussed extensively in the Thesis, let us mention that also the predictions for the diffractive structure function agree well with the data. Finally, the longitudinal structure function F_L has been predicted and compared with the H1 estimations. The large experimental errors, however, disable from making a firm conclusion. Fortunately, the direct measurement of F_L, should be available in the near future.

The theoretical study of the saturation effects was presented in Chapter 5. For that purpose, the BK equation with running coupling and the improved NLL BFKL kernel was used. As a method of solving the equation for asymptotic energies, we adopted the traveling waves approach. This approach, known since long ago in statistical physics, allows to obtain the solutions of a certain class of nonlinear equations by analyzing solely their linear part. The existence of the traveling wave solution, in terms

of QCD, is equivalent to the property of geometric scaling. We found that the parts of the equation that are generated by the NLL corrections to the BFKL kernel do not contribute to the first two universal terms in the asymptotic result for the saturation scale. In other words, the functional form of this solutions is the same as in the case of the LL BK equation with running coupling studied in [76]. The NLL result depends, however, parametrically on the resummation scheme used for the BFKL kernel. We studied our results with the kernels resummed in three three specific schemes S3, S4 and CCS. The first two depend explicitly on $\bar{\alpha}_s$ and the value of the coupling influences the critical parameters which enter the expressions for the amplitude and the saturation scale. In contrast, the third scheme is independent of $\bar{\alpha}_s$ and therefore the results obtained within this scheme are identical with those found at the leading order [76]. Finally, we found that although our results are, strictly speaking, valid for asymptotic values of Y, we are able to mimic the non-asymptotic behavior for the saturation scale from [90]. This can be achieved by choosing an appropriate value of Y_0, which is an arbitrary parameter in our approach. The non-zero value of Y_0 generates and parametrizes the higher order, non-universal corrections, which are relevant at phenomenological rapidities. This is true, in particular, for the energy of the HERA collider.

In Chapter 7 we turned to the study of jets. We analyzed the case in which they develop in the dense QCD medium. Such jets are modified with respect to those created in the vacuum, which can be used to study medium properties. A number of signatures that may be left on jets created in the heavy ion collisions have been explored so far. In Chapter 7 we investigate a new possibility to study jet modification, namely by looking at the change of its hadronic content. We analyzed the single particle spectra of identified hadrons. To obtain these quantities, we used the perturbative framework of MLLA supplemented by the hypothesis of LPHD. This formalism is known to successfully describe jets in e^+e^-, $pp/p\bar{p}$ and ep collisions. Moreover, it was particularly convenient since the available analytic results allow for easy implementation of the medium induced energy loss. More specifically, this interaction of the jet with the medium was introduced, following the model proposed in [121], by enhancing the singular parts of the splitting functions. As shown in [121], this is sufficient to account for the suppression of the high-momentum particles at RHIC. We predict for the LHC that the rations $K^{\pm}/\pi^{\pm}$ and $p(\bar{p})/\pi^{\pm}$, significantly increase if the jet is modified by the medium. We argue that this feature should be more general and remain valid for a large class of the radiative energy loss models. The significant change of hadrochemistry that we observe was obtained only by the modification of the partonic cascade, without changing the process of hadronization. Therefore, we view the study of jet hadrochemistry as a source of valuable information concerning the microscopic mechanism underlying jet quenching. We checked that due to the characteristically different hadrochemistry of the jet and the underlying event the effects predicted for pure jets persist even if the jets are not separated from the high-multiplicity environment of the heavy ion collision. To estimate the underlying event at LHC we used the result form [132, 133] and calculated the background yield inside the jet cone. The ALICE experiment, which will soon start operating, has an extensive program of measuring the identified particle distribution. Therefore one, will be able to confront our predictions with data in the near future.

Acknowledgments

In the first place, I would like to thank my supervisor, Krzysztof Golec-Biernat, for his continuous support during the period of my PhD. His enthusiasm and readiness to discuss, which I consider simply invaluable, allowed me to gain or improve understanding of various aspect of Quantum Chromodynamics. Our common work led to the results documented in the Chapter 3 of this Thesis. I am also grateful to him for careful reading of the manuscript and for many valuable remarks.

I am likewise obliged to my two other collaborators, Robert Peschanski and Urs Wiedemann, with whom I have obtained the results reported on in Chapters 5 and 7, respectively.

I am indebted to prof. Andrzej Białas for his guidance during my first projects related to the theoretical description of particle collisions at high energies. I am also grateful for his supervision at the beginning of my PhD as well as for many interesting discussions afterwards.

The quality of the results presented in this Thesis was greatly improved by the discussions with Nicolas Borghini, Yuri Dokshitzer, Andreas Morsch, Stehphane Munier, Karel Safarik, Jürgen Schukraft, and Yves Schutz. I wish also to thank Steffen Bass, Rainer Fries and Carlos Salgado for sharing the estimations of the underlying event expected in the Pb-Pb collisions at the LHC.

Over the years of my PhD I took part in many enriching discussions with Adam Bzdak, Jakub Jedrak, Krzysztof Fiałkowski, Cyrille Marquet, Leszek Motyka, Michał Praszałowicz, Christophe Royon, Andrzej Siódmok, Dionysis Triantafyllopoulos, Laurent Schoeffel and Jacek Wosiek.

I wish also to thank the Theory Group at the Institute of Physics at Jagiellonian University for providing me nice and comfortable environment to work and study.

Part of the work which constitutes this Thesis was obtained during my visit to the Institute of Nuclear Physics in Cracow, École Polytechnique in Palaiseau and Institut de Physique Théorique in Saclay. I acknowledge the hospitality of these institutions.

I feel gratitude to the members of the CERN Theory Group for their hospitality at the time of my one-year stay at CERN. I wish to thank Urs Wiedemann for his supervision during this period. I acknowledge the support of the Marie Curie Early Stage Research Training Fellowship of the European Community's Sixth Framework Programme under contract number (MEST-CT-2005-020238), which made the stay at CERN possible.

I would like to thank my family and in particular my wife Joanna for all.

This research has been supported by the grants: No. 1 P03B 028 28 (2005-08), No. N202 048 31/2647 (2006-08) and by the French–Polish scientific agreement Polonium.

Appendix A

Mellin transform and its properties

The Mellin transform and its inverse are defined as follows

$$\tilde{f}(\omega) = \int_0^\infty dt\, t^{\omega-1} f(t), \tag{A.1}$$

$$f(t) = \int_{c-i\infty}^{c+i\infty} \frac{d\omega}{2\pi i} t^{-\omega} \tilde{f}(\omega), \tag{A.2}$$

where $a < c < b$. The limits a and b are specified by the so called *fundamental strip* that is the area in the plane of complex ω in which the Mellin transform exists. In other words, $\tilde{f}(\omega)$ has no singularities if $a < \mathrm{Re}\{\omega\} < c$. The Mellin transform (A.1) of the function $f(t)$ is equivalent to the two-sided Laplace transform of $f(e^{-t})$.

In this Thesis we exploit in several places the transform of the Heaviside step function $\Theta(a-t)$

$$\int_0^\infty dt\, t^{\omega-1} \Theta(a-t) = \frac{a^\omega}{\omega}. \tag{A.3}$$

The above integral converges for $\omega \in (0, \infty)$. In fact, very often in practical applications, the fundamental strip stretches from ω_0 to $+\infty$, where ω_0 is the rightmost singularity of $\tilde{f}(\omega)$. In that case, the condition for c is $c > \omega_0$.

Interestingly enough, the functions of the Bjorken variable x vanish, by definition, for $x > 1$. In such case, the Mellin transform boils down to

$$\tilde{f}(\omega) = \int_0^1 dt\, x^{\omega-1} f(x), \tag{A.4}$$

with the fundamental strip (ω_0, ∞). It is straightforward to check that this is equivalent to the one-sided Laplace transform of $f(e^{-x})$.

An important property of the Mellin transform is the algebraization of the following convolution

$$\int_0^1 dx\, x^{\omega-1} \left[\int_x^1 \frac{dz}{z} A\Big(\frac{x}{z}\Big) B(z) \right] = \int_0^1 dx\, x^{\omega-1} \left[\int_x^1 \frac{dz}{z} A(z) B\Big(\frac{x}{z}\Big) \right] = \tilde{A}(\omega)\tilde{B}(\omega), \tag{A.5}$$

where we assume that the functions $A(x)$ and $B(x)$ vanish for $x > 1$. This relation is used for instance in Section 1.5.2 to find the solution of the DGLAP equation in the limit of small x as well as in Section 3.5 to obtain the gluon density in the DGLAP improved saturation model.

Appendix B

"NLL" part of the BK equation with the NLL BFKL kernel

After substituting the Ansatz (4.16), with $u \equiv \mathcal{N}$, into Eq. (5.24), setting $k = \frac{1}{3}$, $\alpha = \frac{1}{3}$ and keeping only the terms $\mathcal{O}(t^{-\frac{1}{3}})$, which are leading in the limit of large t, one arrives at the following equation

$$G(z)\gamma_c \upsilon_g (z - 4\beta) t^{-\frac{1}{3}} = \frac{1}{b}\chi'' G''(z) t^{-\frac{1}{3}} + \frac{2}{b} e^{\gamma_c z\, t^{1/3}} \cdot \Upsilon(G(z), G(z)', G(z)'', z, t), \qquad \text{(B.1)}$$

where by $\Upsilon(G(z), G(z)', G(z)'', z, t)$ we denoted terms of the order $\mathcal{O}(t^{-\frac{1}{3}})$ from the "NLL" part of Eq. (5.24)

$$\text{"NLL"} = \Big\{ \frac{1}{2t}\,\dot{\chi}(\gamma_c)\,\partial_t - \frac{1}{2t}\,\dot{\chi}'(\gamma_c)\,\partial_L \partial_t - \frac{1}{2t}\,\dot{\chi}'(\gamma_c)\,\gamma_c \partial_t + \frac{1}{8t^2}\,\ddot{\chi}(\gamma_c)\,(\partial_t^2 - \frac{1}{t}\,\partial_t) \Big\} \mathcal{N}(L, t). \qquad \text{(B.2)}$$

The derivatives which appear in the above expression can be easily calculated and are given by

$$\begin{aligned}
\partial_t \mathcal{N} &= e^{-\gamma_c z\, t^{1/3}} \Big\{ G(z) \Big[\frac{1}{3} t^{-\frac{2}{3}} + \upsilon_g \gamma_c t^{\frac{1}{3}} - \beta \gamma_c t^{-\frac{1}{3}} \Big] + G'(z) \Big[-\frac{1}{3} z t^{-\frac{2}{3}} - \upsilon_g + \beta t^{-\frac{2}{3}} \Big] \Big\}, \\
\partial_t^2 \mathcal{N} &= e^{-\gamma_c z\, t^{1/3}} \Big\{ G(z) \Big[-\frac{2}{9} t^{-\frac{5}{3}} + \frac{2}{3} \upsilon_g \gamma_c t^{-\frac{2}{3}} - \frac{2}{3} \beta \gamma_c t^{-\frac{4}{3}} + \upsilon_g^2 \gamma_c^2 t^{\frac{1}{3}} - \\
&\qquad 2\upsilon_g \beta \gamma_c^2 t^{-\frac{1}{3}} + \beta^2 \gamma_c^2 t^{-1} + \frac{2}{3} \beta \gamma_c t^{-\frac{4}{3}} \Big] + \\
&\qquad G'(z) \Big[\frac{2}{9} z t^{-\frac{5}{3}} - \frac{2}{3} z \upsilon_g \gamma_c t^{-\frac{2}{3}} + \frac{2}{3} z \beta \gamma_c t^{-\frac{4}{3}} - 2\upsilon_g^2 \gamma_c + \\
&\qquad 4\upsilon_g \beta \gamma_c t^{-\frac{2}{3}} - 2\beta^2 \gamma_c t^{-\frac{4}{3}} - \frac{2}{3} \beta t^{-\frac{5}{3}} \Big] + \\
&\qquad G''(z) \Big[\frac{1}{9} z^2 t^{-\frac{5}{3}} - \frac{2}{3} z \beta t^{-\frac{5}{3}} + \frac{2}{3} z \upsilon_g t^{-1} + \beta^2 t^{-\frac{5}{3}} - 2\beta \upsilon_g t^{-1} + \upsilon_g^2 t^{-\frac{1}{3}} \Big] \Big\}, \\
\partial_L \partial_t \mathcal{N} &= e^{-\gamma_c z\, t^{1/3}} \Big\{ G(z) \Big[-\frac{1}{3} \gamma_c t^{-\frac{2}{3}} - \upsilon_g \gamma_c^2 t^{\frac{1}{3}} + \beta \gamma_c^2 t^{-\frac{1}{3}} \Big] + \\
&\qquad G'(z) \Big[\frac{1}{3} z \gamma_c t^{-\frac{2}{3}} + 2\upsilon_g \gamma_c - 2\gamma_c \beta t^{-\frac{2}{3}} \Big] + \\
&\qquad G''(z) \Big[-\frac{1}{3} z t^{-1} - \upsilon_g t^{-\frac{1}{3}} + \beta t^{-1} \Big] \Big\}. \qquad \text{(B.3)}
\end{aligned}$$

Extracting the terms which dominate for large t gives

$$\begin{aligned}
\partial_t \mathcal{N} &= e^{-\gamma_c z\, t^{1/3}} G(z)\, v_g \gamma_c t^{\frac{1}{3}} + \mathcal{O}(t^{-\frac{1}{3}}), \\
\partial_t^2 \mathcal{N} &= e^{-\gamma_c z\, t^{1/3}} G(z)\, v_g^2 \gamma_c^2 t^{\frac{1}{3}} + \mathcal{O}(t^{-\frac{1}{3}}), \\
\partial_L\, \partial_t \mathcal{N} &= -e^{-\gamma_c z\, t^{1/3}} G(z)\, v_g \gamma_c^2 t^{\frac{1}{3}} + \mathcal{O}(t^{-\frac{1}{3}}).
\end{aligned} \tag{B.4}$$

We see that the leading terms of of the derivatives are of the order $\mathcal{O}(t^{\frac{1}{3}})$. However, each derivative in (B.2) is suppressed either by t^{-1} or t^{-2} . Therefore, the "NLL" term contributes only at the order $\mathcal{O}(t^{-\frac{2}{3}})$ and this is why the solutions of the BK equation with the LL and NLL kernel have the same functional form.

Appendix C

Particle identified hadron spectra in MLLA

In the case of ultra high energies ζ defined in Eq. (6.58) can be interpreted as the normalized rapidity. However, for the presently available energies the normalized rapidity should be defined rather as

$$\bar{\zeta} = \frac{y}{y_{\text{max}}}, \qquad y = \ln \frac{E_h + p_h}{M_h}, \qquad y_{\text{max}} = \ln \frac{E_{\text{jet}} + p_{\text{max}}}{M_h}, \tag{C.1}$$

where E_h is the hadron energy and p_h its momentum. The variable ξ, which appears in the result (6.57), is defined as $\xi = \ln(E_{\text{jet}}/E_h)$. It is straightforward to show using the definition (C.1) that

$$E_h = M_h \cosh y, \tag{C.2}$$

$$E_{\text{jet}} = M_h \cosh y_{\text{max}}. \tag{C.3}$$

Hence, we have

$$\xi = \ln \frac{E_{\text{jet}}}{E} = \ln \frac{\cosh y_{\text{max}}}{\cosh y} = \ln \frac{\cosh y_{\text{max}}}{\cosh\left(\bar{\zeta} y_{\text{max}}\right)}, \tag{C.4}$$

and substituting the above into the definition of ξ from Eq. (6.58) gives the relation between the two normalized rapidities

$$\begin{aligned} \zeta &= 1 - \frac{\xi}{Y(\theta_c)} \\ &= 1 - \frac{\xi}{Y(\theta_c)} \ln \frac{\cosh y_{\text{max}}}{\cosh\left(\bar{\zeta}\, y_{\text{max}}\right)}. \end{aligned} \tag{C.5}$$

This is the result given in Eq. (7.4) which we exploit in Chapter 7.

The rapidity y and its maximal value y_{max} can be expressed explicitly for a given hadron h in terms of the variable $x_p = p_h/E_{\text{jet}}$

$$y = \ln \frac{E + p_h}{M_h} = \ln \frac{p_h + \sqrt{p_h^2 + M_h^2}}{M_h} = \ln \left\{ x_p + \sqrt{x_p^2 + \left(\frac{M_h}{E_{\text{jet}}}\right)^2} \right\} + \ln \frac{E_{\text{jet}}}{M_h}, \tag{C.6}$$

$$y_{\text{max}} = \ln \frac{E_{\text{jet}} + \sqrt{E_{\text{jet}}^2 - M_h^2}}{M_h} = \ln \left\{ \frac{E_{\text{jet}}}{M_h} + \sqrt{\left(\frac{E_{\text{jet}}}{M_h}\right)^2 - 1} \right\}. \tag{C.7}$$

The relation (C.5) substituted to the limiting spectrum is taken with $y_{\rm max}^{\rm lim} \equiv y_{\rm max}(M_h = M_\pi = \Lambda)$. This, together with the hypothesis of the local parton-hadron duality, leads to

$$x\frac{dN^h}{dx}(\bar{\zeta}) = K_{\rm LPHD}\, K_0(M_h)\, \gamma_h\, D_G^{\rm lim}\left(\zeta = 1 - \frac{1}{Y(\theta_c)} \ln \frac{\cosh y_{\rm max}^{\rm lim}}{\cosh\left(\bar{\zeta}\, y_{\rm max}^{\rm lim}\right)}\right), \tag{C.8}$$

and after accounting for the difference between $x = E_h/E_{\rm jet}$ and $x_p = p_h/E_{\rm jet}$ we arrive at

$$x_p\frac{dN^h}{dx_p}(\bar{\zeta}) = K_{\rm LPHD}\, K_0(M_h)\, \gamma_h\, \frac{x_p^2}{x_p^2 + \left(\frac{M_h}{E_{\rm jet}}\right)^2}\, D_G^{\rm lim}\left(\zeta = 1 - \frac{1}{Y(\theta_c)} \ln \frac{\cosh y_{\rm max}^{\rm lim}}{\cosh\left(\bar{\zeta}\, y_{\rm max}^{\rm lim}\right)}\right), \tag{C.9}$$

where the Jacobian $x_p^2/(x_p^2 + (M_h/E_{\rm jet}))^2$ comes from changing variables from $x = E_h/E_{\rm jet}$ to $x_p = p_h/E_{\rm jet}$. The redefined normalized rapidity, $\bar{\zeta}$, depends on the hadron momentum fraction x_p, hadron mass M_h and the jet energy $E_{\rm jet}$

$$\bar{\zeta}(x_p, M_h, E_{\rm jet}) = \frac{\ln\left\{x_p + \sqrt{x_p^2 + \left(\frac{M_h}{E_{\rm jet}}\right)^2}\right\} + \ln\frac{E_{\rm jet}}{M_h}}{\ln\left\{\frac{E_{\rm jet}}{M_h} + \sqrt{\left(\frac{E_{\rm jet}}{M_h}\right)^2 - 1}\right\}}. \tag{C.10}$$

Hence, we obtained Eq. (7.5), which is the basic formula for the study presented in Chapter 7.

Bibliography

[1] T. Muta, *Foundations of Quantum Chromodynamics* (World Scientific, 1987).

[2] S. Pokorski, *Gauge Field Theories*, 2nd ed. (Cambridge University Press, 2000).

[3] R. K. Ellis, W. J. Stirling, and B. R. Webber, *QCD and Collider Physics* (Cambridge University Press, 2003).

[4] Y. L. Dokshitzer, V. A. Khoze, A. H. Mueller, and S. I. Troyan, *Basics of Perturbative QCD* (Editions Frontieres, 1991).

[5] K. Golec-Biernat, Habilitation Thesis, Report No 1877/PH (2001).

[6] G. Leibbrandt, Rev. Mod. Phys. **59**, 1067 (1987).

[7] G. Altarelli and G. Parisi, Nucl. Phys. **B126**, 298 (1977).

[8] G. Curci, W. Furmanski, and R. Petronzio, Nucl. Phys. **B175**, 27 (1980).

[9] W. Furmanski and R. Petronzio, Phys. Lett. **B97**, 437 (1980).

[10] S. Moch, J. A. M. Vermaseren, and A. Vogt, Nucl. Phys. **B688**, 101 (2004).

[11] A. Vogt, S. Moch, and J. A. M. Vermaseren, Nucl. Phys. **B691**, 129 (2004).

[12] J. Collins, D. Soper, and G. Sterman, *Factorization of hard processes in QCD, In: A. H. Mueller (Ed.) Perturbative quantum chromodynamics* (World Scientific, 1989).

[13] V. N. Gribov and L. N. Lipatov, Sov. J. Nucl. Phys. **15**, 438 (1972).

[14] L. N. Lipatov, Sov. J. Nucl. Phys. **20**, 94 (1975).

[15] Y. L. Dokshitzer, Sov. Phys. JETP **46**, 641 (1977).

[16] A. D. Martin, W. J. Stirling, R. S. Thorne, and G. Watt, Phys. Lett. **B652**, 292 (2007).

[17] W. K. Tung *et al.*, JHEP **02**, 053 (2007).

[18] A. De Rujula *et al.*, Phys. Rev. **D10**, 1649 (1974).

[19] L. N. Lipatov, Sov. J. Nucl. Phys. **23**, 338 (1976).

[20] E. A. Kuraev, L. N. Lipatov, and V. S. Fadin, Sov. Phys. JETP **45**, 199 (1977).

[21] E. A. Kuraev, L. N. Lipatov, and V. S. Fadin, Sov. Phys. JETP **44**, 443 (1976).

[22] I. I. Balitsky and L. N. Lipatov, Sov. J. Nucl. Phys. **28**, 822 (1978).

[23] J. R. Forshaw and D. A. Ross, *Quantum Chromodynamic and the Pomeron* (Cambridge University Press, 2004).

[24] G. P. Salam, Acta Phys. Polon. **B30**, 3679 (1999).

[25] V. S. Fadin and L. N. Lipatov, Phys. Lett. **B429**, 127 (1998).

[26] M. Ciafaloni and G. Camici, Phys. Lett. **B430**, 349 (1998).

[27] G. P. Salam, JHEP **07**, 019 (1998).

[28] M. Ciafaloni, D. Colferai, and G. P. Salam, Phys. Rev. **D60**, 114036 (1999).

[29] M. Ciafaloni and D. Colferai, Phys. Lett. **B452**, 372 (1999).

[30] B. Andersson, G. Gustafson, and J. Samuelsson, Nucl. Phys. **B467**, 443 (1996).

[31] J. Kwiecinski, A. D. Martin, and P. J. Sutton, Z. Phys. **C71**, 585 (1996).

[32] M. Froissart, Phys. Rev. **123**, 1053 (1961).

[33] A. Martin, Phys. Rev. **129**, 1432 (1963).

[34] L. V. Gribov, E. M. Levin, and M. G. Ryskin, Nucl. Phys. **B188**, 555 (1981).

[35] L. V. Gribov, E. M. Levin, and M. G. Ryskin, Phys. Rept. **100**, 1 (1983).

[36] A. H. Mueller and J.-w. Qiu, Nucl. Phys. **B268**, 427 (1986).

[37] I. Balitsky, Nucl. Phys. **B463**, 99 (1996).

[38] Y. V. Kovchegov, Phys. Rev. **D60**, 034008 (1999).

[39] J. Jalilian-Marian, A. Kovner, A. Leonidov, and H. Weigert, Nucl. Phys. **B504**, 415 (1997).

[40] J. Jalilian-Marian, A. Kovner, A. Leonidov, and H. Weigert, Phys. Rev. **D59**, 014014 (1999).

[41] E. Iancu, A. Leonidov, and L. D. McLerran, Nucl. Phys. **A692**, 583 (2001).

[42] E. Iancu, A. Leonidov, and L. D. McLerran, Phys. Lett. **B510**, 133 (2001).

[43] E. Ferreiro, E. Iancu, A. Leonidov, and L. McLerran, Nucl. Phys. **A703**, 489 (2002).

[44] H. Weigert, Nucl. Phys. **A703**, 823 (2002).

[45] L. D. McLerran and R. Venugopalan, Phys. Rev. **D49**, 2233 (1994).

[46] L. D. McLerran and R. Venugopalan, Phys. Rev. **D49**, 3352 (1994).

[47] K. Golec-Biernat and M. Wusthoff, Phys. Rev. **D59**, 014017 (1999).

[48] K. Golec-Biernat and M. Wusthoff, Phys. Rev. **D60**, 114023 (1999).

[49] J. Bartels, K. Golec-Biernat, and H. Kowalski, Phys. Rev. **D66**, 014001 (2002).

[50] H1, C. Adloff *et al.*, Eur. Phys. J. **C21**, 33 (2001).

[51] ZEUS, S. Chekanov *et al.*, Eur. Phys. J. **C21**, 443 (2001).

[52] ZEUS, J. Breitweg *et al.*, Phys. Lett. **B487**, 53 (2000).

[53] J. R. Forshaw, G. Kerley, and G. Shaw, Phys. Rev. **D60**, 074012 (1999).

[54] J. R. Forshaw, G. R. Kerley, and G. Shaw, Nucl. Phys. **A675**, 80c (2000).

[55] J. R. Forshaw and G. Shaw, JHEP **12**, 052 (2004).

[56] E. Iancu, K. Itakura, and S. Munier, Phys. Lett. **B590**, 199 (2004).

[57] M. McDermott, L. Frankfurt, V. Guzey, and M. Strikman, Eur. Phys. J. **C16**, 641 (2000).

[58] H. Kowalski, L. Motyka, and G. Watt, Phys. Rev. **D74**, 074016 (2006).

[59] J. R. Forshaw, R. Sandapen, and G. Shaw, JHEP **11**, 025 (2006).

[60] H1, C. Adloff *et al.*, Phys. Lett. **B528**, 199 (2002).

[61] H1, A. Aktas *et al.*, Eur. Phys. J. **C40**, 349 (2005).

[62] ZEUS, S. Chekanov *et al.*, Phys. Rev. **D69**, 012004 (2004).

[63] K. J. Golec-Biernat and S. Sapeta, Phys. Rev. **D74**, 054032 (2006).

[64] A. M. Stasto, K. Golec-Biernat, and J. Kwiecinski, Phys. Rev. Lett. **86**, 596 (2001).

[65] C. Marquet and L. Schoeffel, Phys. Lett. **B639**, 471 (2006).

[66] A. D. Martin, R. G. Roberts, W. J. Stirling, and R. S. Thorne, Phys. Lett. **B531**, 216 (2002).

[67] L. Frankfurt, A. Radyushkin, and M. Strikman, Phys. Rev. **D55**, 98 (1997).

[68] A. D. Martin, R. G. Roberts, W. J. Stirling, and R. S. Thorne, Eur. Phys. J. **C14**, 133 (2000).

[69] G. Soyez, Phys. Lett. **B655**, 32 (2007).

[70] H1, C. Adloff *et al.*, Eur. Phys. J. **C30**, 1 (2003).

[71] E. M. Lobodzinska, Acta Phys. Polon. **B35**, 223 (2004).

[72] A. H. Mueller, Nucl. Phys. **B415**, 373 (1994).

[73] A. H. Mueller and B. Patel, Nucl. Phys. **B425**, 471 (1994).

[74] Y. V. Kovchegov, Phys. Rev. **D61**, 074018 (2000).

[75] S. Munier and R. Peschanski, Phys. Rev. Lett. **91**, 232001 (2003).

[76] S. Munier and R. Peschanski, Phys. Rev. **D69**, 034008 (2004).

[77] S. Munier and R. Peschanski, Phys. Rev. **D70**, 077503 (2004).

[78] A. H. Mueller and D. N. Triantafyllopoulos, Nucl. Phys. **B640**, 331 (2002).

[79] H. Kowalski and D. Teaney, Phys. Rev. **D68**, 114005 (2003).

[80] K. J. Golec-Biernat, L. Motyka, and A. M. Stasto, Phys. Rev. **D65**, 074037 (2002).

[81] I. Balitsky, Phys. Rev. **D75**, 014001 (2007).

[82] Y. V. Kovchegov and H. Weigert, Nucl. Phys. **A784**, 188 (2007).

[83] J. L. Albacete and Y. V. Kovchegov, Phys. Rev. **D75**, 125021 (2007).

[84] I. Balitsky and G. A. Chirilli, Phys. Rev. **D77**, 014019 (2008).

[85] R. A. Fisher, Ann. Eugenics. **7**, 355 (1937).

[86] A. Kolmogorov, I. Petrovsky, and N. Piscounov, Moscou Univ. Bull. Math. **A1**, 1 (1937).

[87] U. Ebert and E. van Saarloos, Physica **D146**, 1 (2000).

[88] E. Brunet and B. Derrida, Phys. Rev. **E56**, 2597 (1997).

[89] R. Enberg, Phys. Rev. **D75**, 014012 (2007).

[90] D. N. Triantafyllopoulos, Nucl. Phys. **B648**, 293 (2003).

[91] R. B. Peschanski and S. Sapeta, Phys. Rev. **D74**, 114021 (2006).

[92] A. H. Mueller and A. I. Shoshi, Nucl. Phys. **B692**, 175 (2004).

[93] E. Iancu, A. H. Mueller, and S. Munier, Phys. Lett. **B606**, 342 (2005).

[94] S. Munier, Nucl. Phys. **A755**, 622 (2005).

[95] G. Soyez, Phys. Rev. **D72**, 016007 (2005).

[96] R. Enberg, K. Golec-Biernat, and S. Munier, Phys. Rev. **D72**, 074021 (2005).

[97] Y. Hatta, E. Iancu, C. Marquet, G. Soyez, and D. N. Triantafyllopoulos, Nucl. Phys. **A773**, 95 (2006).

[98] E. Brunet, B. Derrida, A. H. Mueller, and S. Munier, Phys. Rev. **E73**, 056126 (2006).

[99] C. Marquet, G. Soyez, and B.-W. Xiao, Phys. Lett. **B639**, 635 (2006).

[100] A. Dumitru, E. Iancu, L. Portugal, G. Soyez, and D. N. Triantafyllopoulos, JHEP **08**, 062 (2007).

[101] A. Bassetto, M. Ciafaloni, and G. Marchesini, Phys. Rept. **100**, 201 (1983).

[102] Y. L. Dokshitzer and S. I. Troyan, *Proceedings of the XIX Winter School of the LNPI, volume 1* (Leningrad, 1984).

[103] Y. L. Dokshitzer, V. A. Khoze, and S. I. Troian, Adv. Ser. Direct. High Energy Phys. **5**, 241 (1988).

[104] Y. L. Dokshitzer, V. A. Khoze, and S. I. Troian, J. Phys. **G17**, 1481 (1991).

[105] Y. I. Azimov, Y. L. Dokshitzer, V. A. Khoze, and S. I. Troyan, Z. Phys. **C27**, 65 (1985).

[106] Y. I. Azimov, Y. L. Dokshitzer, V. A. Khoze, and S. I. Troyan, Zeit. Phys. **C31**, 213 (1986).

[107] TASSO, W. Braunschweig *et al.*, Z. Phys. **C47**, 187 (1990).

[108] OPAL, M. Z. Akrawy *et al.*, Phys. Lett. **B247**, 617 (1990).

[109] OPAL, G. Abbiendi *et al.*, Eur. Phys. J. **C27**, 467 (2003).

[110] D. G. d'Enterria, AIP Conf. Proc. **806**, 252 (2006).

[111] PHENIX, K. Adcox *et al.*, Nucl. Phys. **A757**, 184 (2005).

[112] B. B. Back *et al.*, Nucl. Phys. **A757**, 28 (2005).

[113] BRAHMS, I. Arsene *et al.*, Nucl. Phys. **A757**, 1 (2005).

[114] STAR, J. Adams *et al.*, Nucl. Phys. **A757**, 102 (2005).

[115] X.-N. Wang, Phys. Lett. **B579**, 299 (2004).

[116] A. Dainese, C. Loizides, and G. Paic, Eur. Phys. J. **C38**, 461 (2005).

[117] K. J. Eskola, H. Honkanen, C. A. Salgado, and U. A. Wiedemann, Nucl. Phys. **A747**, 511 (2005).

[118] M. Gyulassy, I. Vitev, and X. N. Wang, Phys. Rev. Lett. **86**, 2537 (2001).

[119] T. Hirano and Y. Nara, Phys. Rev. **C66**, 041901 (2002).

[120] T. Renk, J. Ruppert, C. Nonaka, and S. A. Bass, Phys. Rev. **C75**, 031902 (2007).

[121] N. Borghini and U. A. Wiedemann, arXiv:hep-ph/0506218 (2005).

[122] S. Sapeta and U. A. Wiedemann, arXiv:0707.3494 [hep-ph] (2007).

[123] M. Gyulassy and X.-n. Wang, Nucl. Phys. **B420**, 583 (1994).

[124] R. Baier, Y. L. Dokshitzer, A. H. Mueller, S. Peigne, and D. Schiff, Nucl. Phys. **B484**, 265 (1997).

[125] B. G. Zakharov, JETP Lett. **65**, 615 (1997).

[126] U. A. Wiedemann, Nucl. Phys. **B588**, 303 (2000).

[127] M. Gyulassy, P. Levai, and I. Vitev, Nucl. Phys. **B594**, 371 (2001).

[128] X.-N. Wang and X.-f. Guo, Nucl. Phys. **A696**, 788 (2001).

[129] CDF, D. E. Acosta *et al.*, Phys. Rev. **D68**, 012003 (2003).

[130] TPC/Two Gamma, H. Aihara *et al.*, Phys. Rev. Lett. **52**, 577 (1984).

[131] PHENIX, S. S. Adler *et al.*, Phys. Rev. Lett. **91**, 072303 (2003).

[132] R. J. Fries, B. Muller, C. Nonaka, and S. A. Bass, Phys. Rev. **C68**, 044902 (2003).

[133] R. J. Fries, B. Muller, C. Nonaka, and S. A. Bass, Phys. Rev. Lett. **90**, 202303 (2003).

[134] L. Maiani, A. D. Polosa, V. Riquer, and C. A. Salgado, Phys. Lett. **B645**, 138 (2007).

[135] D. K. Srivastava, C. Gale, and R. J. Fries, Phys. Rev. **C67**, 034903 (2003).

[136] R. Baier, Y. L. Dokshitzer, A. H. Mueller, and D. Schiff, JHEP **09**, 033 (2001).

[137] B. A. Kniehl, G. Kramer, and B. Potter, Nucl. Phys. **B582**, 514 (2000).

[138] R. J. Fries and B. Muller, Eur. Phys. J. **C34**, s279 (2004).

[139] K. J. Eskola, H. Honkanen, H. Niemi, P. V. Ruuskanen, and S. S. Rasanen, Phys. Rev. **C72**, 044904 (2005).